ABSTRACT

Title of dissertation: RESPONSE CONTROL IN NONLINEAR SYSTEMS WITH NOISE

Vipin K. Agarwal, 2019

Dissertation directed by: Professor Balakumar Balachandran
Department of Mechanical Engineering

Noise is unavoidable and/or present in a wide variety of engineering systems. Although considered to be undesirable from certain viewpoints, it can play a useful role in influencing the behavior of nonlinear mechanical and structural systems that have multiple solutions in the form of equilibrium points, periodic solutions, and aperiodic (including chaotic) solutions. The aim of this dissertation work is to discover clues related to noise enabled steering or control for engendering desirable changes in system behavior.

A combination of experimental, analytical, and numerical studies have been undertaken on the following: i) shifting of jump-up and jump-down frequencies leading to an eventual collapse of hysteresis observed in the response of a nonlinear oscillator, ii) influence of noise on the chaotic response of a nonlinear system, and iii) noise-induced escape route from a chaotic-attractor. Furthermore, a combination of analytical and numerical studies have been undertaken to understand an extended Jeffcott rotor-stator system and the influence of noise on the system dynamics.

Additionally, this dissertation includes work on partial control of chaotic sys-

tems under influence of noise, wherein the trajectories are confined inside a particular region (chaotic attractor) despite the presence of white noise. Maintaining chaotic behavior in systems in the presence of an external disturbance may be desirable and important for the dynamics of certain systems. The proposed algorithm has been shown to be effective for systems with different dimensions.

The dissertation outcomes provide answers to the following fundamental questions: i) how can noise influence the long-time responses of mechanical and structural systems and ii) how can noise be used to steer a system response to avoid an undesirable dynamical state. These answers can serve as an important foundation for many industrial applications (e.g., applications with rotor-stator systems) as well.

RESPONSE CONTROL IN NONLINEAR SYSTEMS WITH NOISE

by

Vipin K. Agarwal

Dissertation submitted to the Faculty of the Graduate School of the
University of Maryland, College Park in partial fulfillment
of the requirements for the degree of
Doctor of Philosophy
2019

Advisory Committee:
Professor Balakumar Balachandran, Chair and Advisor
Professor Amr Baz, Department of Mechanical Engineering
Professor Miao Yu, Department of Mechanical Engineering
Associate Professor Nikhil Chopra, Department of Mechanical Engineering
Distinguished University Professor James A. Yorke, Department of Mathematics, Department of Physics
Professor Isaak D. Mayergoyz, Department of Electrical & Computer Engineering (Dean's Representative)

To my eternal Lord Jagannath, Baladeva and Subhadra Ma.

Acknowledgments

First and foremost, I would like to express my heartfelt gratitude to my advisor and mentor, Professor Balakumar Balachandran for his valuable guidance, patience and support throughout my research. While he gave me a great degree of freedom in my research, his deep insights into the fundamentals of each problem inspired ideas that ultimately took the shape of this dissertation. He set for me high standards of integrity and a mature vision to follow. He always found the time to fit me into his extremely busy schedule. I am incredibly fortunate and appreciative of the opportunity to work under his guidance and learn from such an extraordinary individual.

I would also like to express my deep gratitude to Professor Isaak Mayergoyz for his scientific advice, knowledge and many insightful discussions and suggestions on stochastic dynamics. It has been an absolute honor to have him in my dissertation committee. My earnest thanks to Professor James Yorke for his valuable advice, constructive criticism, and positive appreciation on my research work. Without his extraordinary ideas, elucidations of chaos and mathematical concepts, and inspiring discussions, parts of this dissertation would have been a distant dream. Further, I am highly grateful to Professor Amr Baz, Professor Miao Yu and Professor Nikhil Chopra for agreeing to serve on my dissertation committee and for sparing their invaluable time in reviewing my work. It is a pleasure to learn from each of these individuals through the courses they taught and personal interactions.

I am highly obliged to all of the devotees of Bhakti Yoga Club, in particular

Devaprastha Pr and Padma Malini Mataji who are like my family members, for being so kind to me for all these years. Their loving association has taught me the true meaning of spiritual life. I owe my sincere gratitude to Prof. Behera at IIT Kanpur for his love, care, and constant inspiration. My appreciation goes to all my lab mates for their inputs during our uncountable group meetings and extending me all help whenever I needed it. The atmosphere of learning, cooperation, and fun within the research group has made my journey a truly memorable one. I would like to express my gratitude to my dear friend Raghav, for being infinitely helpful. Further, many thanks to Shikha, Tarun, Dmitry, Natalia, Ratnesh Pr, Ankita Mataji, Ramya, Adil, and Prasad for their friendship and making my time at UMD truly enjoyable.

I would like to thank my parents, and grandparents for their constant unconditional love, support, and sacrifice. My appreciation goes to my bhabhi, sister, Rohit, Neha, Rishi, parents-in-law, Parth, Dhruv, Pradyumna, Mukunda, and Nishan for their love. I owe my deepest thanks to my brother, Vikas who has always stood by me and guided me through my career, and has pulled me through against impossible odds at times. Words cannot express the gratitude I owe him. Finally, and most importantly, I would like to thank my wife, Priti, for bearing with me, giving me a reason to smile every single day and always staying by my side through all the ups and downs. Thank you, Priti, for giving me the best gift of my life, our angel boy Raghav, towards the end of my Ph.D. program. He bought a new joy to my life.

The financial support for this research received through National Science Foundation Grants CMMI-1436141 and CMMI-1760366 are gratefully acknowledged.

Table of Contents

List of Tables

List of Figures

Chapter 1: Introduction

1.1 Problem of Interest

A chief pursuit of this dissertation work is to find and study phenomena that would enable the constructive use of noise and nonlinearity in dynamical systems and determine approaches to use them and extend beyond the traditional stochastic resonance based ones. In this work, in the analysis "noise" refers to white Gaussian noise, which is a random process and generalized derivative of a Wiener process. In the experiments, the considered noise is band-limited white noise.

Additionally, problem of interest to this work is the development of partial control schemes for a nonlinear system under the influence of noise to escape or not enter from regions of undesired dynamical states. As a part of this effort, a combination of analytical, numerical, and experimental studies have been undertaken to understand the responses of nonlinear systems of different dimensions.

Noise can have a dramatic effect on the response of a nonlinear system by making the determination of bifurcation points difficult or by shifting the bifurcation points, tied to which are qualitative changes in the system response with respect to variations in one or more parameter values. The focus of this dissertation work is on the influence of noise on dynamics of several nonlinear systems (e.g., Duffing

oscillator, Jeffcott rotor) and on the application of the partial control scheme to a nonlinear system to avoid certain undesired behaviors without determining a specific trajectory. The motivation of this work is to understand and exploit noise to improve the performance of a mechanical system by changing long-term system behavior and to develop a scheme for controlling the trajectory of a mechanical system inside a particular desired region under the influence of noise.

1.2 Literature Review

1.2.1 Literature Review on Noise-Influenced Response of Duffing Oscillators

Noise occurs naturally in many systems. In general, noise is considered as being undesirable for the performance of an engineering system. However, noise can play a significant role in influencing system dynamics. In particular, the effects of noise on the behavior of a nonlinear system exhibiting chaotic motions has received considerable attention in recent years. Frey and Simiu (1993) explored the use of Melnikov analysis to study the effect of additive noise. The effect of bounded noise on the response of a Duffing oscillator subjected to parametric excitation has also been examined (Liu *et al.*, 2001). Gan (2006) studied noise-induced fractal boundaries in a Duffing system. Yang *et al.* (2005) observed the effects of bounded noise on chaotic motion of a triple-well potential system. The effects of bounded noise on a class of double-well systems has also been examined by Liu *et al.* (2013). In the last few years, effects of noise on the response of Duffing oscillator and coupled, nonlinear

oscillators have received considerable attention (Perkins and Balachandran, 2012; Perkins *et al.*, 2016; Ramakrishnan and Balachandran, 2010a,b, 2011).

The Duffing equation, which was introduced in 1918 (Duffing, 1918), has been subject of experimental and numerical investigations over a wide range of system parameter values. A Duffing oscillator system has a linear stiffness term and a nonlinear (cubic) stiffness term. In numerous nonlinear vibration text books (Nayfeh and Mook, 2008; Hayashi, 2014; Kovacic and Brennan, 2011), various methods have been deliberated to determine and understand the response of a forced nonlinear oscillator with linear and nonlinear cubic stiffness terms. This oscillator system can exhibit either a hardening or a softening characteristic, depending on the nature of the physical system being studied. This system characteristic determines the equilibrium states of the system. The response of Duffing oscillator with a hardening spring has been the subject of experimental and numerical investigations (Mallik, 2008; Perkins, 2017).

Through extensive analytical, experimental, and numerical studies, it has been discovered that the system response curves have a hysteresis characteristic when the system is subjected to a quasi-static variation in the forcing frequency near the system resonance (Nayfeh and Mook, 2008; Gottwald *et al.*, 1992; Nayfeh and Balachandran, 1995; Westra *et al.*, 2010; Kalmár-Nagy *et al.*, 2011). In the hysteresis region, for a particular value of the forcing frequency, the forced Duffing oscillator response is multi-valued. Dual memory storage and logic devices are few examples of practical use of two stable states of a forced Duffing oscillator (Yao and Hikihara, 2013, 2012). A number of systems exhibit hysteresis behavior. For

example, it is mentioned that magnetic hysteresis is a notable characteristic of ferromagnetic materials, and this behavior is associated with the irreversibility of the magnetisation and demagnetisation when the magnetic field is relaxed. Different mathematical models of magnetic hysteresis have been developed by a number of researchers (Mayergoyz, 1991; Wen, 1976; Dimian and Andrei, 2014a). In several studies (Dimian and Andrei, 2014b; Brown *et al.*, 2016), the fundamental deterministic and stochastic aspects of hysteresis loops have been discussed in detail. Serpico *et al.* (2015) studied superparamagnetic-like transitions in connection with the bifurcations of the effective potential with respect to variation in the temperature and excitation conditions. Through analytical and numerical studies, noise driven relaxation phenomena in scalar and vector hysteretic systems have been examined in the time domain (Dimian and Andrei, 2014b). Analysis of output spectral density for hysteretic systems driven by noisy inputs has also been conducted Dimian and Andrei (2014).

The dynamics of a nonlinear system depends on the parameters chosen in the governing equation of motion. With a variation in the chosen control parameter, the qualitative behavior of nonlinear system can be considerably changed. For certain parameter ranges, a nonlinear system can exhibit chaotic behavior. There is a large body of literature on chaotic attractors of a nonlinear system and their basins of attraction. Bifurcation theory can be used to describe the way in which different attractors are created or destroyed with the change in system parameters. There are several routes to chaos and a positive Lyapunov exponent is indicative of chaos. The behavior of a Duffing oscillator system can be chaotic for certain system pa-

rameter values and external forcing parameters, as have been shown through several experimental and numerical studies (Gottwald *et al.*, 1992; Moon, 1980; Todd and Virgin, 1997). After chaos is germinated, a further variation in system parameters can lead to interesting results that can have potential applications in controlling system dynamics. As a control parameter is varied, a sudden discontinuous change in the chaotic attractor of a dissipative dynamical system is called "crisis," a term introduced in the work of Grebogi *et al.* (1982). A crisis occurs when a chaotic attractor comes into contact with an unstable periodic orbit (see for example, Nayfeh and Balachandran (1995); Alligood *et al.* (1996) for a detailed discussion). A crisis can be identified as a boundary/exterior crisis, or interior crisis, or attractor merging crisis (Nayfeh and Balachandran, 1995; Grebogi *et al.*, 1982, 1986; Sommerer *et al.*, 1991). A 1-D quadratic map can exhibit all three types of crises (Nayfeh and Balachandran, 1995). The forced Duffing oscillator is one of the non-autonomous systems, which can exhibit crisis Hong and Xu (1999). In the last decade, special attention has been paid to the effect of noise on nonlinear systems exhibiting chaotic behavior. Xu *et al.* (2005) have investigated stochastic bifurcation and crisis through the global generalized cell mapping in a twin-well Duffing system subject to a harmonic excitation in presence of noise.

1.2.2 Literature Review on Partial Control of a Chaotic System in the Presence of Noise

Generally speaking, one considers noise as being undesirable for the performance of an engineering system. Chaotic motions of a system may also not be preferrable and various means have been used to control these motions. The proceedings of an IUTAM meeting organized by Professors Rega and Vestroni serves as a rich example (Rega and Vestroni, 2006). Aperiodic behavior can play a significant role in influencing system dynamics, as observed in the context of several systems; for example, avoidance of undesired resonances in mechanical systems and enhancement of the efficiency of a thermal pulse combustor are some applications where chaos can be beneficial (Georgiou and Schwartz, 1996; In *et al.*, 1997). There are also other non-mechanical systems such as biological systems, in which chaotic behavior can play an important role. In living organisms, chaotic dynamics has been stated to be important for some vital functions (Perc and Marhl, 2006). It has been noted that preserving chaos is of potential relevance to biological disorders (Yang *et al.*, 1995).

There are certain situations in which a system's trajectory has characteristics of chaotic behavior for a finite duration of time, before the trajectory escapes to another state that could correspond to a periodic attractor or another state. Sometimes, this end state could be undesirable. This type of behavior is often described as transient chaos. An important example of this kind of behavior is undesired tumor growth (López *et al.*, 2014).

Maintaining chaotic behavior in systems in the presence of an external disturbance can be desirable and important for the dynamics of the considered system. This has motivated studies and efforts on different control techniques, such as, the partial control method studied by Zambrano *et al.* (2008); Sabuco *et al.* (2012a,b). These methods have been designed for application to deterministic systems with bounded noise Zambrano and Sanjuán (2009). The presence of even a low level of noise can radically change the dynamics of a chaotic system, as these perturbations can experience exponential growth.

In the method proposed by Sabuco *et al.* (2012a), the property of transient chaos is used. The goal is to keep the trajectory inside a particular region without moving towards any attractor. The method has been shown to be effective, and one can use this method to control the trajectory by using an upper bound on the control u_0 that is less than the upper bound on the disturbance ξ_0. This control method has been applied to several dynamical systems, including the Hénon map, Duffing oscillator, and other systems in the context of ecology and cancer (López *et al.*, 2014; Capeáns *et al.*, 2014). In all of the previous use of partial control methods, a bounded representation of noise has been used.

1.2.3 Literature Review on Noise-Influenced Rotor Dynamics

The classical Jeffcott rotor system, a simplified, lumped-parameter model of rotors used in practice, was introduced by Jecffott (1919). This system has been subject of numerous studies in the literature. Despite being simple compared to

other rotor models, one can capture the basic characteristics of rotor dynamics by using the Jeffcott model.

Many efforts on studying the dynamics of rotor confined inside a fixed stator have been reported. For example, Black (1966, 1968) examined the forward whirling and backward whirling solutions of a Jeffcott rotor contained within a stator subjected to dry-friction. The torsional vibrations and stability of a two degree-of-freedom rotor model with nonlinear conditions have been explored by Jansen (1991). This study has served as the basis for several other efforts with the intent of modeling drill strings. A large number of research publications have focused on numerical and experimental studies of the nonlinear response of torsional vibrations of a rotor-stator system (Liao *et al.*, 2011, 2012; Vlajic *et al.*, 2014a). Analytical and numerical investigation of the torsional vibrations of a rotor with continuous stator contact during forward and backward whirling has been explored by Vlajic *et al.* (2014b). Diangui (2000) studied the characteristics of torsional vibration of a rotor with rotor-stator contact and confirmed that the measured natural torsional frequency with contact is higher than the one without contact.

In addition, there is a large body of literature on controlling torsional vibrations and stick-slip motions which can cause the rotor to store and release torsional energy. Jansen and Van Den Steen (1995) described an active damping system and used feedback control for vibration-free rotation. Robust μ synthesis controllers and H∞ controller have been used for suppressing stick-slip induced vibrations in oil well drill strings (Karkoub *et al.*, 2010; Serrarens *et al.*, 1998). Christoforou and Yigit (2003) presented an active control strategy, which was based on optimal state feed-

back control designed to control drill-string rotational motions. Al-Hiddabi *et al.* (2003) constructed a nonlinear dynamic inversion control scheme to suppress the lateral and the torsional vibrations of a drill string. Recently, Kreuzer and Steidl (2012) suggested a method for controlling the torsional vibrations of drill strings by decomposing the drill-string dynamics into two traveling waves traveling in the direction of the top drive and in the direction of the drill bit at the bottom. Alzibdeh *et al.* (2016) considered effects of sinusoidal drive speed modulation on the rotor with continuous stator contact.

As detailed in Chapter 4, the author has considered white Gaussian noise modulation in the rotor driving speed, for implementing an open-loop non-collocated control scheme, to mitigate the continuous rotor-stator contact. The current study on the use of noise for response control of the system dynamics has been undertaken to find alternative control schemes, in light of the difficulties and challenges in installing and operating the sensors and actuators needed for closed-loop and/or collocated control schemes.

1.3 Objectives

The overall goal of this work is to understand how low-intensity noise in combination with an appropriate deterministic input can be used to push the system into the basin of attraction of a desired system response or move the system away from region of undesired response, and how the long-time responses of mechanical and structural systems can be influenced by exercising partial control with noise

and steering the responses to sculpt regions of the state space called safe sets.

To realize the previously mentioned goal, the following objectives were pursued as a part of this dissertation work.

1. Conduct a combined analytical, numerical and experimental study of a Duffing oscillator system to examine the changes in dynamics under the influence of noise in different settings, in particular, the chaotic dynamics of a soft Duffing oscillator

2. Construct a partial control scheme for a Duffing oscillator in presence of white noise to keep the trajectories inside a particular region of state-space

3. Study the deterministic and stochastic dynamics of torsional vibrations and whirling motions for a Jeffcott rotor contained within a stator during forward and backward whirling motions along with continuous rotor-stator contact.

One of the highlights of this work is the gathering of a first numerical-experimental evidence for a noise-induced escape route from a chaotic attractor to a periodic attractor. While in the current work, the author deals with specific systems with specific parameters, it is believed that the observed phenomena are quite general and extensions to a wide range of nonlinear systems are expected to be possible.

1.4 Organization of Dissertation

The rest of the dissertation is organized as follows. Several conference and journal articles have followed during the course of this dissertation work. These

articles are cited in this section as well as in the different chapters. In Chapter 2, the effects of noise on a Duffing oscillator system are discussed (Agarwal and Balachandran, 2015; Agarwal *et al.*, 2018, 2019). Experimental efforts and results along with analytical-numerical results are presented and discussed. The influence of white Gaussian noise on the frequency responses of monostable and bistable, softening Duffing oscillators are studied. In Chapter 3, the author describes the concept of a safe set, the Sculpting Algorithm for computing a safe set, and the partial control method for a system with white noise by using the Euler-Maruyama integration method (Agarwal *et al.*, 2017; Agarwal and Balachandran, 2019a). Subsequently, an application of this method to the response of a Duffing oscillator is considered. In particular, parameters for which this system experiences a transient chaotic behavior are considered and comparisons are made between the cases with white noise and bounded noise. In Chapter 4, the torsion and whirling responses of a modified Jeffcott rotor confined within a fixed stator are studied. Additionally, the influence of noise on whirling responses are outlined (Agarwal and Balachandran, 2019b). In Chapter 5, the dissertation contributions are highlighted and future directions are discussed.

Chapter 2: Noise-Influenced Responses of Duffing Oscillators

In this chapter, a treatment of the influence of white Gaussian noise on the dynamics of a Duffing oscillator is presented based on the work of Agarwal and Balachandran (2015); Agarwal *et al.* (2018, 2019). Here, the author reports on the following: i) how an introduction of noise in a Duffing oscillator with softening characteristic can influence the chosen system's aperiodic behavior. ii) how an introduction of noise in a Duffing oscillator can influence the frequency-response curve and destroy it. Finally, the author subjects chaotic trajectories to white Gaussian noise at low levels that are just sufficient to cause a trajectory to escape from the basin. According to experimental and computational results, there is a specific escape route that the trajectory always follows. Here, the boundary of the basin of the chaotic attractor is the stable manifold of a periodic orbit. This manifold is captured through a stroboscopic plotting of data. As the trajectory escapes, it is observed that it is essentially on the basin boundary. The dynamics pulls the trajectory to the fixed point on the boundary and the trajectory escapes along the unstable manifold. This work provides a glimpse into the possibilities for noise-influenced responses.

The rest of this chapter is organized as follows. In Section 2.1, the author describes the experimental arrangement. In Section 2.2, the modeling efforts un-

Table 2.1: Nomenclature describing the quantities governing the Duffing oscillator.

Nomenclature	
x	Nondimensional oscillator displacement
x_1	Nondimensional oscillator position in state space
x_2	Nondimensional oscillator velocity in state space
ω_n	Linear natural frequency
c	Viscous damping
k_1	Linear stiffness
k_3	Nonlinear stiffness
η	Nondimensional damping factor
α	Nondimensional linear stiffness
β	Nondimensional nonlinear stiffness
$\hat{F}_0$	Nondimensional forcing amplitude
Ω	Nondimensional forcing frequency
$\dot{W}(t)$	White Gaussian noise
σ_N	Amplitude of noise for numerical simulations
σ_E	Amplitude of noise for experimental studies

dertaken for the nonlinear oscillator along with a nondimensionalization scheme for parameter identification, and Euler-Maruyama simulations are presented. In Section 2.3, the numerical and experimental results for noise influenced chaotic Duffing oscillator are presented. A comprehensive treatment of the influence of white Gaussian noise on the frequency-responses of both monostable and bistable Duffing oscillators with softening characteristics is presented and discussed in Section 2.4. In Section 2.5, noise-induced chaotic-attractor escape route is described. According to the experimental and computational results, it is reported that there is specific escape route that the trajectory always follow. Finally, conclusions are drawn together and presented in Section 2.6. In addition, striking similarities and differences between results obtained through experimental and numerical investigations are discussed in Section 2.6.

2.1 Experimental Arrangement

The experimental prototype of the Duffing oscillator and schematic of the experimental setup are shown in Figure 2.1. The experimental arrangement consists of a cantilever steel structure with an attached tip mass magnet at its free end. The tip mass magnet is located in the magnetic field of another magnet that is fixed in a position close to it. The inter-magnet separation can be varied and the magnet orientations can be reversed to realize a nonlinear Duffing oscillator with either a hardening or a softening (monostable or bistable) characteristic. The other end of the cantilever structure is excited by an electromagnetic shaker that is used to provide the deterministic input (harmonic excitation) and the additive Gaussian noise input. The excitation provided by the shaker is along a direction normal to the longitudinal axis of the beam oscillator allowing for excitation of bending motions of the structure. Given the cantilever structure's orientation, for the purpose of the current experimental arrangement, the influence of gravity is neglected in modeling the cantilever structure dynamics. Although the author does not take an explicit model for the magnets into account but all the effects of the system identifications are captured.

Several means are employed to gather experimental data. The free-end displacement of the cantilever structure is measured by using a strain gauge, which is secured on the cantilever structure, and the NI cDAQ-9178 with an NI 9235 module. The harmonic excitation amplitude is measured by using a 3-axis accelerometer (SparkFun ADXL337) that is attached to the shaker head at the base of the can-

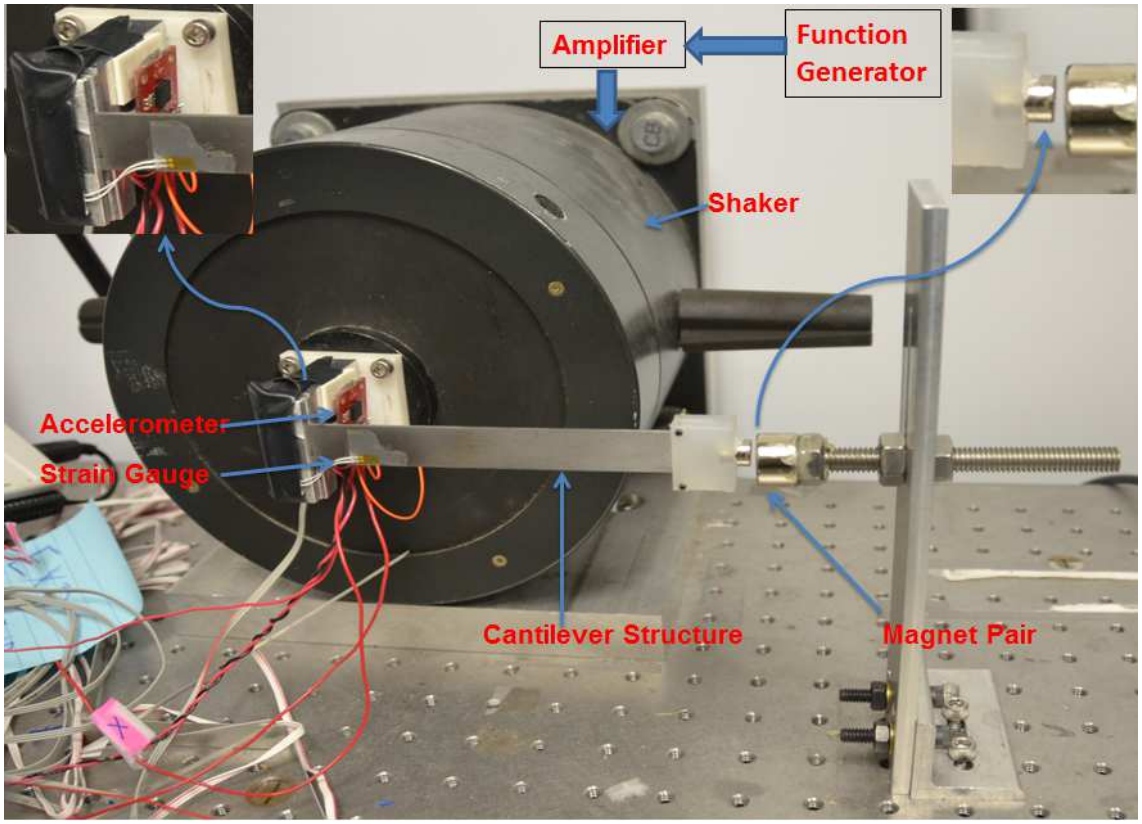

(a)

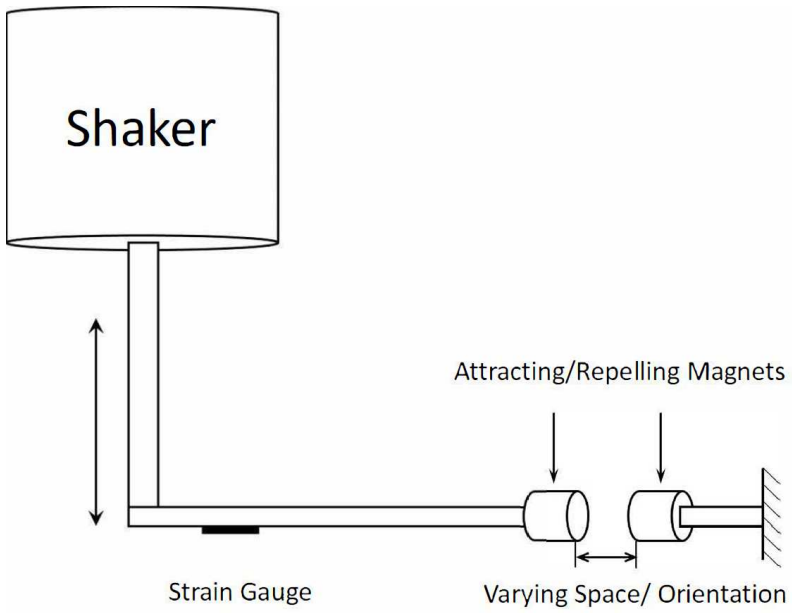

(b)

Figure 2.1: (a) Experimental arrangement. (b) Schematic of Duffing oscillator. The separation between the magnets and their relative orientations are varied. An electromagnetic shaker is used to provide the deterministic harmonic excitation along with a white Gaussian noise input.

tilever structure. A LabVIEW® program was developed to provide the deterministic harmonic excitation and Gaussian noise input to the Brüel & Kjær electromagnetic shaker through NI modules. In addition, the same LabVIEW® program is used for real time data acquisition of the strain gauge and the accelerometer signals. The natural frequencies of the system depend on the inter-magnet separation and relative orientations of the magnets.

Both hardening and softening characteristic of the nonlinear systems were realized in the experiments, as noted earlier. The experimental setup was noted to be quite sensitive to the relative spacing of the magnets. When both the magnets repel each other, the system behaves as a bistable, softening nonlinear oscillator with two stable potential wells, as the zero tip deflection position is unstable. On the other hand, when the magnets attract each other, the system behaves as a monostable, nonlinear oscillator with hardening or softening characteristic and the zero tip deflection position is stable. For all of the experimental studies, the author focused both on monostable and bistable Duffing oscillators with softening characteristics.

2.2 Mathematical Modeling, Nondimensionalization, and Parameter Identification

The equation of motion of a Duffing oscillator with a mass m, a viscous damping c, a linear stiffness k_1, a nonlinear stiffness k_3, a forcing amplitude F_0, and a forcing frequency ω can be written as

Table 2.2: Stiffness parameters and different Duffing oscillator realizations

Linear stiffness	Cubic stiffness	Oscillator characteristic
$k_1 > 0$	$k_3 > 0$	monostable, hardening
$k_1 > 0$	$k_3 < 0$	monostable, softening
$k_1 < 0$	$k_3 > 0$	bistable, softening

$$m\ddot{y} + c\dot{y} + k_1 y + k_3 y^3 = F_0 \cos(\omega t). \tag{2.1}$$

where m, c and F_0 are all positive-valued quantities. Different values of stiffness parameters k_1 and k_3 correspond to different Duffing oscillator characteristics, as presented in Table 2.2. Without the damping and external force, the system also represents a Hamiltonian system.

In the current work, the author has considered monostable and bistable, Duffing oscillators with softening characteristics. The harmonic excitation or deterministic input is represented by $F_0 \cos(\omega t)$. The Duffing oscillator represented by equation (2.1) exhibits a hysteresis behavior when the excitation frequency ω is used as a control parameter in a frequency range around the system resonance. As an example of this behavior, the frequency-response curves obtained for a Duffing oscillator with softening characteristic is displayed in Figure 2.14.

2.2.1 Monostable, Softening Duffing Oscillator

For a monostable, Duffing oscillator with softening characteristics, $k_1 > 0$ and $k_3 < 0$, the system oscillates about the equilibrium point at $(0, 0)$. The linear

natural frequency of the system is given by $\omega_n = \sqrt{\frac{k_1}{m}}$. Considering equation (2.1) and dividing both sides by the mass m, and introducing the nondimensional variables $\tau = \omega_n t$, $\Omega = \omega/\omega_n$; after some manipulations, equation (2.1) can be rewritten as

$$y'' + \eta y' + \alpha y + \hat{k}_3 y^3 = \tilde{F}_0 \cos(\Omega\tau). \tag{2.2}$$

where the prime symbol "$\prime$" represents the nondimensional time derivative $\frac{d}{d\tau}$, $\eta = \frac{c}{m\omega_n}$, $\alpha = \frac{k_1}{m\omega_n^2}$, $\hat{k}_3 = \frac{k_3}{m\omega_n^2}$, and $\tilde{F}_0 = \frac{F_0}{m\omega_n^2}$.

For weak forcing, weak damping, weak nonlinearity, and an excitation frequency close to the system natural frequency, the frequency-response equation for this system with cubic nonlinearity can be written as Nayfeh and Mook (2008)

$$\frac{\eta^2}{4} + \left(\Omega - 1 - \frac{3}{8}\frac{\hat{k}_3 a^2}{\Omega_n}\right)^2 = \frac{\tilde{F}_0^2}{4\Omega_n^2 a^2} \tag{2.3}$$

where $\Omega = \omega/\omega_n$, $\Omega_n = \omega_n/\omega_n = 1$, and "$a$" represents the amplitude of oscillation at the forcing frequency Ω. The details on the construction of this equation are provided in Appendix A. From equation (2.3), one can define the largest amplitude of the frequency-response curve as a_p, which takes the form $a_p = \frac{\tilde{F}_0}{\eta\Omega_n}$.

Furthermore, the displacement "y" in equation (2.2) is normalized with the maximum amplitude a_p by defining a nondimensional displacement $x = y/a_p$ and the nondimensional amplitude $A = a/a_p$. With this substitution, equation (2.2) can be modified as

$$x'' + \eta x' + \alpha x + \beta x^3 = \hat{F}_0 \cos(\Omega\tau). \tag{2.4}$$

where $\alpha = \Omega_n^2 = 1$, $\beta = \hat{k}_3 a_p^2$ and $\hat{F}_0 = \frac{\tilde{F}_0}{a_p}$. Then, the frequency-response equation given by equation (2.3) can be written as

$$\frac{\eta^2}{4} + \left(\Omega - 1 - \frac{3}{8}\frac{\beta A^2}{\Omega_n}\right)^2 = \frac{\hat{F}_0^2}{4\Omega_n^2 A^2} \tag{2.5}$$

where the maximum nondimensional amplitude of the frequency-response curve is $A_p = 1$. In equations (2.4) and (2.5), all of the parameters η, α, β, and $\hat{F}_0$, Ω, and x are nondimensional.

The displacement data measured in the experiments are normalized with respect to the largest amplitude measured during the deterministic frequency sweep experiment. Then, the analytical frequency-response results obtained through equation (2.5) are curve fitted to the normalized, deterministic frequency-response data from the experiments. The resulting parameter values are used to conduct numerical simulations under the influence of noise as discussed in later sections.

2.2.2 Bistable, Softening Duffing Oscillator

For a bistable, Duffing oscillator with softening characteristic, $k_1 < 0$ and $k_3 > 0$, considering equation (2.1) and dividing both sides by the mass m results in

$$\ddot{y} + \breve{c}\dot{y} - \breve{k}_1 y + \breve{k}_3 y^3 = \breve{F}_0 \cos(\omega t). \tag{2.6}$$

where $\breve{c} = c/m$, $\breve{k}_1 = -k_1/m > 0$, $\breve{k}_3 = k_3/m > 0$ and $\breve{F}_0 = F_0/m$. The above system have two equilibrium points in state-space at $(+\sqrt{\breve{k}_1/\breve{k}_3}, 0)$ and $(-\sqrt{\breve{k}_1/\breve{k}_3}, 0)$. The system can oscillate about these stable equilibrium points. Considering the system

oscillations about the static equilibrium point at $(+\sqrt{\breve{k}_1/\breve{k}_3}, 0)$ and substituting $y = \sqrt{\frac{\breve{k}_1}{\breve{k}_3}} + \breve{y}$ in equation (2.6), the author obtains

$$\ddot{\breve{y}} + \breve{c}\dot{\breve{y}} + 2\breve{k}_1\breve{y} + 3\sqrt{\breve{k}_1\breve{k}_3}\breve{y}^2 + \breve{k}_3\breve{y}^3 = \breve{F}_0\cos(\omega t). \tag{2.7}$$

The linear natural frequency of this system is given by $\omega_n = \sqrt{2\breve{k}_1} = \sqrt{\frac{-2k_1}{m}}$. Introducing the nondimensional variables $\tau = \omega_n t$, $\Omega = \omega/\omega_n$, after some manipulations, equation (2.1), is rewritten as

$$\breve{y}'' + \tilde{c}\breve{y}' + \tilde{k}_1\breve{y} + \tilde{k}_2\breve{y}^2 + \tilde{k}_3\breve{y}^3 = \tilde{F}_0\cos(\Omega\tau). \tag{2.8}$$

where "$\prime$" represents nondimensional time derivative $\frac{d}{d\tau}$, $\tilde{c} = \frac{\breve{c}}{\omega_n}$, $\tilde{k}_1 = \frac{2\breve{k}_1}{\omega_n^2}$, $\tilde{k}_2 = \frac{3\sqrt{\breve{k}_1\breve{k}_3}}{\omega_n^2}$, $\tilde{k}_3 = \frac{\breve{k}_3}{\omega_n^2}$, and $\tilde{F}_0 = \frac{\breve{F}_0}{\omega_n^2}$.

For weak damping, weak nonlinearity, and weak forcing close to the system resonance, the frequency-response of the system represented given by equation (2.8) can be written as Nayfeh and Mook (2008)

$$\frac{\tilde{c}^2}{4} + \left(\Omega - 1 - \frac{9\tilde{k}_3\Omega_n^2 - 10\tilde{k}_2^2}{24\Omega_n^3}a^2\right)^2 = \frac{\tilde{F}_0^2}{4\Omega_n^2 a^2} \tag{2.9}$$

where $\Omega = \omega/\omega_n$, $\Omega_n = \omega_n/\omega_n = 1$, and "$a$" represents the amplitude of oscillation at forcing frequency Ω. The details on the construction of this equation are provided in Appendix A.

Similar to the monostable case, the largest amplitude of the frequency-response curve is defined as $a_p = \frac{\tilde{F}_0}{\tilde{c}\Omega_n}$. Furthermore, the displacement $\breve{y}$ in equation (2.8) is

normalized with maximum amplitude a_p by defining a nondimensional displacement $\hat{y} = \breve{y}/a_p$ and the nondimensional amplitude $A = a/a_p$. With this substitution, equation (2.8) can be rewritten as

$$\hat{y}'' + \hat{c}\hat{y}' + \hat{k}_1\hat{y} + \hat{k}_2\hat{y}^2 + \hat{k}_3\hat{y}^3 = \hat{F}_0\cos(\Omega\tau). \tag{2.10}$$

where $\hat{c} = \tilde{c}$, $\hat{k}_1 = \tilde{k}_1$, $\hat{k}_2 = \tilde{k}_2 a_p$, $\hat{k}_3 = \tilde{k}_3 a_p^2$, and $\hat{F}_0 = \frac{\tilde{F}_0}{a_p}$.

For weak damping, weak nonlinearity and weak forcing close to the system resonance, the nondimensional frequency-response given by equation (2.9) can be obtained as

$$\frac{\hat{c}^2}{4} + \left(\Omega - 1 - \frac{9\hat{k}_3\Omega_n^2 - 10\hat{k}_2^2}{24\Omega_n^3}A^2\right)^2 = \frac{\hat{F}_0^2}{4\Omega_n^2 A^2} \tag{2.11}$$

where $A = a/a_p$ represents the nondimensional amplitude of frequency-response curve at a particular forcing frequency Ω. The maximum nondimensional amplitude of the frequency-response curve is $A_p = 1$. By substituting the value of $\hat{k}_2$, the above expression can be further simplified to

$$\frac{\hat{c}^2}{4} + \left(\Omega - 1 - \frac{3}{8}\frac{(-4\hat{k}_3)}{\Omega_n}A^2\right)^2 = \frac{\hat{F}_0^2}{4\Omega_n^2 A^2} \tag{2.12}$$

Alternatively, after substituting $x = y/a_p$, $\tau = \omega_n t$ with $\omega_n = \sqrt{\frac{-2k_1}{m}}$, and $\Omega = \frac{\omega}{\omega_n}$, equation (2.1) can be rewritten as

$$x'' + \eta x' + \alpha x + \beta x^3 = \hat{F}_0\cos(\Omega\tau). \tag{2.13}$$

where the prime symbol "′" represents the nondimensional time derivative $\frac{d}{d\tau}$, $\Omega_n = 1$, $\eta = \frac{c}{m\omega_n}$ $\alpha = \frac{k_1}{m\omega_n^2} = -0.5$, $\beta = \frac{k_3 a_p^2}{m\omega_n^2}$, and $\hat{F}_0 = \frac{F_0}{m\omega_n^2 a_p}$.

Also, the nondimensional frequency-response given by (2.12) can be rewritten as

$$\frac{\eta^2}{4} + \left(\Omega - 1 - \frac{3}{8}\frac{(-4\beta)A^2}{\Omega_n}\right)^2 = \frac{\hat{F}_0^2}{4\Omega_n^2 A^2} \tag{2.14}$$

In equations (2.13) and (2.14), all of the given parameters η, α, β. and $\hat{F}_0$, Ω, and x are nondimensional.

Similar to the monostable, Duffing oscillator case with softening characteristic, the experimentally obtained displacement data are normalized with respect to the largest amplitude measured in the deterministic frequency sweep experiment.

The analytical frequency-response results obtained through equation (2.14) are curve fitted to the normalized, deterministic frequency-response data obtained from the experiments. The resulting parameter values are used for numerical simulations under the influence of noise that is discussed in later sections.

With the addition of white Gaussian noise, the Duffing oscillator equation given by either equation (2.4) or (2.13) can be written as

$$x'' + \eta x' + \alpha x + \beta x^3 = \hat{F}_0 \cos(\Omega\tau) + \sigma_N \dot{W}(\tau). \tag{2.15}$$

where the harmonic excitation or deterministic input is represented by $\hat{F}_0 \cos(\Omega\tau)$ and the noise input to the system is represented by $\sigma_N \dot{W}(\tau)$, where σ_N represents the noise amplitude used in the numerical simulation, $W(t)$ represents the Wiener

process, and $\dot{W}(\tau)$ is a "mnemonic" derivative. The above equation can be rewritten into the state-space form as

$$\begin{cases} x_1' &= x_2 \\ x_2' &= -\eta x_2 - \alpha x_1 - \beta x_1^3 + \hat{F}_0 \cos(\Omega\tau) + \sigma_N \dot{W}(\tau) \end{cases} \tag{2.16}$$

To carry out numerical studies, the above equations are expressed in the Langevin form as

$$\begin{cases} dx_1 &= x_2 d\tau \\ dx_2 &= \Big(-\eta x_2 - \alpha x_1 - \beta x_1^3 + \hat{F}_0 \cos(\Omega\tau) \Big) d\tau + \sigma_N dW \end{cases} \tag{2.17}$$

It is mentioned that in this differential form, one no longer has the derivative of the Brownian motion (which does not exist) but a differential white noise which does exist. Now, the Euler-Maruyama method can be used to obtain numerical solutions of equation (2.17). The quantity dW, is the incremental noise, which has a mean that is equal to zero and a standard deviation that is equal to $\sqrt{d\tau}$.

2.3 Influence of Noise on Aperiodic Response of a Duffing Oscillator

In this section, the author primarily focuses on investigating the influence of Gaussian white noise on the aperiodic behavior of softening Duffing system. In the presence of harmonic excitations, the complex motions of this system are examined through experimental and numerical means. The influence of noise on the system response is studied, and it is shown that with an appropriate level of noise, the aperiodic behavior of a harmonically forced oscillator can be significantly influenced.

2.3.1 Experimental Results

The author focused on the softening case for inputs with noise inclusion in the experimental arrangement. The experimental system was observed to display aperiodic behavior for a narrow range of parameters, during primary and secondary resonance excitations. As a representative example, the system response around the excitation frequency of 21.05 Hz and forcing level of 88 N has been studied. The first natural frequency of the cantilever structure is around 50 Hz, and as the deterministic excitation frequency was reduced in a quasi-static sweep, a jump location was identified on the upper branch of the frequency-response curve. The excitation frequency of 21.05 Hz is close to this jump location.

The experimental results obtained for the system responses are presented in Figure 2.2 to Figure 2.6. In all cases, to construct the phase portrait projections, a measure of the cantilever tip displacement is plotted versus the associated velocity. This information is also used in the construction of the associated Poincaré sec-

tions. The aperiodic behavior of the considered soft Duffing oscillator is shown in Figure 2.2. The corresponding Poincaré section constructed by using the deterministic excitation frequency as a clock frequency suggests a fractal geometry, which is characteristic of a chaotic motions. A positive Lyapunov exponent value of 0.11 determined from the response data confirms the chaotic nature of the motion.

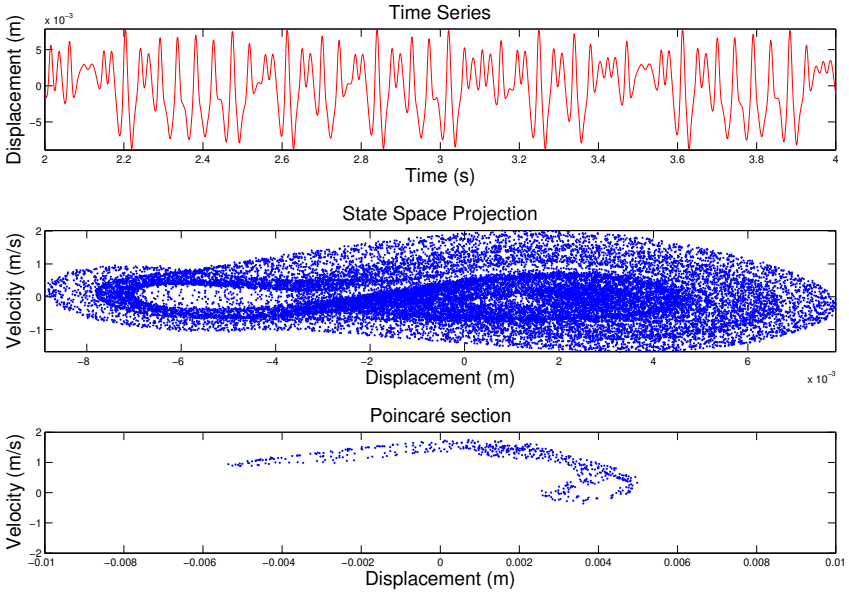

Figure 2.2: Experimental results: Softening Duffing oscillator response in the case without noise and deterministic harmonic excitation, chaotic behavior at excitation frequency f = 21.05 Hz.

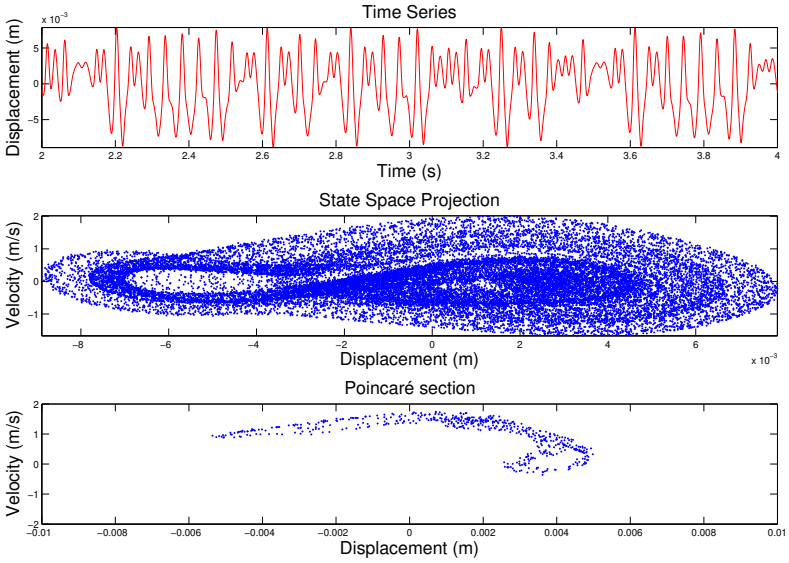

(a)

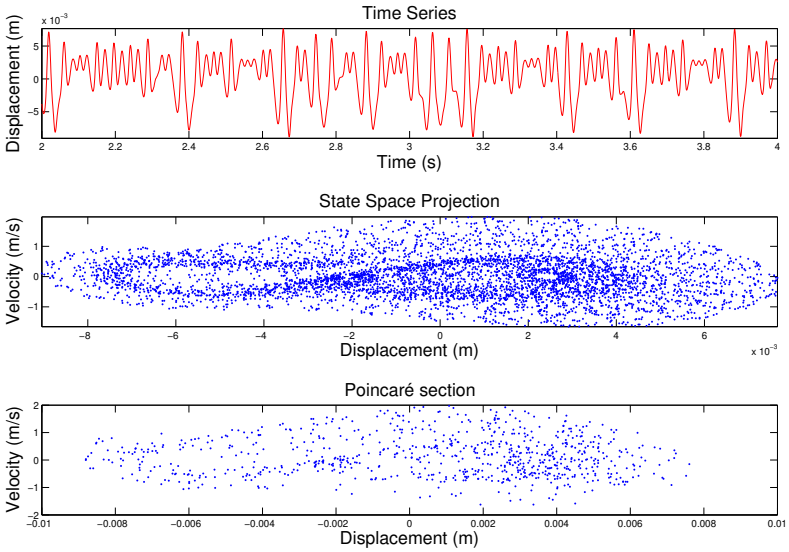

(b)

Figure 2.3: Experimental results: Softening Duffing oscillator response with (a) noise amplitude = 0.1 and (b) noise amplitude = 0.5. The excitation frequency f = 21.05 Hz for the deterministic input, whose level is the same in the cases with noise and without noise.

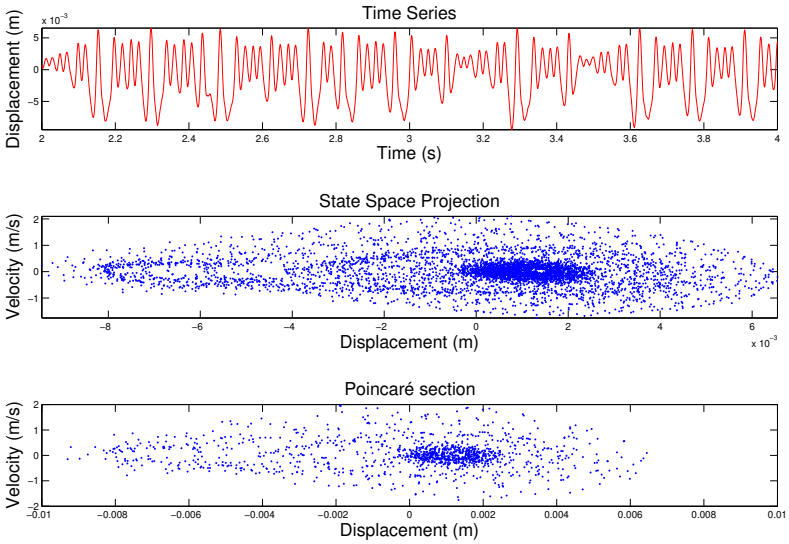

(a)

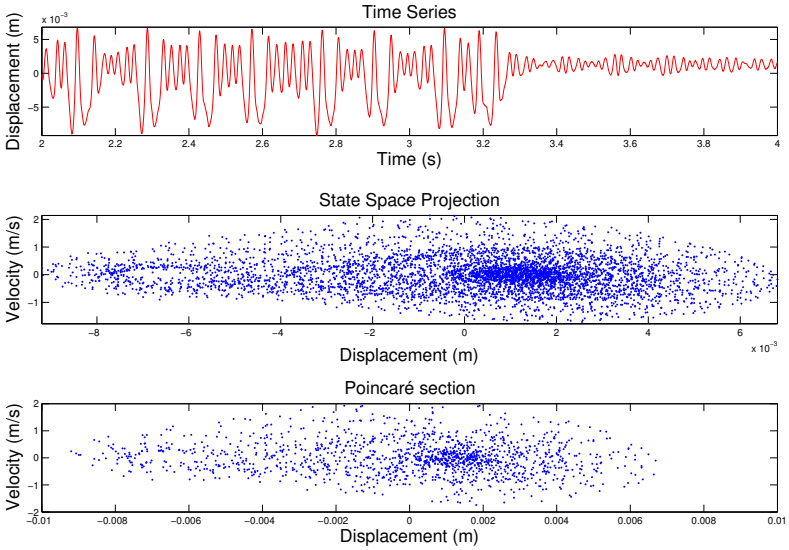

(b)

Figure 2.4: Experimental results: Softening Duffing oscillator response with (a) noise amplitude = 1 and (b) noise amplitude = 1.5. The excitation frequency f = 21.05 Hz for the deterministic input, whose level is the same in the cases with noise and without noise.

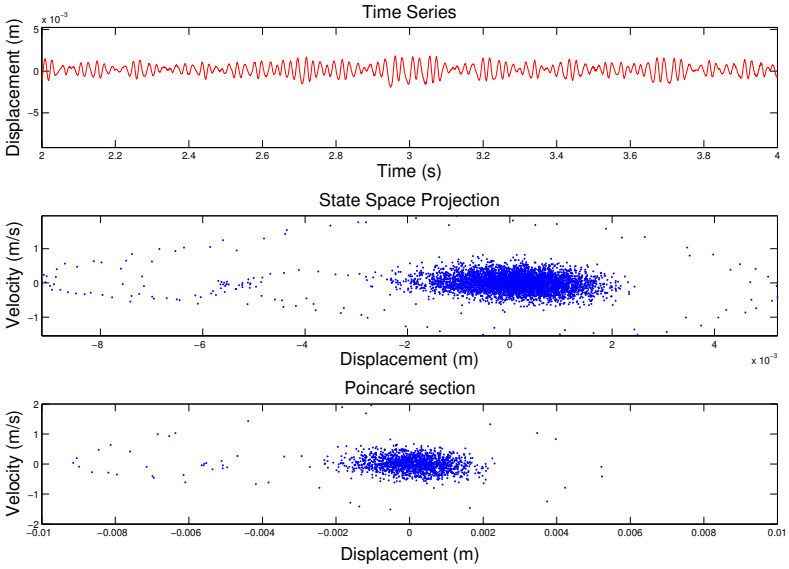

(a)

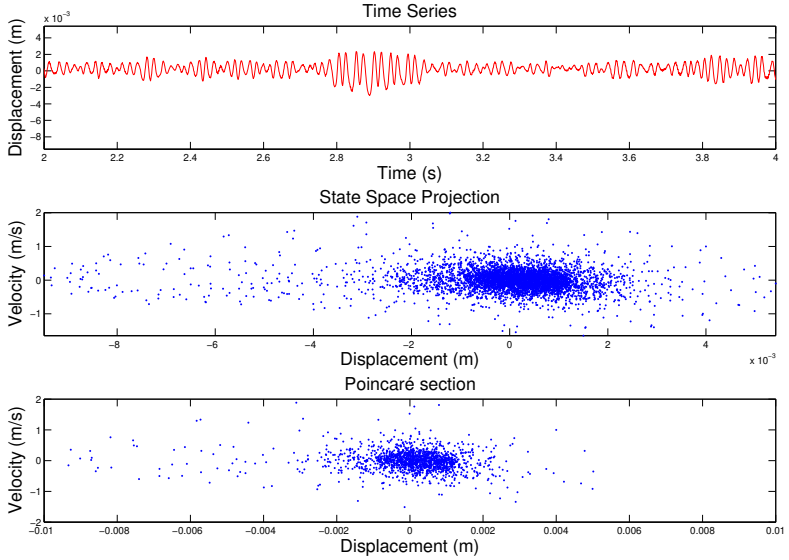

(b)

Figure 2.5: Experimental results: Softening Duffing oscillator response with (a) noise amplitude = 2 and (b) noise amplitude = 2.5. The excitation frequency f = 21.05 Hz for the deterministic input, whose level is the same in the cases with noise and without noise.

Having confirmed the presence of aperiodic motions for the deterministic case, the influence of noise on the system response has been considered. Different noise amplitudes were considered and the results obtained are quite revealing. As the white noise amplitude is increased from 0.1 units to 1 unit the response cloud slowly grows as shown in Figure 2.3(a) to Figure 2.4(a). However, beyond a certain noise level, a further increase in noise amplitude pushes the response towards a fixed point of the unforced system as shown in Figure 2.4(b) and Figure 2.5(a). From the results displayed in Figure 2.5(a), one can see the convergence of the motion towards one of the fixed points of the unforced system. These results support the findings reported in the earlier work of Perkins and Balachandran (2012), wherein it was shown that noise can be used to move the response of a Rayleigh-Duffing system from a chaotic

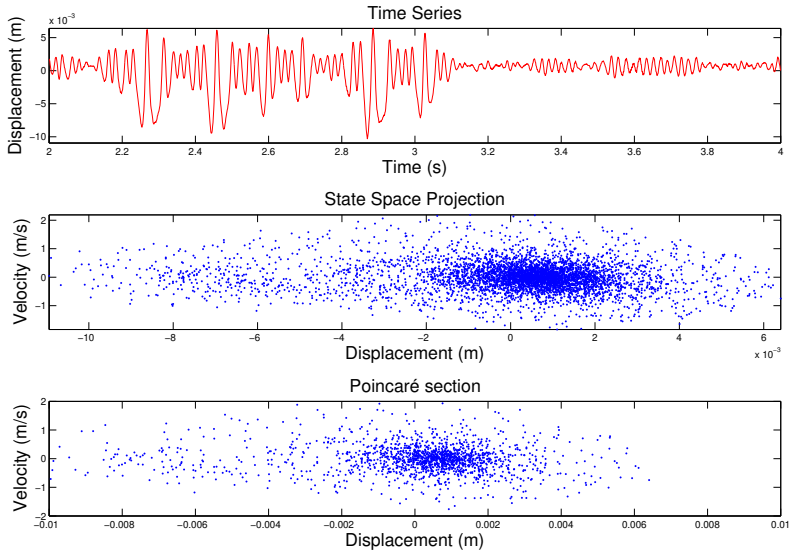

Figure 2.6: Experimental results: Softening Duffing oscillator response in the case with noise, noise amplitude = 3.5 units. The excitation frequency f = 21.05 Hz for the deterministic input, whose level is the same in the cases with noise and without noise.

Table 2.3: Parameter identification for hardening Duffing oscillator of experiments

Parameter	Value	Parameter	Value
ω_n	$2\pi \times 58.18$ rad/sec		
η	0.044	α	1
β	1	$\hat{F}_0$	0.0258

case to a non-chaotic case. As the author increases the noise amplitude further, the response cloud around a fixed point grows as shown in the Poincaré section in Figure 2.5(b) for noise amplitude of 2.5 units. The noise-influenced responses observed at higher noise levels are shown in Figure 2.5(b) and Figure 2.6.

2.3.2 Numerical Results

For one of the experimental configurations considered, which turned out to be a hardening case, the analytical frequency-response results obtained through are curve fitted to the normalized, deterministic frequency-response data from the experiments as shown in Figure 2.8(a). The parameter identification was done by using nonlinear curve-fitting in least-squares sense in MATLAB. The resulting parameter values are given in Table 2.3.

As reported in prior literature (Mallik, 2008), this system can experience chaotic behavior around one third of the system natural frequency at large amplitudes of excitation. The numerical results obtained at a low level forcing amplitude are shown in Figure 2.7(a); the response is periodic. At a high amplitude of excitation, the system behaves chaotically as shown in Figure 2.7(b).

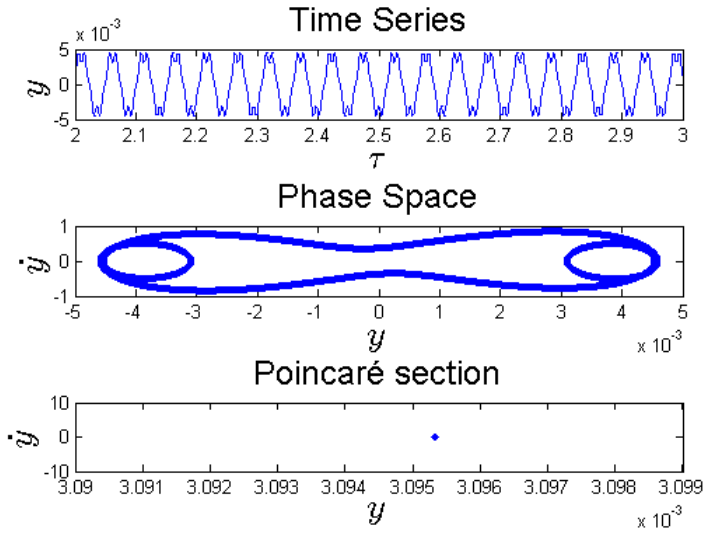

(a)

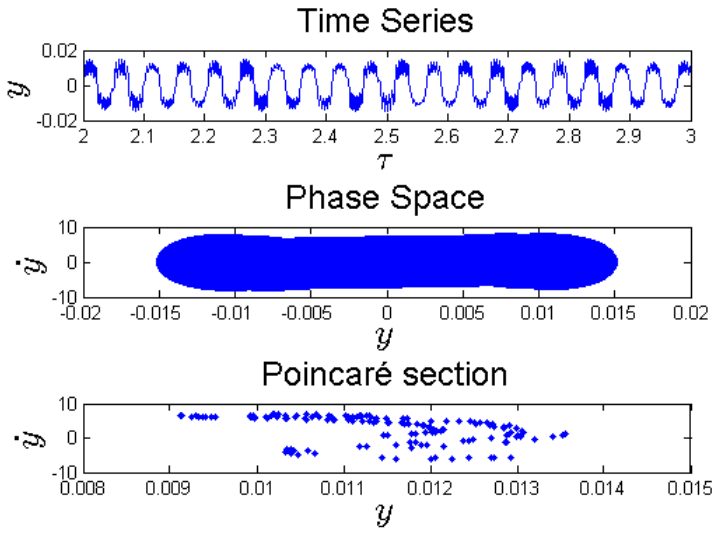

(b)

Figure 2.7: Numerical results: Hardening Duffing oscillator response in the case without noise and excitation frequency close to one third of natural frequency of the system. (a) The system shows periodic behavior at a low excitation level. (b) The system shows aperiodic behavior at a high excitation level.

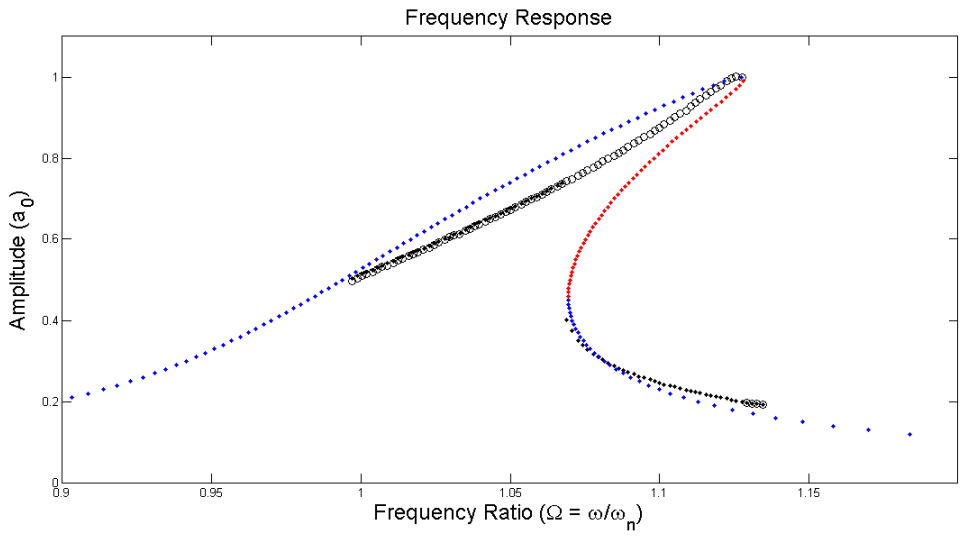

(a)

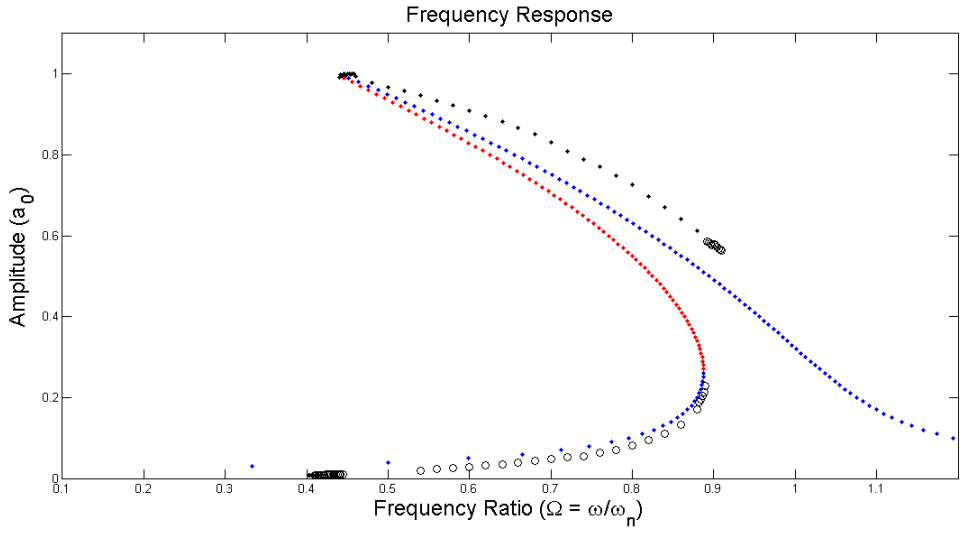

(b)

Figure 2.8: (a)Frequency-response of hardening Duffing oscillator. Black points represent experimental data and blue and red points correspond to numerical results for $k_1 = 2397.9$ N/m, $k_3 = 35450.60$ N/m^3, $\eta = 0.044$, and F = 16.0 N. (b) Frequency-response of soft Duffing oscillator. Black points represent experimental data and blue and red points correspond to numerical results for $\eta = 0.044$ and $\hat{F}_0 = 0.0231$.

Table 2.4: Parameter identification for bistable, softening Duffing oscillator of experiments

Parameter	Value	Parameter	Value
ω_n	$2\pi \times 50$ rad/sec		
η	0.044	α	-1
β	1	$\hat{F}_0$	0.0231

This level of excitation would be difficult to realize in the experimental system. However, the numerical results should help extend the experimental findings to other parameter regimes.

For the softening case, the experimental results obtained for the frequency-response of the system is shown in Figure 2.8(b). The parameter identification was carried out by using nonlinear curve-fitting in least-squares sense in MATLAB. The resulting parameter values are given in Table 2.4.

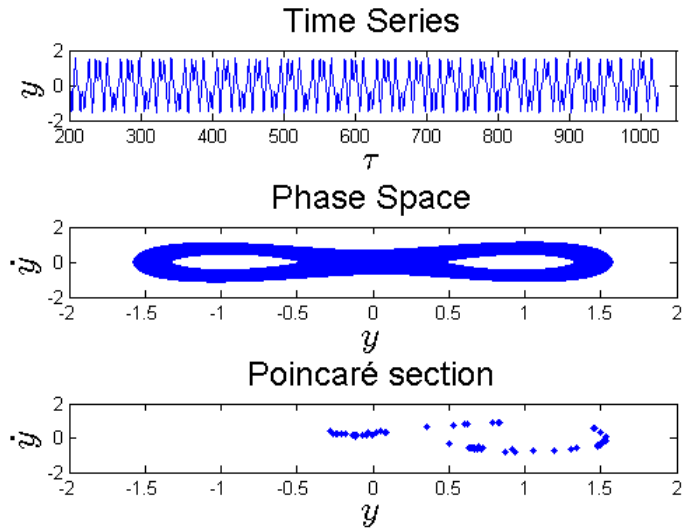

Figure 2.9: Numerical results: Softening Duffing oscillator response in the case without noise and deterministic harmonic excitation: chaotic behavior at excitation frequency f = 21.05 Hz.

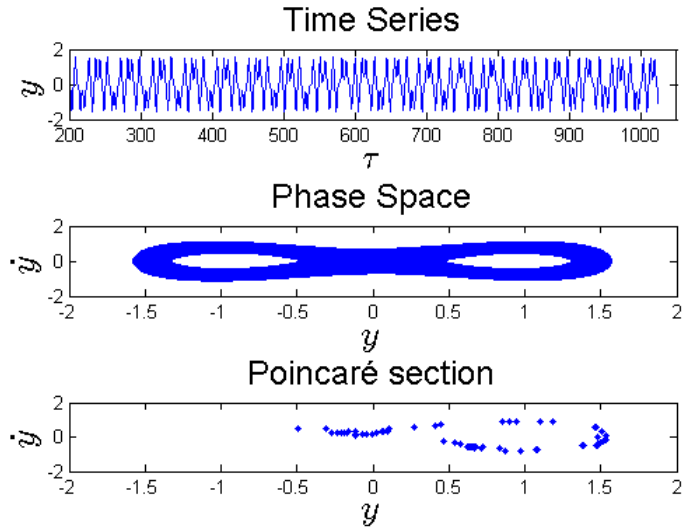

(a)

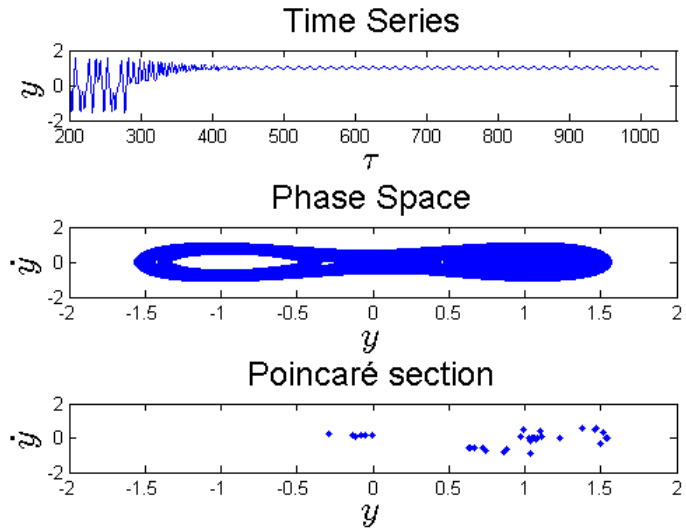

(b)

Figure 2.10: Numerical results: Softening Duffing oscillator response in the case with noise, (a) noise amplitude = 0.00001 units and (b) noise amplitude = 0.0001 units. The excitation frequency f = 21.05 Hz for the deterministic input, whose level is the same in the cases with noise and without noise.

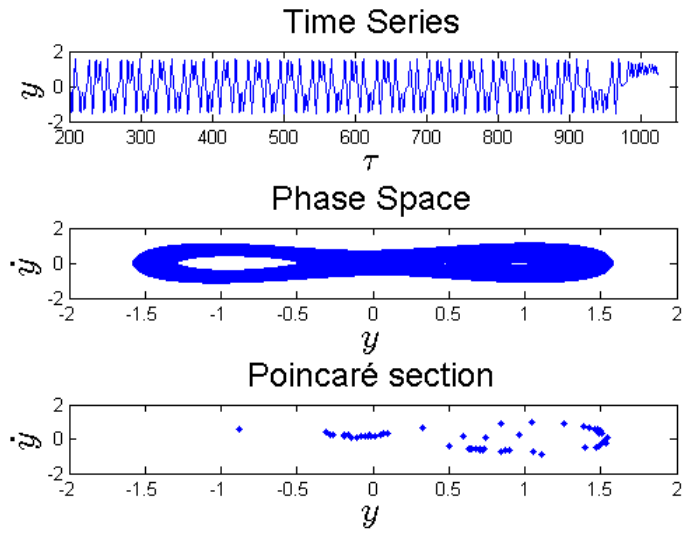

(a)

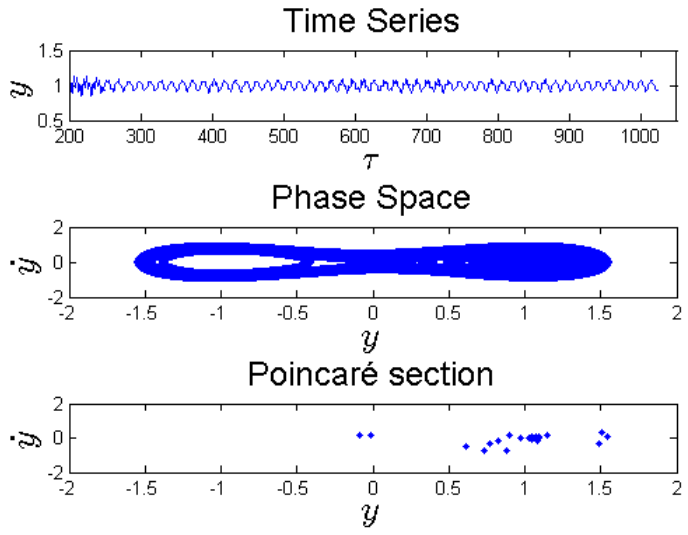

(b)

Figure 2.11: Numerical results: Softening Duffing oscillator response in the case with noise, (a) noise amplitude = 0.001 units and (b) noise amplitude = 0.005 units. The excitation frequency f = 21.05 Hz for the deterministic input, whose level is the same in the cases with noise and without noise.

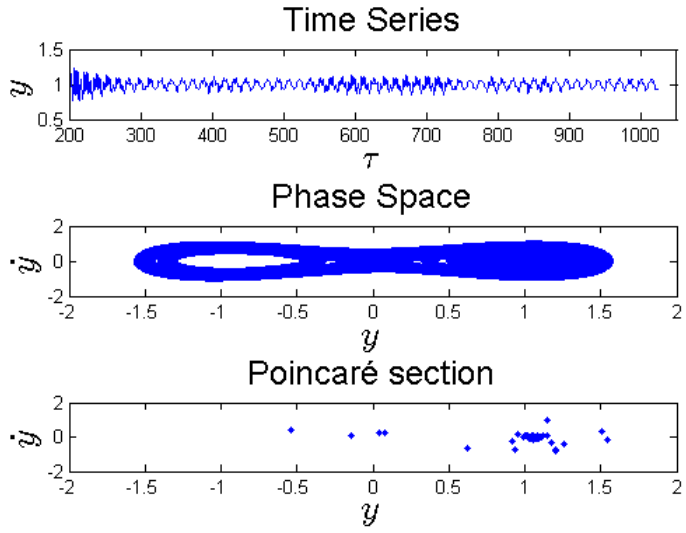

(a)

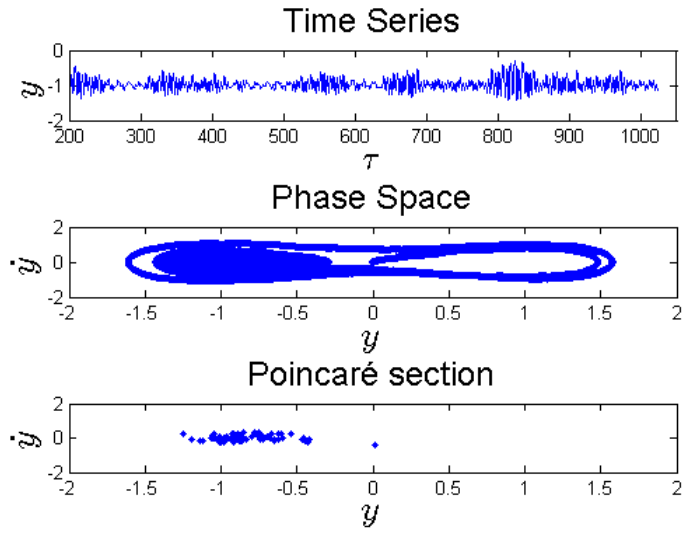

(b)

Figure 2.12: Numerical results: Softening Duffing oscillator response in the case with noise, (a) noise amplitude = 0.01 units and (b) noise amplitude = 0.05 units. The excitation frequency f = 21.05 Hz for the deterministic input, whose level is the same in the cases with noise and without noise.

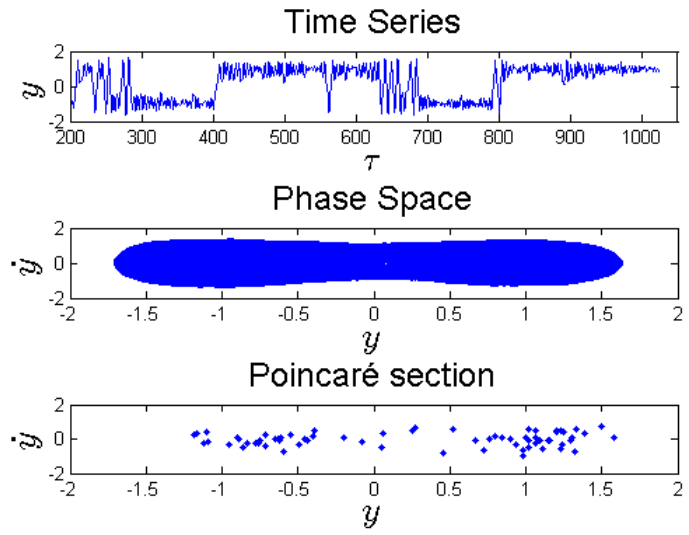

(a)

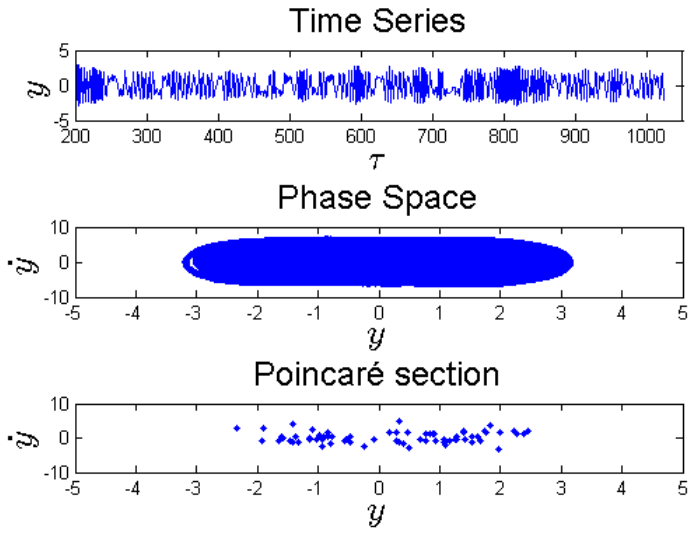

(b)

Figure 2.13: Numerical results: Softening Duffing oscillator response in the case with noise, (a) noise amplitude = 0.1 units and (b) noise amplitude = 0.5 units. The excitation frequency f = 21.05 Hz for the deterministic input, whose level is the same in the cases with noise and without noise.

The numerical response of soft Duffing oscillator around excitation frequency of 21.05 Hz for $\alpha = 1$ and high forcing level ($\hat{F}_0 = 0.118$) is shown in Figure 2.9. Next, noise is included in the system input. The numerical results obtained for the different noise levels are shown in Figure 2.10(a) to Figure 2.13(b). As the nondimensional noise level is increased from 0.00001 units to 0.005 units, the response gradually moves towards a fixed point of the unforced system as shown in Figure 2.10(a) to Figure 2.11(b). From the results shown in Figure 2.11(b), one can discern the convergence of the motion towards one of the fixed points of the unforced system. As the noise amplitude has been increased further, the response cloud around a fixed point was found to grow as illustrated in Figure 2.12(a) to Figure 2.13(b). It is mentioned that all system parameters presented in Figure 2.8(a) to Figure 2.13(b) are nondimensional. The numerical results support the findings of the experiments.

2.4 Influence of Noise on Frequency-Responses of Softening Duffing Oscillators

In this section, the influence of noise on the responses of continuous-time dynamical systems are considered. In particular, the influence of white Gaussian noise on the frequency-responses of monostable and bistable, softening Duffing oscillators are studied. A combination of experimental, analytical, and numerical studies are undertaken to understand the shifting of jump-up and jump-down frequencies and an eventual collapse of upper and lower responses branches of into one response

Table 2.5: Parameter identification for monostable, softening Duffing oscillator of experiments

Parameter	Value	Parameter	Value
ω_n	$2\pi \times 61.28$ rad/sec		
η	0.035	α	1
β	-0.4	$\hat{F}_0$	0.035

curve with no jump instabilities for the considered Duffing oscillator. It is noted that with noise, the hysteresis observed in the response of the nonlinear oscillator without noise can be destroyed.

2.4.1 Numerical Results

For monostable, softening Duffing oscillator, the analytical frequency-response results obtained through equation (2.5) are curve fitted to the normalized, deterministic frequency-response data from the experiments as shown in Figure 2.14(a). The resulting parameter values are given in Table 2.5. On the other hand, for bistable, softening Duffing oscillator, the analytical frequency-response results obtained through equation (2.14) are curve fitted to the normalized, deterministic frequency-response data obtained from the experiments as shown in Figure 2.14(b). The resulting parameter values are given in Table 2.6. These parameters are used for numerical simulations under the influence of noise that is discussed in this section.

The Euler–Maruyama method have been used to obtain numerical solutions of equation (2.17) in order to study the changes in the frequency-response curve of a Duffing oscillator with softening characteristics with variation of noise amplitude σ_N.

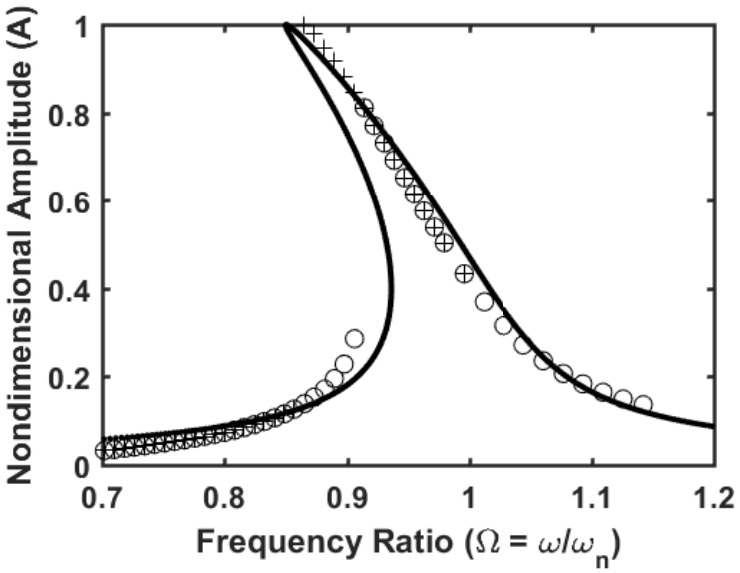

(a) Monostable Softening Duffing Oscillator

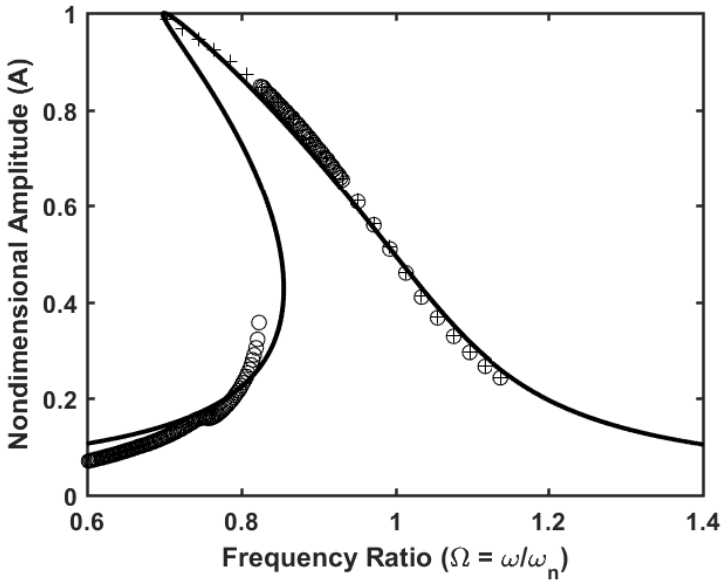

(b) Bistable Softening Duffing Oscillator

Figure 2.14: Plots of experimentally and numerically obtained frequency-response curves for softening Duffing oscillators. The sweep-up points (increasing excitation frequency) are shown by circles and sweep-down points (decreasing excitation frequency) are shown by the symbol " + ". The analytically predicted frequency-response is curve fitted to experimental data. In plot (a), the authors show the normalized, deterministic frequency-response of a monostable, softening Duffing oscillator along with the analytic frequency-response generated by using equation (2.5). In plot (b), the normalized, deterministic frequency-response of a bistable, softening Duffing oscillator has been shown along with the analytic frequency-response generated by using equation (2.14).

Table 2.6: Parameter identification for bistable, softening Duffing oscillator of experiments

Parameter	Value	Parameter	Value
ω_n	$2\pi \times 48.34$ rad/sec		
η	0.085	α	-0.5
β	0.2	$\hat{F}_0$	0.085

The linear natural frequencies ω_n for both the monostable and the bistable softening Duffing oscillators are obtained from a low amplitude impulse response test about their respective equilibrium positions. The rest of the parameters are obtained from free oscillation data and from curve fitting of the experimental obtained deterministic frequency-response curve to the analytical frequency-response curve, which are given by equations (2.5) and (2.14). The values of the corresponding parameters obtained for both the monostable and the bistable Duffing oscillator are shown in Table 2.5 and Table 2.6, respectively.

For numerical simulations, the author chose the initial conditions corresponding to different branches of the frequency-response curves obtained for the deterministic case. Different initial conditions representing different branches are obtained from the associated basins of attraction at a particular forcing frequency. In the current work, for each of the monostable and bistable cases, two different initial conditions have been chosen corresponding to sweep-up (lower branch as represented by circles in Figure 2.14) and sweep-down (upper branch as by symbol " + " in Figure 2.14). Note that the same initial conditions for deterministic and stochastic simulations were also assumed. For a monostable, Duffing oscillator with softening characteristic, $(0, 0)$ is one of the initial conditions corresponding to the

sweep-up frequency-response branch, and $(0, 1.03)$ is one of the initial conditions corresponding to the sweep-down frequency-response branch. Similarly, for a bistable, Duffing oscillator with softening characteristics, $(-1.4, 0)$ is one of the chosen initial conditions, which corresponds to the the sweep-up frequency-response branch, and $(-1.814, 0.6914)$ is one of the chosen initial conditions, which corresponds to the sweep-down frequency-response branch.

The numerical results are obtained by solving the state-space form given by equations (2.17). The numerical simulation results are produced with the same initial conditions, same forcing vector and by averaging 100 Euler-Maruyama simulations in the time domain over 300 time periods. At each particular forcing frequency, each of these Euler-Maruyama simulations has the same noise amplitude σ_N, but different noise vectors. The time domain averaging results in an average displacement response at a particular forcing frequency and the amplitude of the average displacement response has been chosen which represents one of the points on the frequency-response curve. The resulting frequency-response curve is produced by combining the results obtained for all the forcing frequencies. In Figure 2.17, the numerical results obtained for the monostable case are shown, and in Figure 2.18, the numerical results obtained for the bistable, Duffing oscillator are shown.

For both monostable and bistable cases, the frequency-response curves with $\sigma_N = 0$ are shown in Figure 2.17(a) and Figure 2.18(a), respectively. These results are obtained from Euler-Maruyama simulations in the time domain with the chosen initial conditions. The outcomes can be compared with the frequency-response curve obtained from deterministic experiment and analytical solution shown in Figures

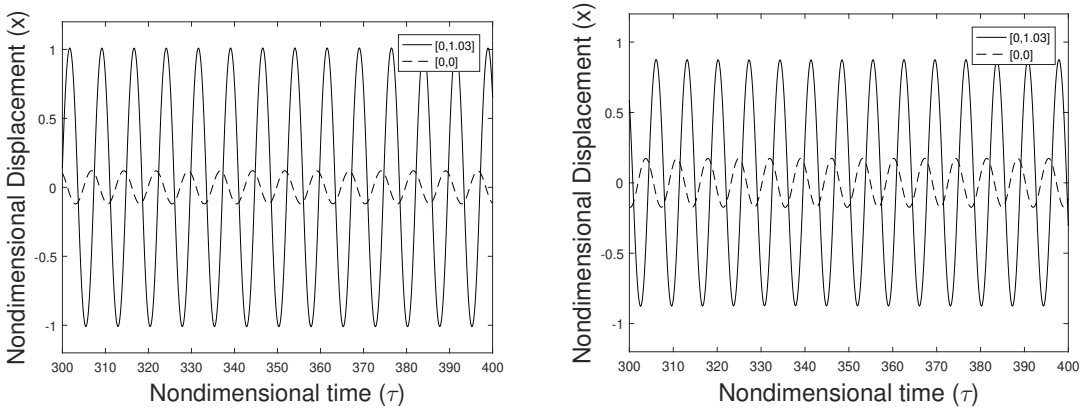

(a) $\Omega = 0.85$ (b) $\Omega = 0.89$

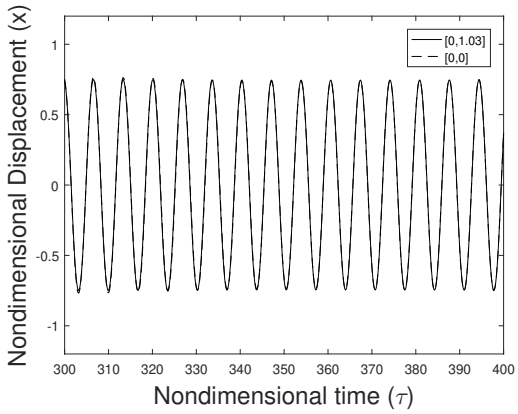

(c) $\Omega = 0.93$

Figure 2.15: Time series for monostable, softening Duffing oscillator responses for three different driving frequencies with the initial conditions $(0, 0)$ and $(0, 1.03)$ corresponding to the bottom branch and top branch of the frequency-response curve, respectively. In plot (a), the authors show the time series at the jump-up frequency; there is a small response amplitude for the initial condition $(0, 0)$ and a large response amplitude for the initial condition $(0, 1.03)$. In plot (b), the time series at an intermediate frequency between jump-down frequency and jump-up frequency has been shown. At this particular frequency, the initial condition $(0, 0)$ results in a small response amplitude and the initial condition $(0, 1.03)$ results in a large response amplitude. In plot (c), the time series at the jump-up frequency has been shown. At this particular frequency, both the initial conditions result in the same response amplitude.

2.14(a)-(b). For the monostable system, the jump phenomenon is observed at $\Omega = 0.85$ and at $\Omega = 0.93$, which can also be verified from the time series obtained for these initial conditions at the forcing frequency $0.85 \leq \Omega \leq 0.93$, as shown in Figure

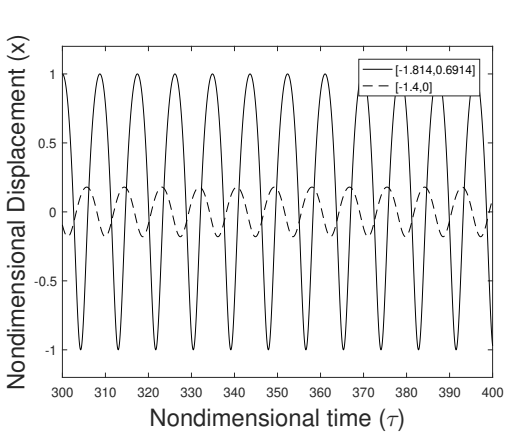

(a) $\Omega = 0.70$

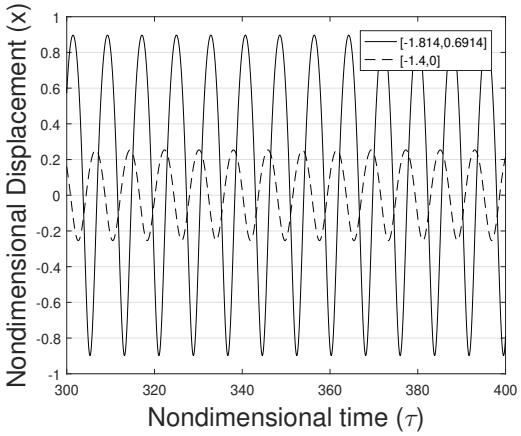

(b) $\Omega = 0.80$

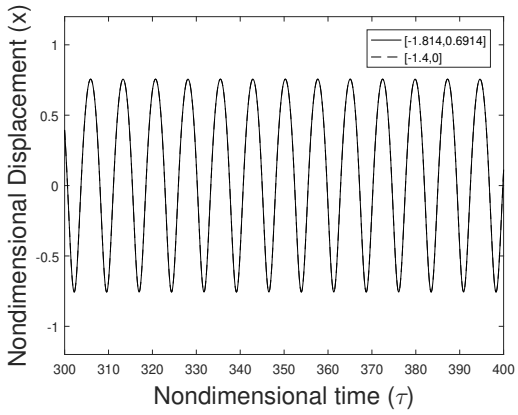

(c) $\Omega = 0.85$

Figure 2.16: Time series for bistable, softening Duffing oscillator responses for three different driving frequencies with the initial conditions $(-1.4, 0)$ and $(-1.8140, 0.6914)$ corresponding to the bottom branch and top branch of the frequency-response curve, respectively. In plot (a), the authors show the time series at the jump-up frequency; there is a small response amplitude for the initial condition $(-1.4, 0)$ and a large response amplitude for initial condition $(-1.8140, 0.6914)$. In plot (b), the time series at an intermediate frequency between jump-down frequency and jump-up frequency has been shown. At this particular frequency, the initial condition $(-1.4, 0)$ results in a small response amplitude and the initial condition $(-1.8140, 0.6914)$ results in a large response amplitude. In plot (c), the time series at the jump-up frequency has been shown. At this particular frequency, both initial conditions result in the same response amplitude.

2.15. The time series shown in Figures 2.15(a)-(b) correspond to two different response outputs with different displacement amplitudes. On the other hand, in Figure 2.15(c), there is one response curve for both initial conditions. Similarly, for the bistable case, the time series obtained at three different forcing frequencies are shown in Figures 2.16(a)-(c).

The region of the frequency-response curve having two stable solution or the region between the two jump frequencies is called as the hysteresis region. The addition of noise to the system affects the hysteresis region by shifting the "jump" frequencies.

For a monostable, Duffing oscillator with softening characteristics, a small increment in noise amplitude σ_N doesn't affect the top branch of the frequency-response curve but this noise addition pushes the lower branch near the jump-up frequency towards the upper branch as shown in Figure 2.17(b). A further increase in noise amplitude σ_N moves the jump-down and jump-up frequencies towards each other, which results in reduction of the hysteresis region as shown in Figures 2.17(c)-(h). A large noise amplitude destroys the hysteresis region by merging the jump-up and jump-down frequencies and the resulting response has only one peak as shown in Figure 2.17(h). The frequency-response curve looks almost linear with an asymmetric amplitude peak. This system has one stable potential well (Kovacic and Brennan, 2011). Furthermore, the increase in noise amplitude σ_N pushes the system response out of the stable potential well towards the unstable region and the numerical simulations do not help generate frequency-response data. As shown in Figure 2.17(i), the frequency-response curve has no data at few of the forcing

frequencies (missing symbols " + " for $0.85 \leq \Omega \leq 0.92$).

For a bistable, Duffing oscillator with softening characteristics, an increase in noise amplitude σ_N moves the jump-down and jump-up frequencies towards each other, which results in reduction of the hysteresis region as shown in Figures 2.18(b)-(f). A large noise amplitude destroys the hysteresis region by merging the jump-up and jump-down frequencies and the reponse has only one peak as shown in Figure 2.18(f). The frequency-response curve looks almost linear with an asymmetric amplitude peak. With a further increase in noise amplitude σ_N, the result is a cluster of points in the frequency-response curve as shown in Figures 2.18(g)-(h). The bistable, Duffing oscillator system has two stable potential wells (Kovacic and Brennan, 2011). With a further increase in noise amplitude σ_N, the system response is pushed from one stable potential well to another potential well. The numerical results corresponding to the jump from one potential well to another have not been presented here. The numerical path integration procedure (Yu and Lin, 2004; Hanggi and Riseborough, 1983) based on the Gauss-Legendre integration rule was used to compute the evolution of probability density subjected to a harmonic and a white Gaussian excitation. The periodicity of probability density function implies a steady state response. This procedure has been used to find out the noise amplitude limit, for which there is no jump between the two potential wells. Here, with a noise amplitude $\sigma_N \leq 0.05$, there is no jump observed in the system response from one potential well to another. For a noise amplitude $\sigma_N \geq 0.06$, there is a small probability that system response will jump from one potential well to another potential well. The corresponding contour plots with two different noise amplitudes

are shown in Figure 2.21.

A comparison of numerical results with experimental findings is made in the next section.

2.4.2 Experimental Results

The experimental results are obtained by conducting quasi-static frequency sweeps for increasing and decreasing excitation frequencies. In Figure 2.19 and Figure 2.20, the frequency-response curves of a monostable and a bistable Duffing oscillator are respectively shown. The experiments were conducted to cover the hysteresis region. In the numerical studies, the noise is assumed to be a white Gaussian noise. On the other hand, in the experiments, the noise is assumed to be a band limited white noise. The spectrum of the experimental noise has a constant power density in the operating frequency range of interest, and in this range, this noise may be treated as being equivalent to a white noise. Qualitative comparisons between experimental results and numerical results are made in this section.

For a monostable, softening Duffing oscillator, a small increment in the noise amplitude σ_E doesn't result in changes in the jump-down frequency and the upper branch of the frequency-response curve. However, the lower branch of the frequency-response curve near the jump-up frequency is slightly moved towards the upper branch of the frequency-response curve and the jump-up frequency is shifted to the left as shown in Figures 2.19(b)-(c). These results can be compared with the numerical results shown in Figure 2.17(b). A further increase in noise amplitude

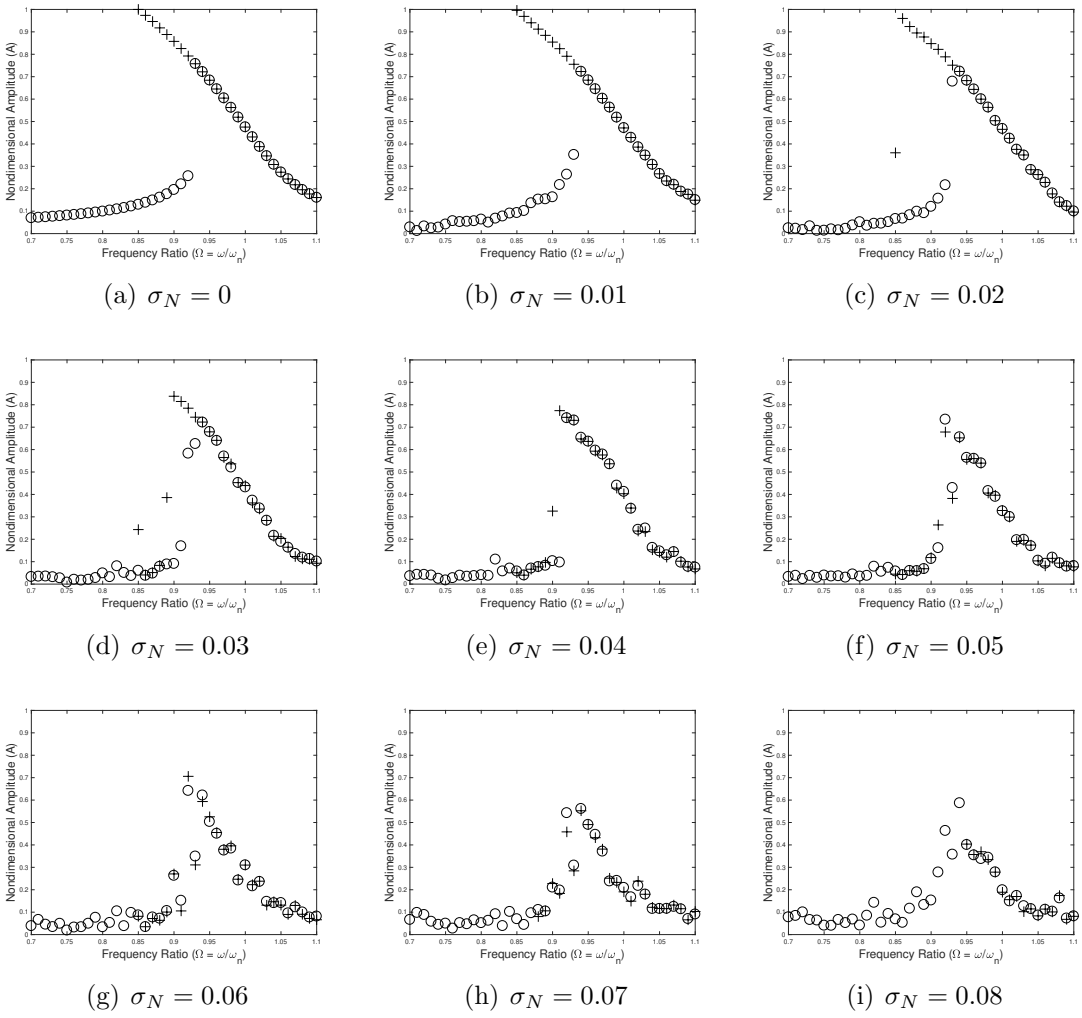

(a) $\sigma_N = 0$ (b) $\sigma_N = 0.01$ (c) $\sigma_N = 0.02$

(d) $\sigma_N = 0.03$ (e) $\sigma_N = 0.04$ (f) $\sigma_N = 0.05$

(g) $\sigma_N = 0.06$ (h) $\sigma_N = 0.07$ (i) $\sigma_N = 0.08$

Figure 2.17: Frequency-response curves obtained through numerical simulation of monostable, softening Duffing oscillator dynamics. Corresponding system parameter values chosen are shown in Table 2.5. In plot (a), the circles correspond to the sweep-up branch of frequency-response curve obtained from the initial condition $(0, 0)$. The points marked by the symbol "$+$" correspond to the sweep-down branch of the frequency-response curve obtained from the initial condition $(0, 1.03)$. This plot may be compared with Figure 2.14(a). The associated time series are shown in Figure 2.15. The plots (b)-(i) are obtained from the averaged dynamics for the same initial conditions as those used for the deterministic case.

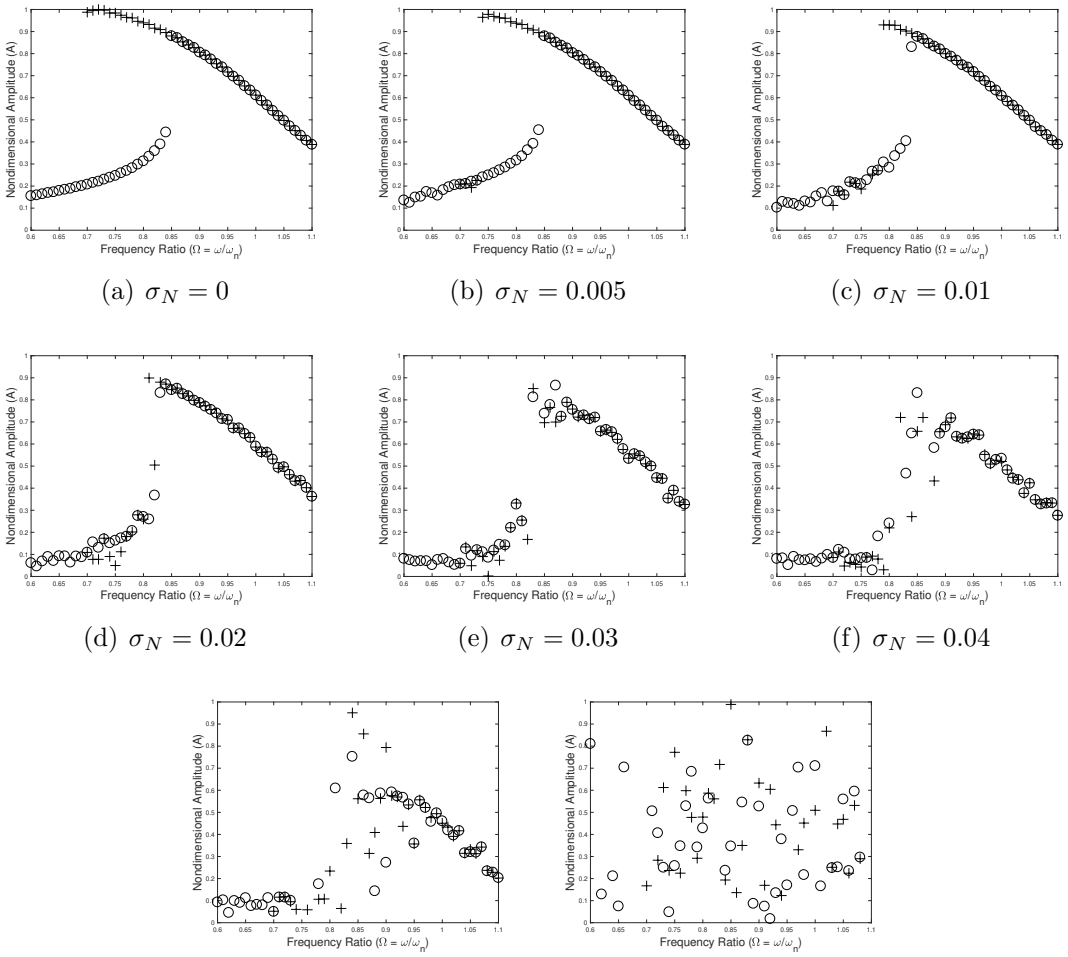

(a) $\sigma_N = 0$ (b) $\sigma_N = 0.005$ (c) $\sigma_N = 0.01$

(d) $\sigma_N = 0.02$ (e) $\sigma_N = 0.03$ (f) $\sigma_N = 0.04$

(g) $\sigma_N = 0.05$ (h) $\sigma_N = 0.1$

Figure 2.18: Frequency-response curves obtained through numerical simulations of bistable, softening Duffing oscillator dynamics. Corresponding system parameter values chosen are shown in Table 2.6. In plot (a), the circles correspond to the sweep-up branch of frequency-response curve obtained from the initial condition $(-1.4, 0)$. The points marked by the symbol " $+$" correspond to the sweep-down branch of the frequency-response curve obtained from the initial condition $(-1.814, 0.6914)$. This plot may be compared with Figure 2.14(b). The associated time series are shown in Figure 2.16. The plots (b)-(h) are obtained from the averaged dynamics for the same initial conditions as those used for the deterministic case.

σ_E results in movement of the jump-down and jump-up frequencies towards each other and a slight move of the upper and lowers branches towards each other; this results in reduction of the hysteresis region as shown in Figures 2.19(d)-(f). These experimental findings are in agreement with the numerical results shown in Figures 2.17(c)-(g). Similar to the numerical results shown in Figure 2.17(h), a large noise amplitude leads to destruction of the hysteresis region through merger of the jump-up and jump-down frequencies. The resulting response has only one peak as shown in Figure 2.19(f), and the frequency-response curve looks almost linear with an asymmetric amplitude peak. Noting that a monostable, Duffing oscillator system with softening characteristic has one stable potential well, a further increase in noise amplitude σ_N pushes the system response out of the stable potential well towards the unstable region and the experiments could not be continued as the system response is moved to an unstable region.

For a bistable, Duffing oscillator with softening characteristic, an increase in the noise amplitude σ_N leads to a movement of the jump-down and jump-up frequencies towards each other, resulting in a reduction of the hysteresis region as shown in Figure 2.20(b). A similar pattern is also seen in the numerical results with respect to increments in the noise amplitude σ_N, as seen in Figures 2.18(b)-(e). Similar to what was observed with the numerical results of Figure 2.18(e), a large noise amplitude level results in destruction of the hysteresis region through merger of the jump-up and jump-down frequencies. The resulting response has only one peak as shown in Figures 2.18(b)-(c), and the frequency-response curve looks almost linear with an asymmetric amplitude peak. With a further increase in noise

amplitude σ_E, the result is a cluster of points in the frequency-response curve as shown in Figures 2.19(c)-(e). This is quite similar to what the author observed in the numerical results shown in Figures 2.18(g)-(h). As a bistable, softening Duffing oscillator has two stable potential wells, with a further increase in the level of noise amplitude σ_E, the system response jumps from one stable potential well to another potential well. For a large level of noise, the experimental findings reveal a jump from one potential well to another.

In the case of the bistable Duffing oscillator arrangement, it should be noted that the amplitude of noise σ_E needed to destroy the hysteresis region is much lower than the noise amplitude level required for a monostable, softening Duffing oscillator.

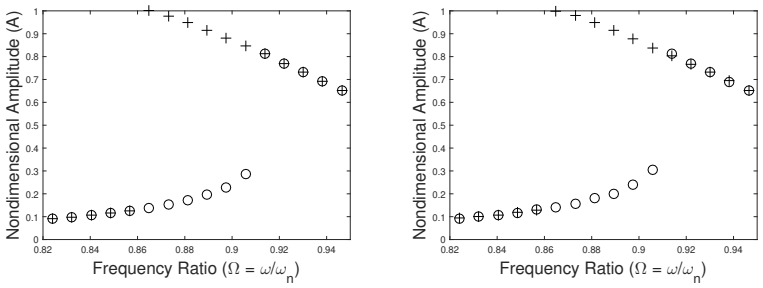

(a) $\sigma_E = 0$ (b) $\sigma_E = 0.5$

(c) $\sigma_E = 1.0$ (d) $\sigma_E = 1.5$

(e) $\sigma_E = 2.0$ (f) $\sigma_E = 3.0$

(g) $\sigma_E = 4.0$

Figure 2.19: Frequency-response curves obtained in experimental study of monostable, softening Duffing oscillator under the influence of white Gaussian noise for different levels of noise amplitude σ_E. The experimental data are normalized with the maximum amplitude of the corresponding, deterministic frequency-response curve. These results can be compared with the results presented in Figure 2.17.

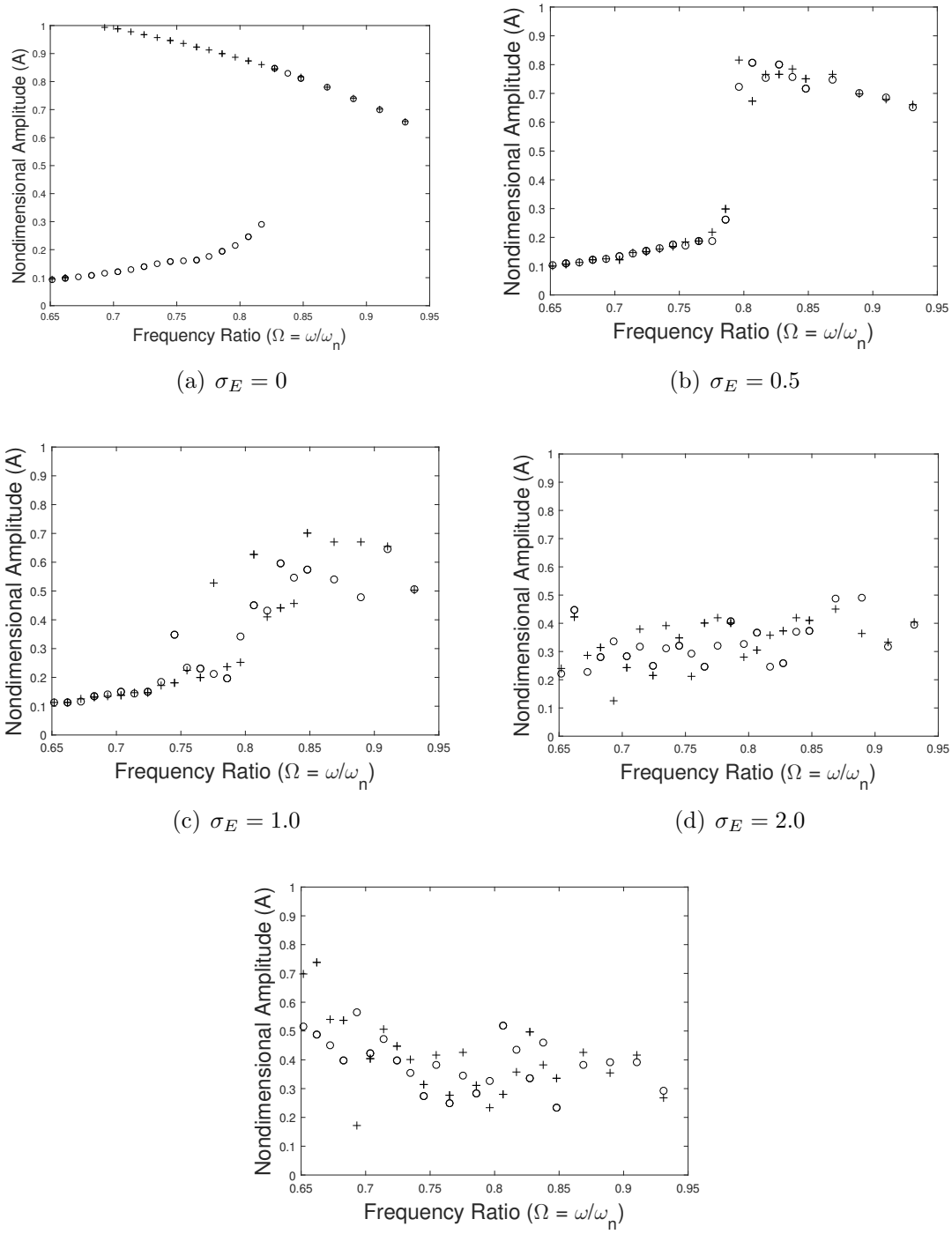

(a) $\sigma_E = 0$

(b) $\sigma_E = 0.5$

(c) $\sigma_E = 1.0$

(d) $\sigma_E = 2.0$

(e) $\sigma_E = 3.0$

Figure 2.20: Frequency-response curves obtained in experimental study of bistable, softening Duffing oscillator under the influence of white Gaussian noise for different levels of noise amplitude σ_E. The experimental data are normalized with the maximum amplitude of the corresponding, deterministic frequency-response curve. These results are compared with the results presented in Figure 2.18.

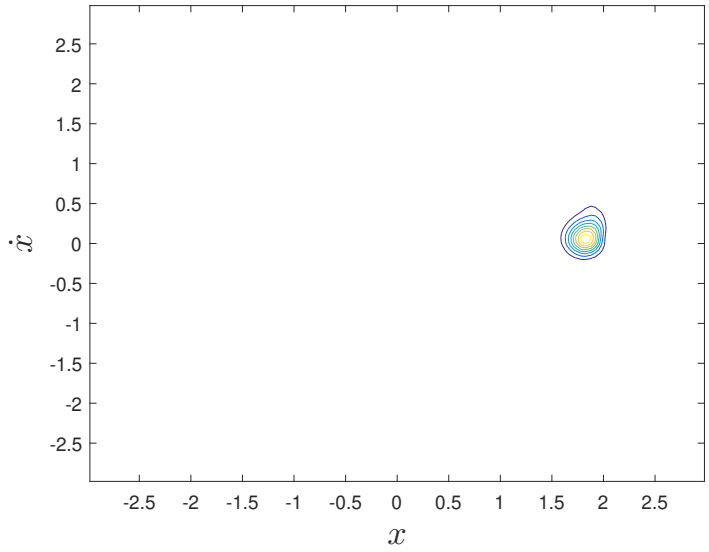

(a) $\sigma_N = 0.05$

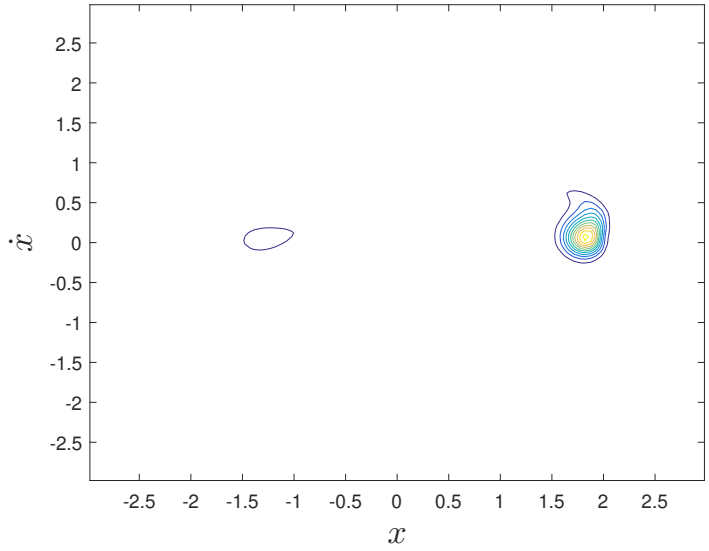

(b) $\sigma_N = 0.06$

Figure 2.21: Contour plots of probability density of a bistable, softening Duffing oscillator (equation (2.15) and Table 2.6). The numerical path integration procedure based on the Gauss-Legendre integration rule is used to compute the evolution of probability density subjected to a harmonic and a white Gaussian excitation. The periodicity of probability density function implies a steady state response. With a noise amplitude $\sigma_N \leq 0.05$, there is no jump in the system response from one potential to the other. For a noise amplitude $\sigma_N \geq 0.06$, there is a small probability that the system response will jump from one potential well to the other potential well.

2.5 Noise-Induced Chaotic-Attractor Escape Route

The influence of white Gaussian noise on the chaotic and periodic responses of bistable, Duffing oscillators is the focus of this section. The noteworthy result of the conducted studies concerns the presence of a pair of attractors, one being periodic and the other being chaotic: the chaotic attractor response can be controlled and terminated with an appropriate noise level. For trajectories in the basin of the chaotic attractor, white Gaussian noise is added at a barely sufficient level to allow trajectories to eventually leave (within some specified time). The author reports that trajectories leave via a special escape route: the unstable manifold of a fixed point saddle on the basin boundary between the two basins of attraction.

2.5.1 Numerical Results

Getting chaos for numerical studies. For the numerical simulations, the parameters have been chosen so that the deterministic response of the system shows the existence of a chaotic attractor as well as stable periodic attractor. To carry this out, after parametric identification, the forcing amplitude F_0 and forcing frequency Ω have been varied over sufficient ranges to observe the chaotic response. The numerically obtained bifurcation diagrams along with Lyapunov spectrum are shown in Figure 2.22. It is clear that the system behaves chaotically for a range of parameter values. For this section, the author has chosen the parameter values as shown in Table 2.7 where the system dynamics is chaotic or periodic depending on the initial condition chosen. For these parameter values, the basin of attraction

Table 2.7: Parameter values for Duffing oscillator showing chaotic realizations

Parameter	Value	Oscillator	characteristic
η	0.085	F_0	0.204
α	-0.5	Ω	0.71
β	0.2		

along with time series is shown in Figure 2.23 and it confirms the existence of a chaotic attractor as well as a stable period-1 attractor.

Numerical simulations were conducted to study any qualitative change in dynamics of the Duffing oscillator with variation of noise amplitude σ_N while integrating equation 2.17. When the noise amplitude σ_N is varied, the rest of of the parameters are kept constant as shown in Table 2.7. The basin of attraction with these parameter values is shown in Figure 2.23. The steady state response of the deterministic system ($\sigma_N = 0$) is chaotic or periodic depending on the initial point chosen. For any initial condition in the purple region, the system response settles down on a chaotic attractor whereas, for any initial condition in the yellow region, the response settles down to a period-1 attractor. Both time series as well as the corresponding stroboscopic maps are shown in Figure 2.23. The numerical results are obtained by integrating the stochastic differential equations, equations (2.17), with the Euler–Maruyama scheme. The initial conditions and parameters used (Table 2.7) to produce the response shown in Figure 2.23, which is the deterministic case, were also used for all of the stochastic simulations as well. The numerical results are produced for more than 100 Euler-Maruyama simulations in the time domain over 1000 time periods. Each of these Euler-Maruyama simulations has the same

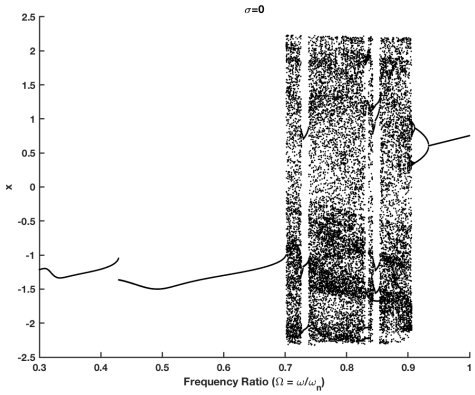

(a) Bifurcation Diagram for $F_0 = 0.204$

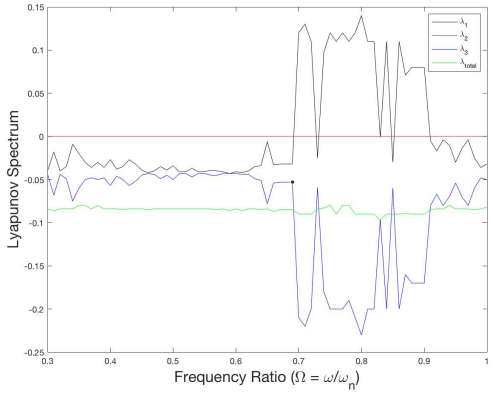

(b) Lyapunov Spectrum for $F_0 = 0.204$

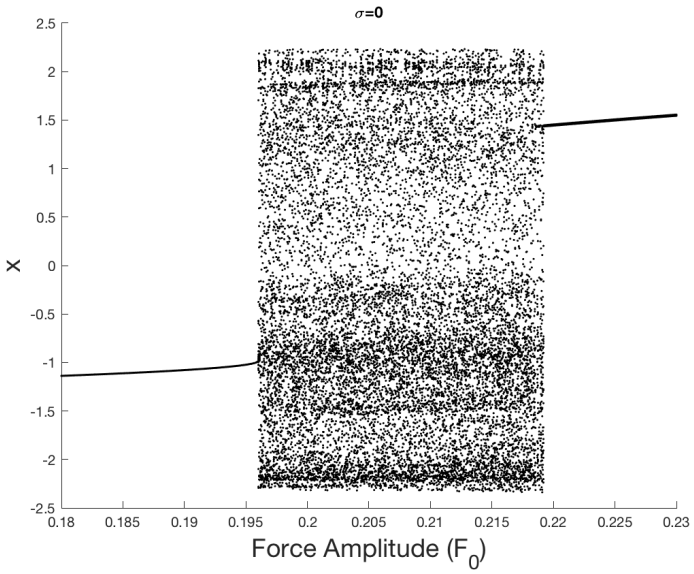

(c) Bifurcation Diagram for $\Omega = 0.71$

Figure 2.22: Plots of numerically obtained bifurcation diagram for softening Duffing oscillators in equation (2.13). In plot (a), the authors show a bifurcation diagram for a constant forcing amplitude ($F_0 = 0.204$). Plot (b) has the corresponding Lyapunov spectrum. A positive lyapunov exponent confirms a chaotic response. Plot (c) has the bifurcation diagram for a constant forcing frequency ($\Omega = 0.71$).

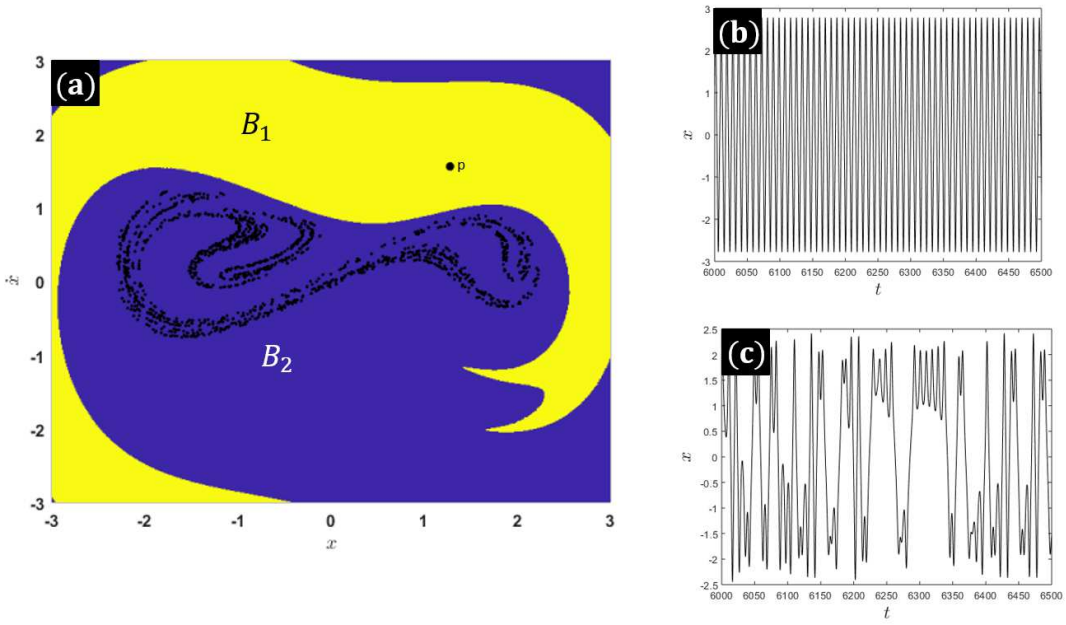

Figure 2.23: Numerical simulations using Euler-Maruyama scheme for noise amplitude $\sigma_N = 0$. See Table 2.7 for system parameter values. For the model, a chaotic attractor coexists with a periodic attractor. Plot (a) is for the stroboscopic map. Purple color (B_2) and yellow color (B_1) are used to identify the basins of attraction of the chaotic and periodic attractors, respectively. The black dots in the purple region are the (stroboscopic) chaotic attractor while point "P" is a fixed point attractor. In plots (b) and (c), the associated time series are shown.

noise amplitude σ_N, but a different noise vector.

Escaping chaos. Any qualitative change in the system dynamics depends on the noise amplitude σ_N. From the numerical results, one can see that for a noise amplitude $0 \leq \sigma_N < \sigma_c$, with any initial condition in the chaotic or periodic basin, the steady-state response settles down on a noisy chaotic attractor or a noisy periodic attractor respectively as shown in Figure 2.24. There are no qualitative changes observed in the system behavior. Here, σ_c represents the critical value of noise amplitude for which the chaotic attractor faces a crisis. At that critical noise amplitude σ_c, the chaotic attractor comes into contact with the stable manifold at the saddle point as shown in Figure 2.31(b) and the chaotic attractor vanishes.

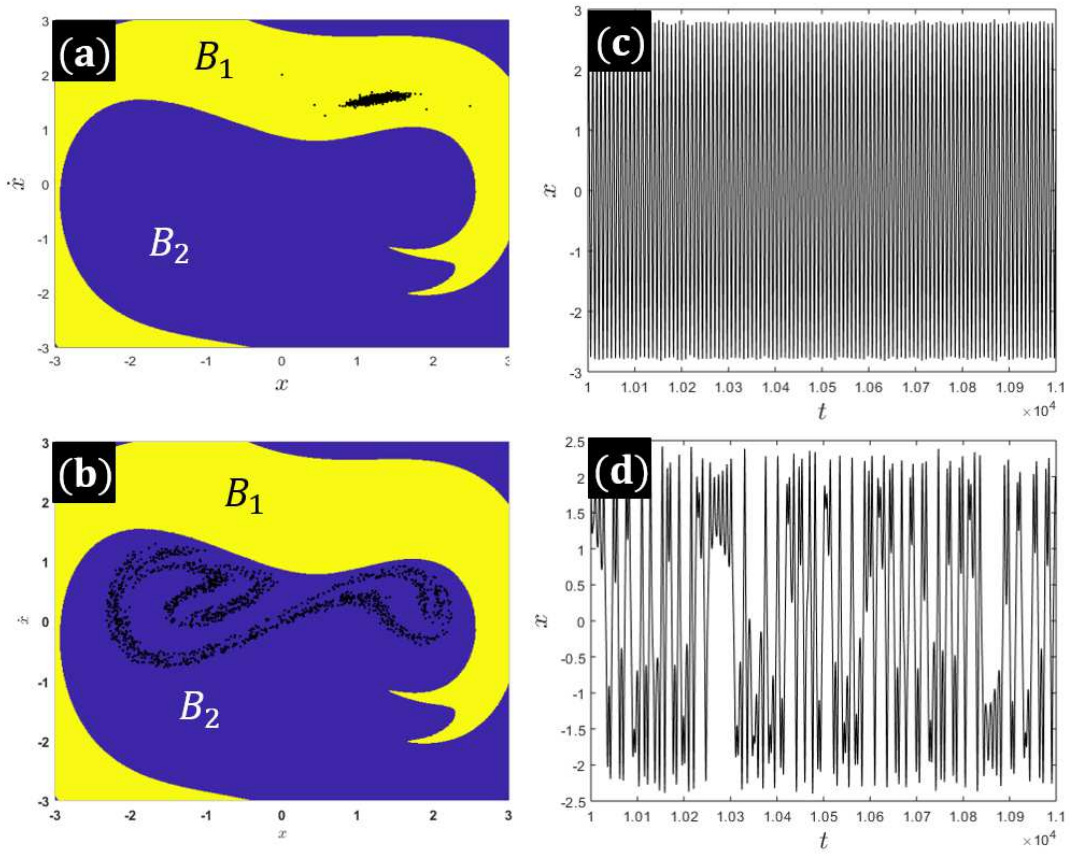

Figure 2.24: Numerical simulations using Euler-Maruyama scheme for noise amplitude $\sigma_N = 0.015$. See Table 2.7 for system parameter values. Purple color (B_2) and yellow color (B_1) are used to identify the basins of attraction of the chaotic and periodic attractors, respectively. The black dots in the purple region are the (stroboscopic) noisy chaotic attractor while black dots in the yellow region are the (stroboscopic) noisy periodic attractor. The black dots in plot (a) are the (stroboscopic) noisy attractor for an initial condition in the yellow region and plot (c) has the associated time series. The black dots in plot (b) are the (stroboscopic) noisy attractor for an initial condition in the purple region and plot (d) has the associated time series. The system dynamics exhibits no qualitative changes.

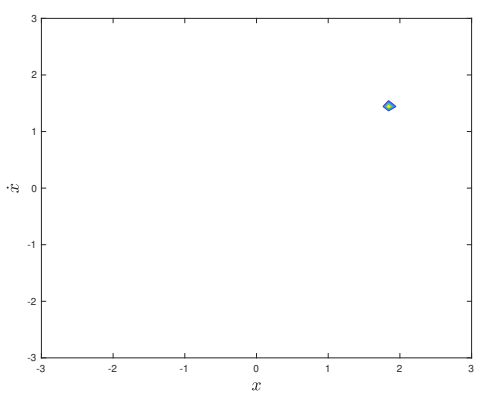

(a) $\sigma_N = 0.02$

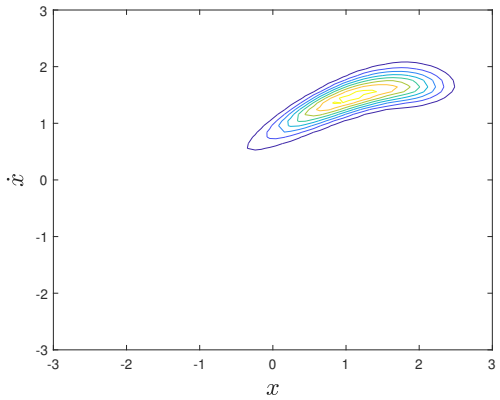

(b) $\sigma_N = 0.045$

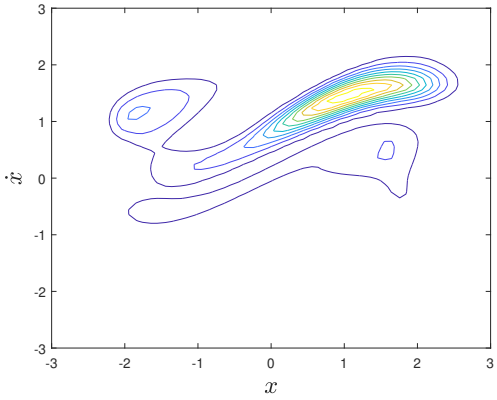

(c) $\sigma_N = 0.05$

Figure 2.25: Contour plots of probability density of a bistable, softening Duffing oscillator (equation (2.15)). See Table 2.7 for system parameter values. The numerical path integration procedure based on the Gauss-Legendre integration rule is used to compute the evolution of probability density subjected to a harmonic and a white Gaussian excitation. The periodicity of probability density function implies a steady state response. With a noise amplitude $\sigma_N < 0.02$, there is no jump in the system response from one attractor to another. With a noise amplitude $0.02 \leq \sigma_N < 0.05$, there is probability of the system response jumping from the chaotic attractor to the periodic attractor (fixed point) but there is no jump from the periodic attractor to the chaotic attractor. For a noise amplitude $\sigma_N \geq 0.05$, there are continuous jumps from chaotic attractor to the periodic attractor.

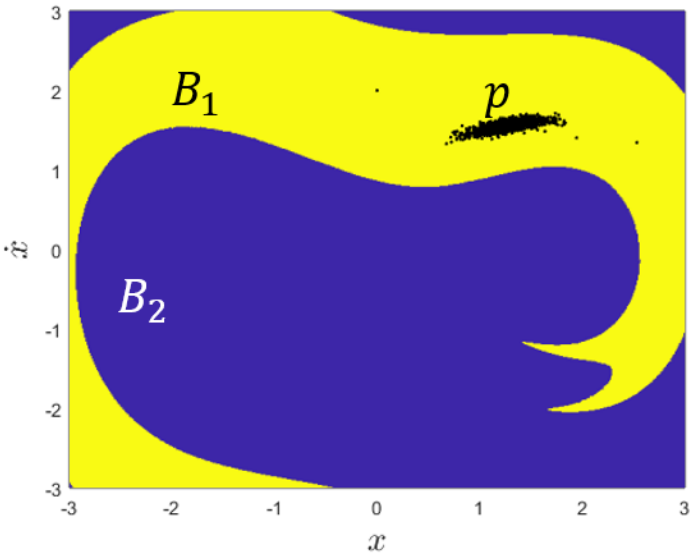

(a) Fixed point (periodic) attractor in yellow with noise

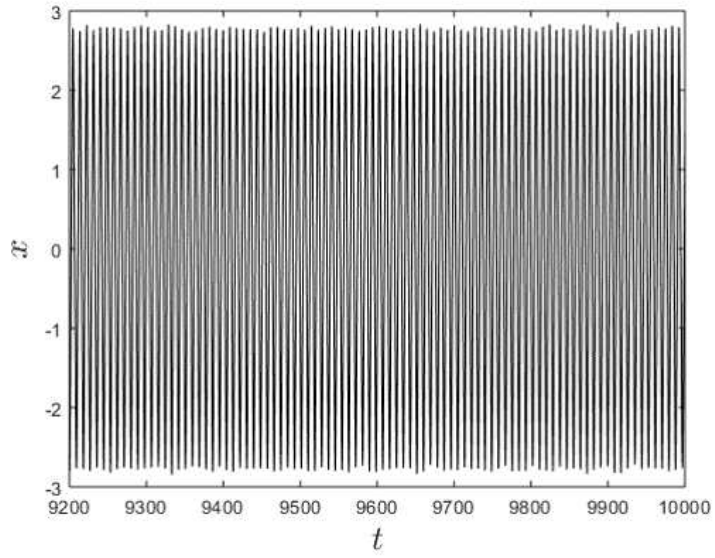

(b) Time series for an initial condition in yellow with noise

Figure 2.26: Numerical simulations using Euler-Maruyama scheme for noise amplitude $\sigma_N = 0.02$. See Table 2.7 for system parameter values. Purple color (B_2) and yellow color (B_1) are used to identify the basins of attraction of the chaotic and periodic attractors, respectively. In plot (a), the black dots in the yellow region are the (stroboscopic) periodic attractor with noise for an initial condition in the yellow region and plot (b) shows the associated time series. The periodic attractor (in yellow) exhibits no qualitative changes with the noise amplitude $\sigma_N = 0.02$.

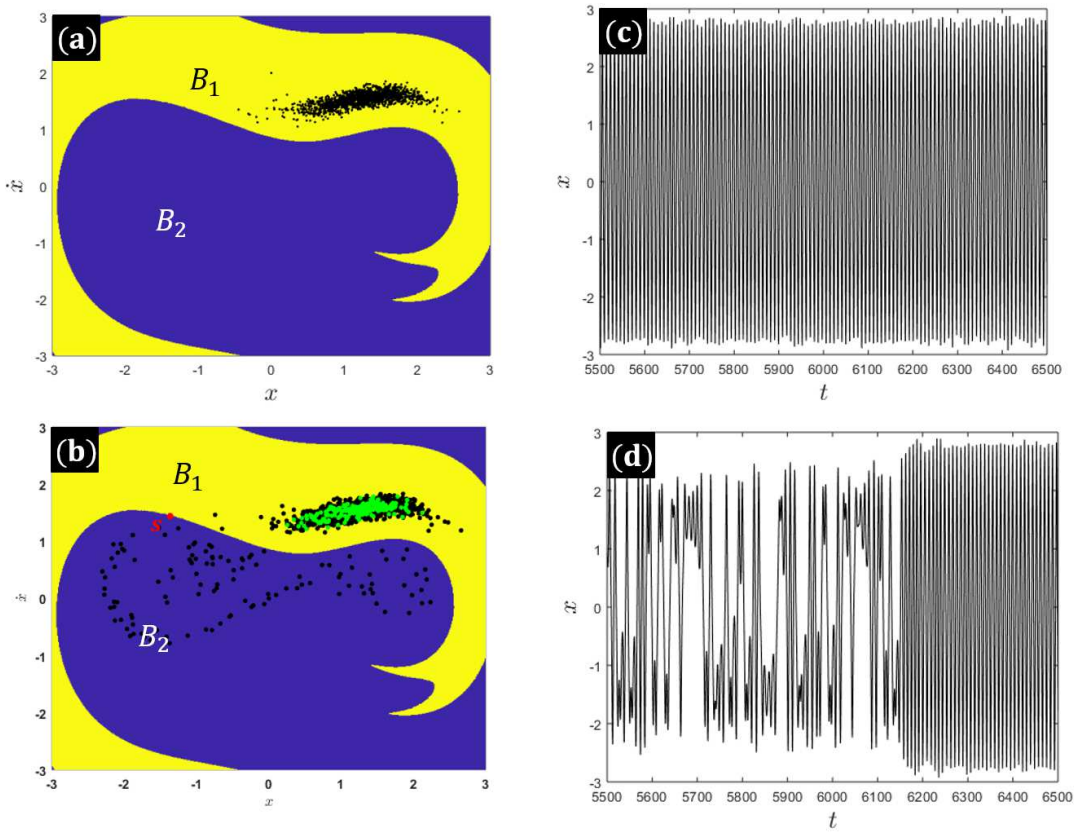

Figure 2.27: Numerical simulations using Euler-Maruyama scheme for noise amplitude $\sigma_N = 0.045$. See Table 2.7 for system parameter values. Purple color (B_2) and yellow color (B_1) are used to identify the basins of attraction of the chaotic and periodic attractors, respectively. In plot (a), the black dots in the yellow region are the (stroboscopic) periodic attractor with noise for an initial condition in the yellow region and in plot (b), the black and green dots are the stroboscopic map with noise for an initial condition in the purple region. The green dots represent the stroboscopic map with noise for the last 200 time periods. In plot (c), a part of the associated time series with noise for an initial condition in yellow region is shown. In plot (d), a part of the associated time series with noise for an initial condition in the purple region is shown. The chaotic attractor escapes to the fixed point (periodic) attractor but, periodic attractor (in yellow) exhibits no qualitative changes with the noise amplitude $\sigma_N = 0.045$.

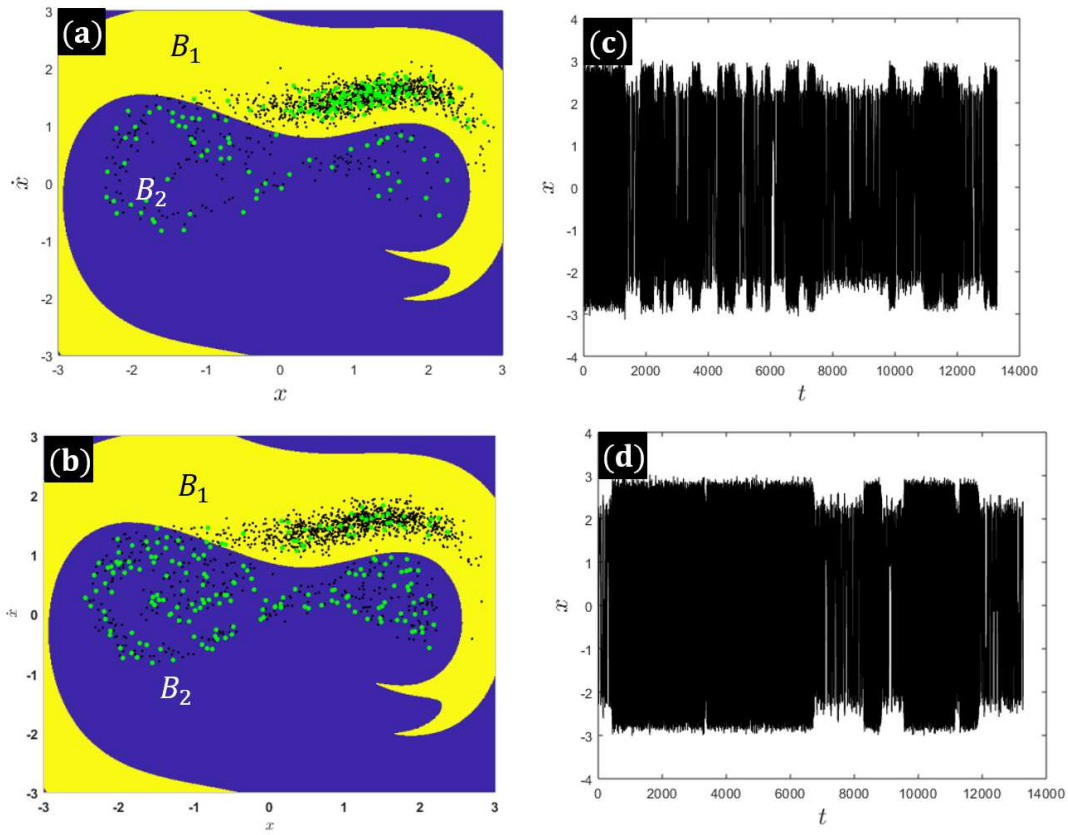

Figure 2.28: Numerical simulations using Euler-Maruyama scheme for large noise amplitude ($\sigma_N = 0.05$). See Table 2.7 for system parameter values. Purple color (B_2) and yellow color (B_1) are used to identify the basins of attraction of the chaotic and periodic attractors, respectively. In plot (a), the black dots in the yellow region are the (stroboscopic) periodic attractor with noise for an initial condition in the yellow region and in plot (b), the black and green dots are the stroboscopic map with noise for an initial condition in the purple region. The green dots in plot (a) and (b) represent the stroboscopic map with noise for the last 200 time periods. In plot (c), a part of the associated time series with noise for an initial condition in yellow region is shown. In plot (d), a part of the associated time series with noise for an initial condition in the purple region is shown. A continuous jump can be seen from the chaotic attractor to the periodic attractor and periodic attractor to chaotic attractor with the noise amplitude $\sigma_N = 0.05$.

The features of this saddle point can be seen at the critical collapse of the chaotic attractor at the critical event, the trajectory moves rapidly towards the saddle along the stable manifold of the saddle and then escapes along its unstable manifold towards the fixed point (periodic) attractor.

The numerical path integration procedure (Yu and Lin, 2004; Hanggi and Riseborough, 1983) based on the Gauss-Legendre integration rule has been used to find out the critical noise amplitude limit σ_c, for which there is a jump from chaotic attractor to the periodic attractor occurs. This procedure is based on the evolution of probability density subjected to a harmonic and a white Gaussian excitation where the periodicity of the probability density function implies a steady state response. For the given parameter values in Table 2.7, the critical noise amplitude is found to be $\sigma_c = 0.02$. The corresponding contour plot is shown in Figure 2.25(a).

With an initial condition in the chaotic attractor basin, with noise amplitude $\sigma_N = 0.02$, all Euler-Maruyama simulations show an escape from the chaotic attractor to the periodic attractor. The steady-state trajectory stays on the noisy periodic attractor thereafter. On the other hand, for all the initial conditions in the periodic attractor basin (yellow), the trajectory remains on the noisy periodic attractor without any qualitative changes or escape. The stroboscopic map along with the time series are shown in Figure 2.26.

Large noise amplitude. Further, the noise amplitude is increased in the simulation of equations (2.17). For an intermediate noise amplitude $\sigma_c \leq \sigma_N \leq \sigma_0$, the chaotic attractor is destroyed and the trajectory escapes to the fixed point (periodic) attractor. On the other hand, the periodic attractor shows no qualitative

changes. Here, the noise amplitude σ_0 represents the noise limit where the jump from the periodic attractor to the chaotic attractor occurs. Again, the numerical path integration procedure has been used to find out the noise amplitude limit σ_0. The corresponding contour plot is shown in Figure 2.25(c), wherein the noise amplitude limit is found to be $\sigma_0 = 0.05$. The time series results along with stroboscopic maps for the intermediate noise amplitude $\sigma_N = 0.045 \leq \sigma_0$ are shown in Figure 2.27. The associated contour plot is shown in Figure **??**(b). Additionally, for a large noise amplitude $\sigma_N \geq \sigma_0$, a continuous jump from a chaotic attractor to a periodic attractor and a periodic attractor to a chaotic attractor occurs. The contour plot for a noise amplitude $\sigma = \sigma_0 = 0.05$ is shown in Figure 2.25(c). The time series results and stroboscopic maps are shown in Figure 2.28 these results confirm the continuous jumps.

A comparison of numerical results with experimental findings is made in Section 2.6. It should be noted that there is no direct comparison between the noise amplitude in the numerical simulations, σ_N, and the noise amplitude in the experiments, σ_E. The noise in numerical simulations are assumed to be white Gaussian noise, while the noise in the experiment is a complicated function of several frequency-response relationships with almost a flat power density spectrum over the range of frequencies that are relevant to the context.

2.5.2 Experimental Results

Getting chaos in experimental system. The experimental studies have

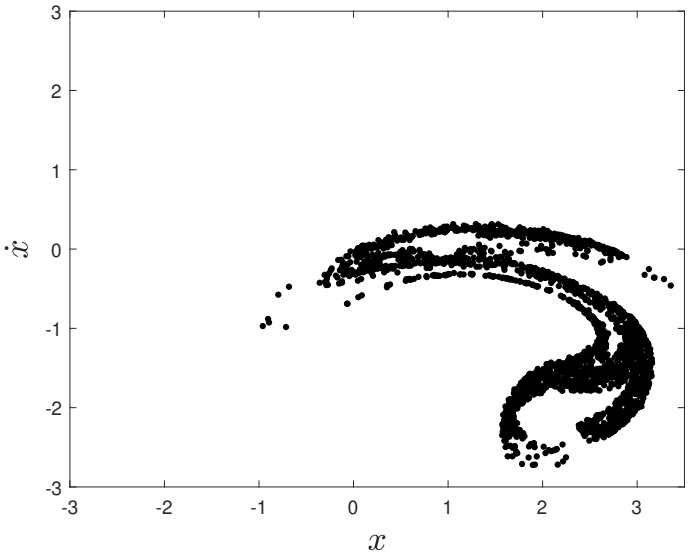

(a) Stroboscopic Map for $\sigma_E = 0$

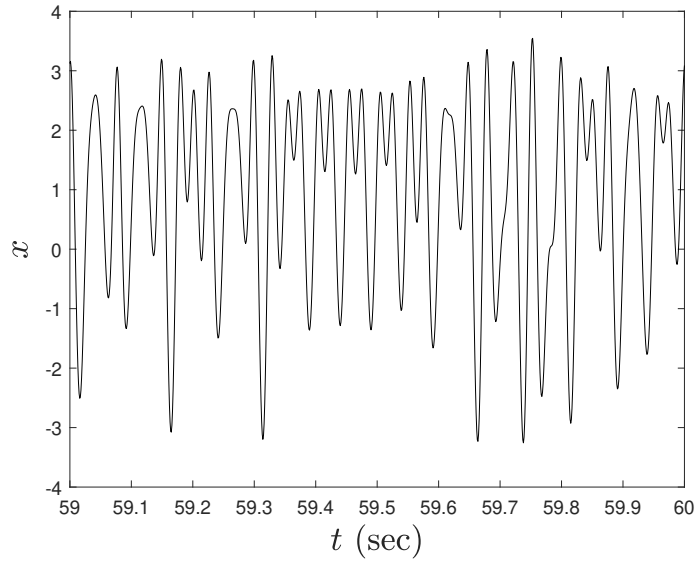

(b) Time Series for $\sigma_E = 0$

Figure 2.29: Stroboscopic map along with the time series obtained through experimental study of a forced bistable, softening Duffing oscillator showing chaotic attractor.

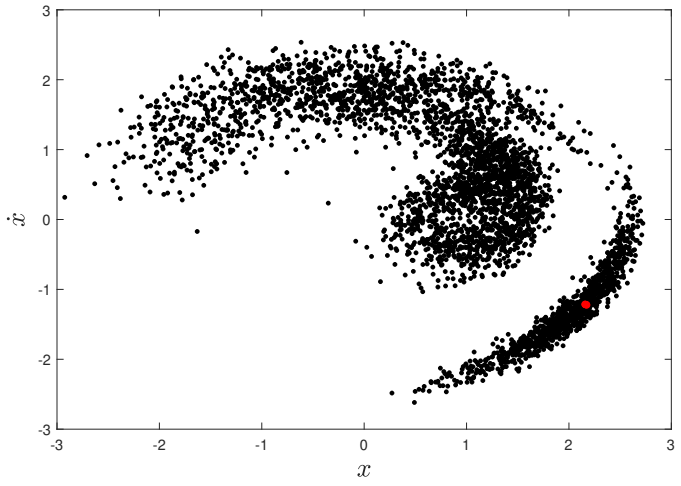

(a) Stroboscopic Map for Noise $\sigma_E = 2.0$

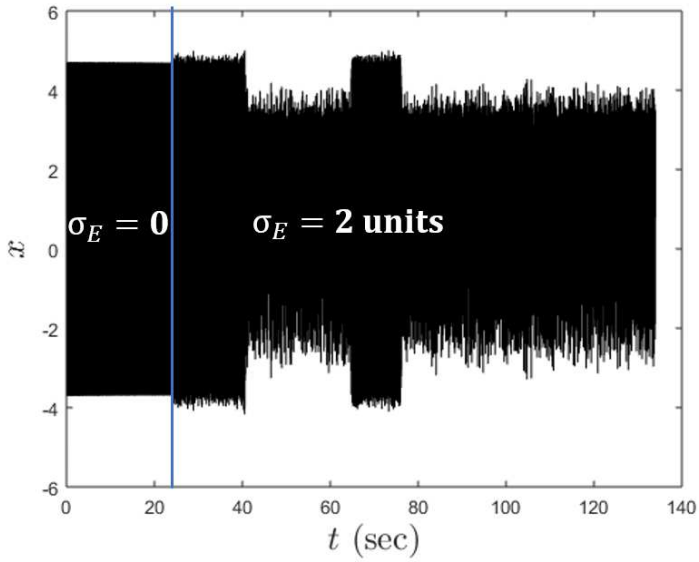

(b) Time Series for Noise Amplitude $\sigma_E = 2.0$

Figure 2.30: Stroboscopic map along with the time series obtained through experimental study of a forced bistable, softening Duffing oscillator for noise amplitude $\sigma_E = 2.0$. In plot (a), the black dots are the stroboscopic map with noise and the red dot is the fixed point attractor for the deterministic case. In plot (b), the associated time series with noise is shown. The system dynamics shows continuous jumps from chaotic attractor to periodic attractor and periodic attractor to chaotic attractor.

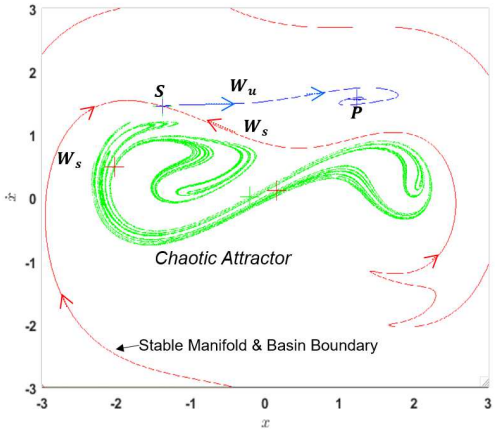

(a) Deterministic System

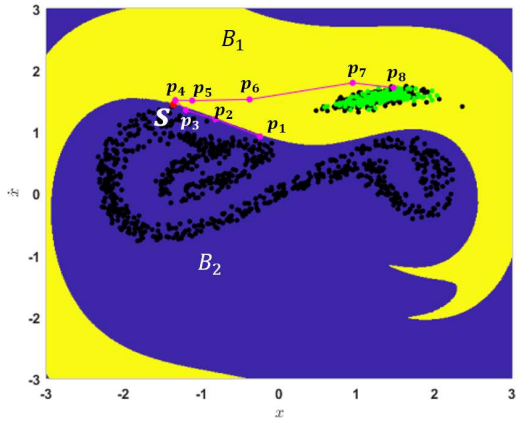

(b) Numerical Results: Noise-Induced Chaotic-Attractor Escape Route

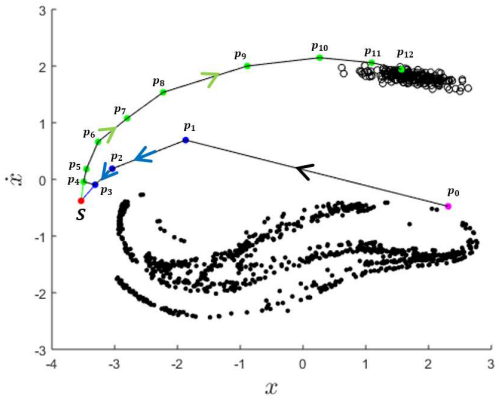

(c) Experimental Results: Noise-Induced Chaotic-Attractor Escape Route

Figure 2.31: The chaotic attractor is destroyed by noise and the trajectory escapes. In plot (a), the (stroboscopic) chaotic attractor (green color) along with stable (W_s) and unstable (W_u) manifold of the fixed point saddle (point "S") for the deterministic system are shown and point "P" is a fixed point attractor. In plot (b), the numerical results for the chaotic attractor escape route (through points p_1 to p_8) with noise $\sigma_N = 0.02$ are shown. The green dots represent the stroboscopic map for the last 200 time periods. For plot (c), a stroboscopic map is obtained through an experimental study of a forced bistable, softening Duffing oscillator with noise amplitude $\sigma_E = 1.8$. The start of the strobe for the experiments is arbitrary and is not synchronized with the clock used for plots (a) and (b). The chaotic attractor is destroyed by noise and the trajectory escapes. The chaotic attractor escape route (through points p_1 to p_{12}) with noise $\sigma_E = 1.8$ is shown. The black circles represent the stroboscopic map for the last 200 time periods. In both plots (b) and (c), the trajectory moves rapidly towards the saddle (point "S") along the stable manifold (basin boundary) of the saddle and then escapes along its unstable manifold towards the fixed point (periodic) attractor. See Figure 2.32 for the time series plot. See Section 2.6 for similarities and differences between numerical and experimental system.

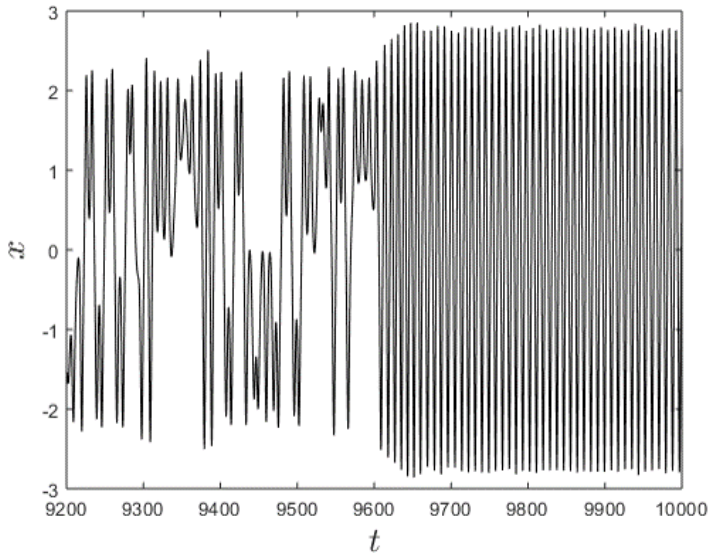

(a) Numerical Time Series for Attractor Escape with Noise

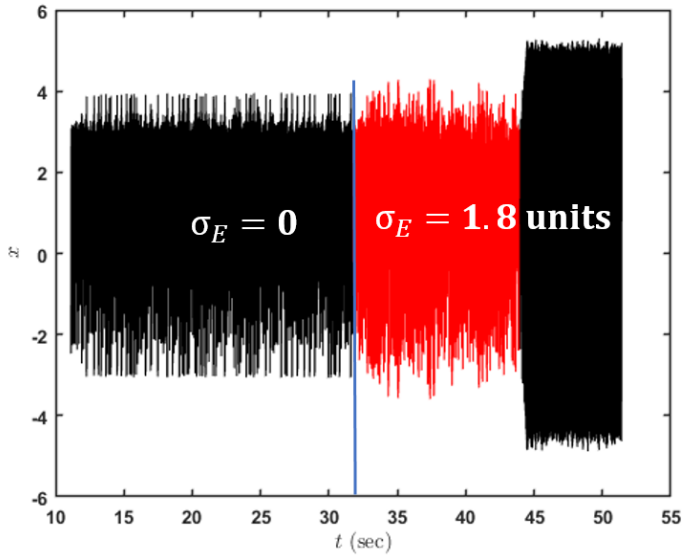

(b) Experimental Time Series for Attractor Escape with Noise

Figure 2.32: The chaotic attractor is destroyed by noise and the trajectory escapes. In plot (a), numerical time series plot is shown. In plot (b), the experimental time series plot is shown. Red color is used in the time window when noise is introduced. The time series shows that the chaotic attractor escape to the periodic attractor (fixed point). See Figure 2.31 for the stroboscopic map. See Section 2.6 for similarities and differences between numerical and experimental results.

been conducted with a forced bistable, Duffing oscillator prototype with softening characteristic. The deterministic response shows chaotic behavior. After parametric identification through curve fitting the experimentally obtained frequency-response curve to analytically obtained response curve, the numerically obtained bifurcation diagram helps to identify the forcing amplitude F_0 and forcing frequency Ω in the chaotic region. For this study, the author has chosen $F_0 = 0.204$ and $\Omega = 0.71$. from the experimental studies for these parameter values (Table 2.7), one can note chaotic dynamics. Both, the time series and the stroboscopic map are shown in Figure 2.29.

The numerical results are obtained by assuming noise to be a white Gaussian noise whereas, in the experimental studies, the noise is assumed to be a band-limited white noise. Due to a constant power density spectrum in the operating forcing frequency range of interest, the band limited white noise may be treated as being equivalent to a white Gaussian noise. In this section, the experimental results are qualitatively compared with numerical outcomes. For any noise amplitude σ_E, the experiments are conducted for more than 15 runs and around 5000 time periods in each run.

Escaping chaos. A small noise amplitude σ_E does not result in an observable qualitative change and the response is a noisy chaos. However, a further increase in the noise amplitude σ_E, results in an eventual but sudden change in the qualitative behavior and the response escapes from the chaotic basin. Here, the noise level is just sufficient to cause the chaotic trajectory to escape to the periodic attractor within a mean time of 100 oscillation of the forced Duffing oscillator. Similar to the

numerical results, the author observes that there is a specific escape route that the trajectory always follows - the escape trajectory is essentially on the basin boundary. The dynamics pulls the trajectory toward the fixed point on the basin boundary and subsequently, the trajectory escapes along the unstable manifold of the saddle point; that is, the branch of the unstable manifold outside the chaotic basin. The steady state trajectory stays on the noisy periodic attractor thereafter.

Repetitions of this experiment show that when the trajectory escapes, it always escapes the basin in the same way. One of the experimental results are shown in Figure 2.31(c). The experimental findings are in agreement with the numerical results shown in Figure 2.31(b).

Large noise amplitude. For large noise amplitude, it does not necessarily follow the above route. Hence, it is essential to keep the noise level as low as possible to observe the exit route. Similar to the numerical results shown in Figure 2.28, a large noise amplitude quickly leads to continuous jumps from chaotic attractor to periodic attractor and back to the chaotic attractor, repeatedly as shown in Figure 2.30. The stroboscopic map shows a cloud of points on the chaotic and periodic attractor with continuous jumps. It should be noted that a particular range of amplitude of noise σ_E is needed to control and terminate the chaotic response and move the response towards a stable periodic attractor.

2.6 Conclusions

In this chapter, the author has examined the effects of a white Gaussian noise on the chaotic and periodic responses of a harmonically forced monostable and bistable, Duffing oscillator with softening characteristics. Numerical simulation results have been obtained for more than 100 Euler-Maruyama simulations in the time domain over 1000 time periods and the experimental results are obtained for more than 15 experimental runs with 5000 time periods for each run.

Through the numerical and experimental studies, it is shown that with the addition of white Gaussian noise, the jump-up and jump-down frequencies in the frequency-response can be moved towards each other and the region of hysteresis can be reduced. In particular, a low level of noise can reduce the hysteresis region. With an appropriate increment in noise amplitude, it is found that the hysteresis region can also be completely destroyed. These findings suggest that the effect of nonlinearity on the frequency-response of a softening Duffing oscillator can be countered through the addition of white Gaussian noise.

For a monostable, Duffing oscillator with softening characteristics, it is found that there is a limitation on the level of maximum noise amplitude one can impose on the system. Through both experiments and simulations, it is found that beyond a certain noise level, the response of the system is moved into the unstable region. On the other hand, for a bistable, Duffing oscillator with softening characteristics, for a large level of noise amplitude, the frequency-response curve looks like a cluster of points. In this case, through experiments and simulations, it is found that, beyond a

certain noise level, the system response is moved from one potential well to another potential well.

Similarities and differences between numerical and experimental systems. 1) The systems here are observed stroboscopically. The appearance of an experimental plot depends strongly on the phase of the strobe that is upon the instant the strobe is started. Hence, much of the difference between the numerical and experimental chaotic attractor is due to the difference in the phase of observation. 2) The parameter range for observing chaos coexisting with a periodic attractor is in a similar range for the two systems. 3) The boundary saddle S is shifted but the basin boundary in both systems is dominated by a fixed point saddle and its stable manifold. 4) There is no direct comparison between the noise amplitude in the numerical simulations, σ_N, and the noise amplitude in the experiments, σ_E. The noise in numerical simulations are assumed to be white Gaussian noise, while the noise in the experiments is a complicated function of several frequency-response relationships with almost a flat power density spectrum over the range of frequencies that are relevant to the context. 5) For both studies, with the addition of noise, as the amplitude reaches a critical value, there is a change. A typical attractor in the chaotic regime quickly escapes to the periodic attractor. This departure is always via a special escape route: the unstable manifold of a saddle point on the basin boundary between the two basins of attraction.

While the author's study here concerns a specific system with specific parameters, it is believed that the observed phenomena is quite general and the escape route would be observed in a wide variety of nonlinear systems. These findings also

suggest that a range of noise amplitude can be used to control the chaotic dynamics without any change in system parameter values.

Chapter 3: Safe Regions with Partial Control of a Chaotic System in the Presence of Noise

Under the influence of noise, it has been shown that the response of many discrete-time dynamical systems can be moved away from a particular region. In this chapter, the partial control scheme constructed for a chaotic system is applied for confining the trajectories inside a particular region despite the presence of white noise as reported in the work of Agarwal *et al.* (2017) and Agarwal and Balachandran (2019a). The proposed algorithm is independent of the dimension of the system. As an illustration, the partial control method has been applied to restrict the response of a Duffing oscillator to a certain state-space region. Different noise forms are considered and numerical results are presented to illustrate the effectiveness of this control method.

The rest of this chapter is organized as follows. In Section 3.1, the author describes the concept of a safe set, the sculpting algorithm for computing a safe set, and the partial control method for a system with white noise by using the Euler-Maruyama integration method. In Section 3.2, an application of this method to the response of a Duffing oscillator is considered. In particular, parameters for which this system experiences a transient chaotic behavior are considered. In Section 3.3,

comparisons are made between the cases with white noise and bounded noise. In this chapter, "bounded" noise or disturbance refers to a disturbance with finite upper bound. Finally, conclusions are drawn together and presented in Section 3.4.

3.1 Partial Control in the Presence of White Noise

3.1.1 Escaping Trajectories

Let f be a continuous map of phase space; then, one can write as

$$q_{n+1} = f(q_n), \tag{3.1}$$

where the trajectory at the n^{th} step is mapped to the $(n+1)^{th}$ step. In nonlinear systems, for a given choice of parameters, the trajectories may exhibit chaotic behavior for a while before eventually leaving that particular region or reaching a stable periodic state. As previously mentioned, this behavior is referred to as "transient chaotic" behavior, and the topological structure inside region Q associated with transient chaotic behavior is a zero-measure set known as a chaotic saddle (Tél and Gruiz, 2006; Alligood *et al.*, 1997).

In various practical applications, due to external disturbances, trajectories typically rapidly leave the region of the state space where transient chaos occurs. To model this, the author considers that there is a white noise component $\sigma\dot{W}(t)$ that causes the trajectory q_n to leave the region Q, where by leaving a region, the author means that the trajectory is leaving that particular region Q, or it converges

towards a fixed point or an attractor that one does not consider as being a part of that particular region Q. In equation form, the relevant map can be written as

$$q_{n+1} = f(q_n, \xi_n). \tag{3.2}$$

Here, q_n is the state at step n, f is a function with chaotic transient in Q, ξ_n is the noise input. The noise input to the system is represented by $\sigma\dot{W}(t)$, where σ represents noise amplitude, $W(t)$ represents the Wiener process and $\dot{W}(t)$ is the associated derivative of Brownian motion. The goal is to choose a control u_n such that for the partially controlled trajectories governed by

$$q_{n+1} = f(q_n, \xi_n) + u_n(r), \tag{3.3}$$

one can guarantee that the q_n remain in region Q for an appropriate choice of control $u_n(r)$ with an upper bound of $u_0(r)$. The author refers to $u_n(r)$ as feedback control that can be chosen with the knowledge of white noise component ξ_n and $f(q_n)$, or in particular $f(q_n, \xi_n)$. Therefore, the goal is to find an appropriate feedback control $u_n(r)$ which is a function of $f(q_n, \xi_n)$, and is bounded by $u_0(r)$. It is also worth noting that the applied control $u_n(r)$ is a discrete control input. To apply this control method to a continuous dynamical system, one has to consider a discretized state of the system. This is usually done by constructing a Poincaré section for autonomous systems, or a stroboscopic map for non-autonomous systems such as forced oscillators. For the current study, the author construct the stroboscopic map with a clocking time rT, where $r = 1, 2, 3, ...$ and T represents the time-period of the

applied harmonic force. With this discretization, the control input required by the partial control method $u_n(r)$ is only applied discretely at regular intervals of time (when stroboscopic maps are used) rT. At any other instant, the system is allowed to evolve freely, without any kind of control.

In the present work, the following assumptions are made:

1. The region Q is a closed and bounded region in the phase space.

2. The applied feedback control $u_n(r)$ in phase space has an upper bound $u_0(r)$, which means that it satisfies $|u_n(r)| \leq u_0(r)$. Such control $u_n(r)$ is called "admissible control". Here, only admissible control is considered.

3. The bound on the control $u_0(r)$ depends on the noise amplitude σ and r.

Here, a safe set S is defined as the set of points in a bounded region, satisfying the following:

1. A safe set S is a subset of Q; that is, $S \subset Q$.

2. For each point q_n in phase space S ($q_n \in S$), the distance of $f(q_n, \xi_n)$ from S is at most $u_0(r)$. This implies that there exists an admissible control value $u_n(r)$ which has an upper bound $u_0(r)$, such that $f(q_n, \xi_n) + u_n(r)$ is in S, or $f(q_n, \xi_n) + u_n(r) \in S$. A safe set is decided by the white noise amplitude σ and control bound $u_0(r)$.

By applying admissible control, it is possible to keep the entire trajectory q_n of equation (3.3) in S and hence in Q. Then, if q is in a safe set $S \subset Q$, the trajectories

can be controlled to stay in S and consequently in Q by choosing the control $u_n(r)$ so that q_{n+1} is in S. For a bounded disturbance, wherein the disturbance ξ_n is bounded by ξ_0, the trajectories are allowed to be remain inside a region Q even when the upper bound of the control u_0 is smaller than the upper bound of the disturbance ξ_0 (Sabuco *et al.*, 2012a). In prior work, safe sets have only been found for one-dimensional and two-dimensional maps for bounded noise values of $\xi_n \leq \xi_0$ (Sabuco *et al.*, 2012a) and the control has been applied at each time interval of T.

In the current study, while applying the partial control method, a grid of points is used for the close bounded region Q that needs to be controlled, and the largest safe set S is found. The control has been applied at the discrete (integer multiple) time steps of rT.

3.1.2 Form of Safe Set

Over the last few years, researchers have considered cases with bounded noise and found safe sets for these cases (Sabuco *et al.*, 2012a). The algorithm for finding a safe set for a bounded noise is available, and it is known that the shape of a safe set can be geometrically more complicated than expected (Sabuco *et al.*, 2012a).

In the present work, the author has followed the steps used by Sabuco *et al.* (2012a). However, the author has had to change the numerical integration scheme, since the white Gaussian noise has been considered instead of bounded noise.

In the prior section, the important properties of a point belonging to a safe set has been mentioned. These properties will be used to develop the algorithm to

compute safe sets by using a recursive algorithm. The algorithm is based on the Euler-Maruyama integration scheme and it can be used to find a safe set whenever there is a chaotic saddle in the region Q. The algorithm has been demonstrated with a Duffing oscillator that exhibits the Wada property, which arises in the phase space for all the basins of attraction. Due to this property, every point on the boundary of any basin is also on the boundary of the other two basins. There also exist fixed points and periodic attractors inside the region Q, and almost all trajectories eventually are attracted to one of the fixed points or periodic attractors, as it is expected for cases with transient chaos.

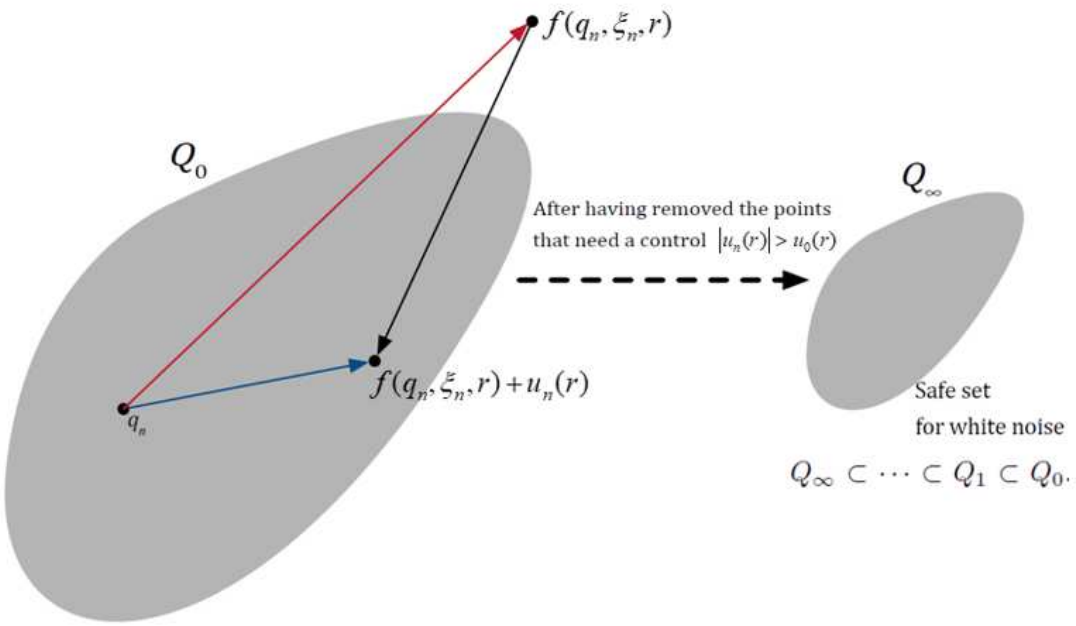

Figure 3.1: Partial Control of a system showing chaotic transient behavior under the influence of white noise: The red arrow shows the mapping of a point q, under the application of a harmonic force and white noise $\xi_n = \sigma\dot{W}(t)$ with noise amplitude σ. The blue arrow shows the mapping of point q, once the control $u_n(r)$ is applied to keep the the point in region Q_0. The control parameter $u_n(r)$ is bounded by an upper bound value of $u_0(r)$. This method removes all the points which need a control $u_n(r) > u_0(r)$. The removed points are called "unsafe" points. Once the "unsafe" points are removed, a new region $Q_1 \subset Q_0$ is obtained. This process is iterated until there is convergence to a safe set Q_∞, which satisfies: $Q_\infty \subset \cdots \subset Q_1 \subset Q_0$.

3.1.3 Sculpting Algorithm for Computing Largest Set

Consider a closed bounded region Q represented by a set of grid points that has to be controlled. Again, the trajectory of any point q in Q without any disturbance is given by

$$q_{n+1} = f(q_n). \tag{3.4}$$

The trajectories are associated with transient chaotic behavior. The application of a white gaussian noise $\sigma\dot{W}(t)$ is represented as

$$q_{n+1} = f(q_n, \xi_n). \tag{3.5}$$

Given the closed bounded set Q and upper bound of control $u_0(r)$, it is declared that a point q in Q is "unsafe" (for Q) under the influence of white noise $\sigma\dot{W}(t)$, if the distance of $f(q_n, \xi_n)$ from region Q is more than the upper bound of the control $u_0(r)$, and such $f(q_n, \xi_n)$ has no admissible control u for which $f(q_n, \xi_n) + u$ is in Q. Then, the sculpting operation Υ that results in the removal of the unsafe points from Q has been defined. This implies that $\Upsilon(Q)$ is the set of safe points in Q after removal of the unsafe points.

The numerical simulation is started with consideration of a grid of points in a close bounded region Q where one needs to find safe set. Then one lets $Q_0 = Q$ and applies the sculpting operator Υ. After removal of the unsafe points from Q_0, one gets $Q_1 = \Upsilon(Q_0)$, wherein Q_1 is the subset of Q_0. Similarly, one computes $Q_2 = \Upsilon(Q_1)$, which is a subset of Q_1 after removal of the unsafe points from Q_1.

In general, one iterates to compute a new set of points $Q_{n+1} = \Upsilon(Q_n)$ by removing the unsafe points from Q_n for each $n > 0$. These sets are all compact sets as f is continuous. The intermediate sets Q_n, are the set of points that can be kept without escapes in the region Q with the partial control method for at least n iterations. The iteration is carried out, until there is convergence to a safe set Q_∞, which satisfies $Q_\infty \subset \cdots \subset Q_1 \subset Q_0$. The set Q_∞, is the set of points that can be indefinitely kept without escapes from the region Q through application of the partial control method.

Now, for any point q ($q \in Q_\infty$), the distance of point $f(q, \xi_n)$ from region Q_∞ is less than the upper bound of the control u_0. In other words, no unsafe point exists within the region Q_∞. After the application of the admissible control u, one gets the point $f(q, \xi_n) + u$, which is inside Q_∞. The author represents Q_∞ as

$$Q_\infty = \bigcap_{n=1}^{\infty} Q_n. \tag{3.6}$$

Also, it is noted that any safe set S in Q is a subset of Q_n and consequently of Q_∞. Q_∞ represents the largest safe set in Q. With this notation, the author writes $\Upsilon(Q_{n+1})$ to be the set of points $q \in Q_n$ for which $f(q)$ is in $(Q_n + u_0(r)) - \xi_n$. Hence, one needs to compute the sets $(Q_n + u_0(r)) - \xi_n$ to find the final safe set.

With the discussed construction of the algorithm, one might need an infinite number of iterations to converge. This would be the general situation for a continuous state space, wherein the state space volume of the points removed at each iteration is infinitesimally small. For this reason, from a practical point of view,

the author recommends computation of the safe set by using a fine grid. With this approach, one only checks the "safety" of the points of the grid, thereby helping the algorithm converge to the safe set in a finite number of iterations. Following this reasoning, the algorithm either converges to the safe set in a number of iterations that is much smaller than the number of the grid points or it does not converge. In the latter case, the author assumes that no safe set exits in the region. The drawback of using this approach (finite grid), is that the actual bound of control used when controlling the real system is always going to be a little bit higher $u_0 + \Delta u$ than u_0, due to the finite resolution. However the deviation of the bound of control Δu from u_0 can be made arbitrarily small by using grids with fine resolution. As a rule of thumb, it is recommended that one uses grid resolutions 10 times smaller or more than the bound of control required Capeáns *et al.* (2016).

By using the Sculpting Algorithm, it has been possible to compute safe sets for a wide variety of systems. The necessary conditions to guarantee their existence is the presence in the region of interest of a Smale horseshoe (Zambrano *et al.*, 2008). However, this is difficult to achieve in most practical cases. For this reason, the author recommends for checking of the existence of safe sets in a particular region, by directly applying the algorithm and checking whether there is convergence or not.

3.1.4 Algorithm Implementation for Duffing Oscillator

The equation of motion of a Duffing Oscillator with mass m, viscous damping c, linear stiffness k_1, nonlinear stiffness k_3, forcing amplitude F_0, and forcing frequency ω can be written as

$$m\ddot{y} + c\dot{y} \pm k_1 y + k_3 y^3 = F_0 \sin(\omega t). \tag{3.7}$$

where '+' sign corresponds to a Duffing oscillator with a hardening stiffness characteristic, '−' sign corresponds to a Duffing oscillator with a softening characteristic, and an overdot represents differentiation with respect to time. The harmonic excitation or deterministic input is represented by $F \sin \omega t$. After substituting $x = \sqrt{\frac{k_3}{k_1}} y$ and $\tau = \omega_n t$ into equation (3.7), and simplifying, the resulting non-dimensional form of the Duffing equation reads as follows:

$$\ddot{x} + 2\zeta\dot{x} \pm \alpha x + \alpha x^3 = \gamma \sin(\Omega\tau). \tag{3.8}$$

Here, ω_n represents the natural frequency of the system, $\zeta = \frac{c}{2m\omega_n}$, $\alpha = \frac{k_1}{m\omega_n^2}$, and $\gamma = \frac{F_0}{m\omega_n^2}\sqrt{\frac{k_3}{k_1}}$.

In addition equation (3.8) can be written in the state-space form as

$$\begin{cases} \dot{x_1} &= x_2 \\ \dot{x_2} &= -2\zeta x_2 \mp \alpha x_1 - \alpha x_1^3 + \gamma \sin(\Omega\tau), \end{cases} \tag{3.9}$$

where $x_1 = x$, and $x_2 = \dot{x}$.

The author considers $q = (x_1, x_2)^T$ and for the $(p+1)^{th}$ step, has

$$\begin{cases} x_1(p+1) = x_1(p) + x_2(p)dt \\ x_2(p+1) = x_2(p) + [-2\zeta x_2(p) \mp \alpha x_1(p) \\ \qquad -\alpha x_1^3(p) + \gamma \sin(\Omega\tau)]dt. \end{cases} \tag{3.10}$$

The above equation takes the form of equation (3.4). Here, $q_{p+1} = (x_1, x_2)^T_{p+1}$, and the right hand side of the equation represents $f(q_p)$ or $f(q_n)$.

After the introduction of the white noise into the Duffing oscillator, equation (3.8) is modified as

$$\ddot{x} + 2\zeta\dot{x} \pm \alpha x + \alpha x^3 = \gamma \sin(\Omega\tau) + \sigma\dot{W}(t). \tag{3.11}$$

By following the steps used to arrive at equation (3.10) in state-space form, the above equation can be written in the Langevin form of a differential equation; that is,

$$\begin{cases} x_1(p+1) = x_1(p) + x_2(p)dt \\ x_2(p+1) = x_2(p) + [-2\zeta x_2(p) \mp \alpha x_1(p) \\ \qquad -\alpha x_1^3(p) + \gamma \sin(\Omega\tau) + \sigma\dot{W}(t)]dt. \end{cases} \tag{3.12}$$

Here, σ represents the noise amplitude, and $\dot{W}(t)$ is a "mnemonic" derivative. The

above equation can be simplified to

$$\begin{cases} x_1(p+1) = x_1(p) + x_2(p)dt \\ x_2(p+1) = x_2(p) + [-2\zeta x_2(p) \mp \alpha x_1(p) \\ \quad -\alpha x_1^3(p) + \gamma \sin(\Omega\tau)]dt + \sigma dW. \end{cases} \tag{3.13}$$

It is mentioned that in this differential form, one no longer has the derivative of the Brownian motion (which does not exist) but a differential white noise which does exist. Now, the Euler-Maruyama method can be used to obtain numerical solutions of equation (3.13). In this form, p is associated with the time step in the solver. The quantity dW, is the incremental noise, which has a mean that is equal to zero and a standard deviation that is equal to $\sqrt{dt}$.

The system represented by equation (3.13) can be written compactly as

$$q_{p+1} = f(q_p, \sigma dW), \tag{3.14}$$

where q_{p+1} is also dependent on the noise input. The author calls q_{p+1} as the the image point of q_p with noise after time step dt.

The author calls q_{n+1} the image point of q_n after a time rT, as shown in Figure 3.2. Alternatively, the equation can be written as

$$q_{n+1} = f(q_n, \xi_n), \tag{3.15}$$

where ξ_n represents the input noise vector.

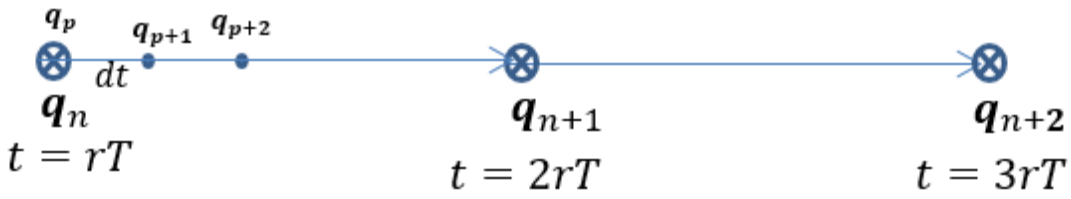

Figure 3.2: Integration and control steps. The simulation has been done considering a step size of dt, which maps q_p to q_{p+1}. q_{n+1} is the image point of q_n after a time which is an integer multiple of time period of harmonic force. ξ_n represents the noise vector applied. The control $u_n(r)$ is applied at each time step of rT. Here, $T = 2\pi/\Omega$ and $r = 1, 2, 3, ...$

For the application of a bounded control, the above equation can be extended as

$$q_{n+1} = f(q_n, \xi_n) + u_n(r). \tag{3.16}$$

Here, the control $u_n(r)$ is a bounded control, which means $|u_n(r)| \leq u_0(r)$.

In the presence of white noise, the steps involved in implementing the partial control algorithm for a continuous time system, such as a Duffing oscillator, are as follows:

1. Start by selecting a grid of points in region Q_0 where the trajectories exhibit a transient chaotic behavior. Introduce white noise as $\sigma\dot{W}(t)$ and for each point q_n in region Q_0 ($q \in Q_0$), and estimate the image point q_{n+1} by using the Euler-Maruyama Scheme.

2. Based on the value noise vector, for each grid point, compute the maximum distance between the image point with noise and the image point without noise. The maximum distance between them represents the upper bound of

the disturbance to apply the Sculpting Algorithm. Based on values of q_n, noise vector, and the function f, choose the upper bound of the control u_0. If one chooses upper bound u_0 to be too small, the resulting safe set would be an empty set, and if the trajectory without control (equation (3.14)) is inside the region Q_n, $u_n = 0$; otherwise, one needs to apply a non-zero control u_n.

3. The goal is to maintain the trajectory inside a region Q_0. To accomplish this, verify whether the point is a safe point or not. Calculate $q_{n+1} = f(q_n, \xi_n) + u_n$ under the application of noise and control, and keep q_{n+1} inside the safe set. If all of the points after the application of a control u_n, which satisfies $|u_n| \leq u_0$, are inside the region Q_n, the set is a safe set. Otherwise, one needs to remove the unsafe points which are points that need a control $u_n > u_0$ from Q_n.

4. After removal of all of the unsafe points from Q_n which do not satisfy the control criteria, iterate to get to the next set of region Q_{n+1}, which is a subset of Q_n. Again, check the conditions on the iterated points, whether they are safe or not as mentioned in step 3. Repeat this process until one gets the final safe set, where $Q_n = Q_{n+1}$. Represent the safe set as Q_∞.

The results obtained for the Duffing oscillator are presented in the next section.

3.2 Results: Application of Partial Control Method to Duffing Oscillator

To demonstrate the algorithm, the author uses the Duffing oscillator parameters used previously by Sabuco *et al.* (2012a); that is,

$$\ddot{x} + 0.15\dot{x} - x + x^3 = 0.245\sin(t). \tag{3.17}$$

For this particular choice of parameters used in equation (3.17), the Duffing oscillator experiences a transient chaotic behavior; the trajectories exhibit chaotic characteristics for a finite amount of time in a compact region Q, until they move to a final state. Depending on the initial conditions, the final state can be a fixed point, or a periodic attractor, or a region outside the bounded region Q. For the particular parameters considered, depending on the stroboscopic map clocking time (rT), the system as given by equation (3.17) has either three attractors including two fixed points and one period 3 orbit or five fixed points. The basin of attraction for different stroboscopic maps are shown in Figure 3.3 and approximate locations of the fixed points are shown in Table 3.1.

With these parameters values, the Duffing oscillator given by equation (3.17) possesses a very interesting property called the Wada property (Aguirre and Sanjuán, 2002); that is, every point on the boundary of any basin shares the boundary of the other two basins.

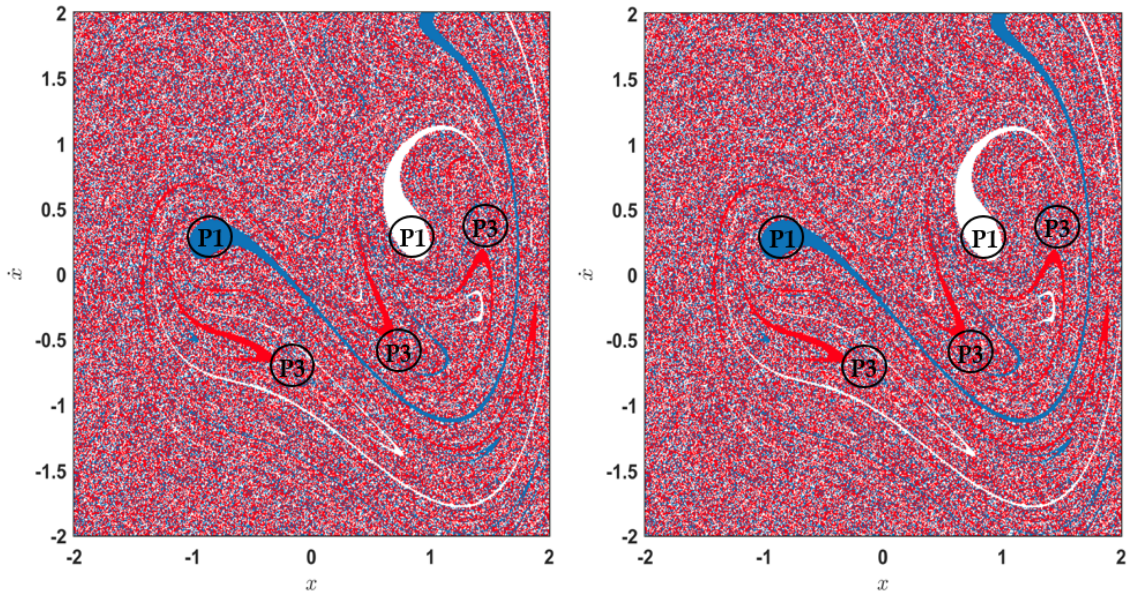

(a) Clocking time: $(3k+1)T; k = 0, 1, 2, ...$

(b) Clocking time: $(3k+2)T; k = 0, 1, 2, ...$

(c) Clocking time: $3(k+1)T; k = 0, 1, 2, ...$

Figure 3.3: Basin of attraction with different clocking time for the Duffing oscillator given in equation (3.17). In this system, in general there are three different clocking time are present. T represents the forcing time period which is $T = 2\pi/\Omega = 1$. Different colors represents different attractors. $P1$ represents fixed points (period-1 attractor) and $P3$ represents period-3 attractor. The approximate locations are shown in Table 3.1.

Table 3.1: Attractors for the Duffing oscillator given in equation (3.17)

Attractor	**Clocking time:** $(3k+1)T; k = 0, 1, 2, ...$
Period-1 Attractor ($P1$)	$(0.815, 0.242)$; $(-0.933, 0.299)$
Period-3 Attractor ($P3$)	$(-1.412, -0.137)$; $(-0.354, -0.614)$; $(0.645, -0.464)$
Attractor	**Clocking time:** $(3k+2)T; k = 0, 1, 2, ...$
Period-1 Attractor ($P1$)	$(0.815, 0.242)$; $(-0.933, 0.299)$
Period-3 Attractor ($P3$)	$(-1.412, -0.137)$; $(-0.354, -0.614)$; $(0.645, -0.464)$
Attractor	**Clocking time:** $3(k+1)T; k = 0, 1, 2, ...$
Period-1 Attractor ($P1$)	$(0.815, 0.242)$; $(-0.933, 0.299)$; $(-1.412, -0.137)$; $(-0.354, -0.614)$; $(0.645, -0.464)$
Period-3 Attractor ($P3$)	No period-3 attractor

As mentioned in the previous section, the application of the partial control algorithm to the Duffing oscillator here differs from the previous applications (Sabuco *et al.*, 2012a), due to the form of the noise. For the present case, let $q = (x, \dot{x})^T$, and let $f(q)$ be the stroboscopic time map of the nonautonomous oscillator given by equation (3.17). Here, a square $[-2, 2] \times [-2, 2]$ has been chosen as the region of interest Q, where the unperturbed and uncontrolled Duffing oscillator is given by equation (3.17). This system exhibits a transient chaotic behavior and the goal is to maintain the trajectory inside the region Q and away from the attracting fixed points and attracting periodic orbit of period 3. Depending on the initial conditions, the final state of the unperturbed and uncontrolled system (equation (3.17)) can be a fixed point, a periodic attractor, or a region outside the bounded region Q. With the goal of maintaining trajectories far away from these attractors, the partial control technique has been applied by taking into consideration the forcing amplitude and disturbance ξ_n that depends on the noise value $\sigma\dot{W}(t)$. Given the clocking time

rT, the applied control $u_n(r)$ is bounded by the maximum control value $u_0(r)$.

As an illustrative example, the author has used a grid of 3000×3000 points in the square $[-2, 2] \times [-2, 2]$ and computed the safe set for the noise amplitude value $\sigma = 0.002$ and the control is applied at discrete time intervals. The upper bound of the control $u_0(r)$ depends on the clocking time. The author started with all of the grid points and removed a circle of radius 0.2 units around each attractor orbit ($P1$ and $P3$) to prevent the periodic behavior. In order to compute the noise bound, for each grid point, the distance between image point with noise and image point without noise has been computed . The iterations have been done for 100 different noise vectors and the maximum distance has been picked up as representing the noise bound. The region with few points that have a large maximum disturbance (more than 0.1) and also, need a large control; that is, $u > 0.1$, has been removed. The remaining region has been considered as the initial set where the Sculpting Algorithm has been applied. Then, the author has implemented the previously described Sculpting Algorithm to remove the "unsafe" points and keep the "safe" points after each iteration, until there is final convergence to a safe set. For this specific choice of σ and u_0, it took 9 iterations of Sculpting Algorithm Υ to obtain the safe set. After each iteration, the number of grid points inside the region Q_n has been computed . Finally, when the number of points in sets Q_n and Q_{n+1} are the same ($Q_{n+1} = Q_n$), the Sculpting Algorithm iteration process is stopped.

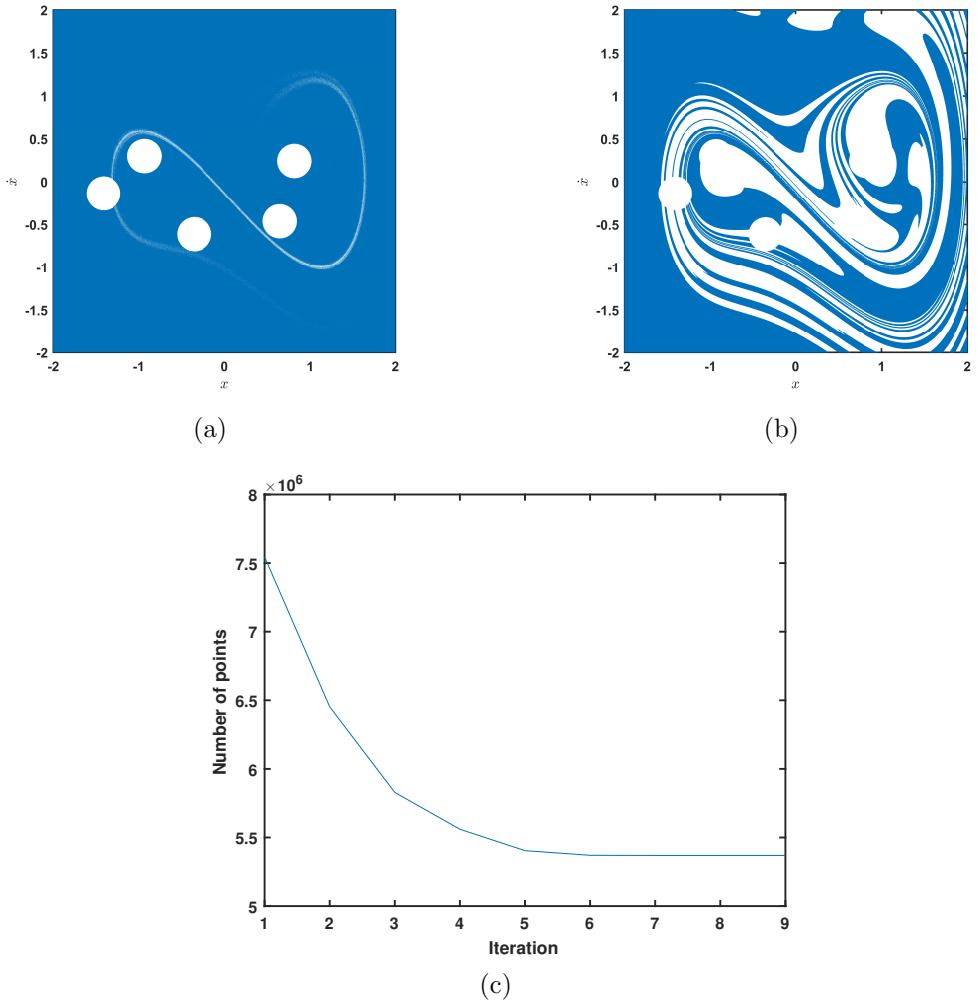

Figure 3.4: Safe set sculpting algorithm: (a) Initial set to start the Sculpting Algorithm. (b) Final Safe Set after 9 iterations. (c) Number of points per iteration. The Sculpting Algorithm has been applied for white noise of amplitude $\sigma = 0.002$. The control has been applied at discrete time interval of T with $T = 2\pi$ and upper bound of the control $u_0(1) = 0.06$. Numerical integration has been done using the Euler-Maruyama scheme. In each step, part of the region Q is removed. Blue colored regions represent the part of the set that remains after each iteration. After several iterations, there is convergence to a safe set, which is represented by Q_∞ as shown in (b).

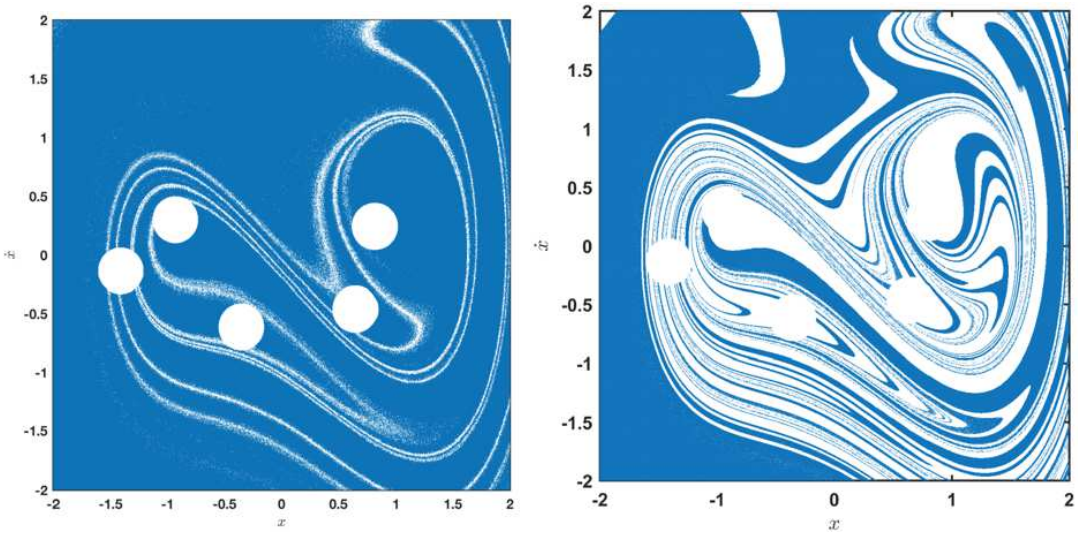

(a) Initial Set

(b) Largest Safe Region

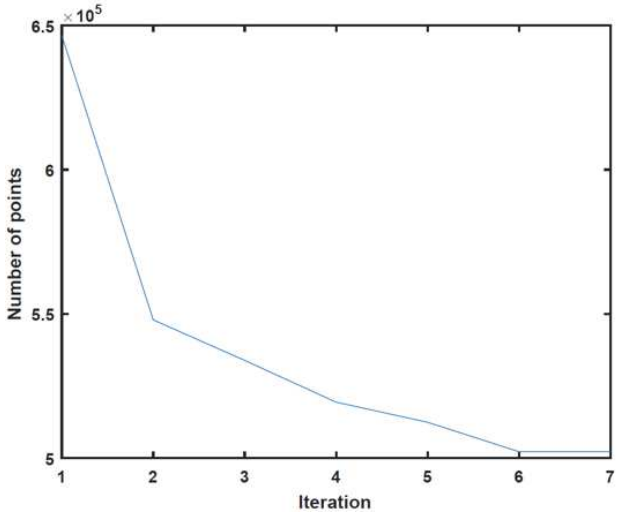

(c) Number of Grid Points after each Iteration

Figure 3.5: Safe set sculpting algorithm: (a) Initial set to start the Sculpting Algorithm. (b) Final Safe Set after 7 iterations. (c) Number of points per iteration. The Sculpting Algorithm has been applied for white noise of amplitude $\sigma = 0.002$. The control has been applied at discrete time interval of $2T$ with $T = 2\pi$ and upper bound of the control $u_0(2) = 0.04$. Numerical integration has been done using the Euler-Maruyama scheme. In each step, part of the region Q is removed. Blue colored regions represent the part of the set that remains after each iteration. After several iterations, there is convergence to a safe set, which is represented by Q_∞ as shown in (b).

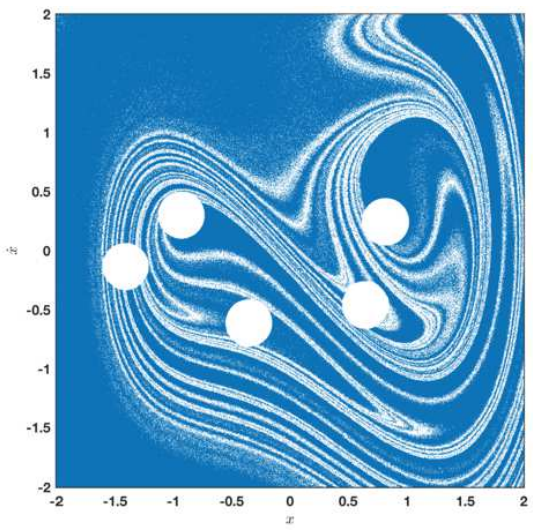

(a) Initial Set

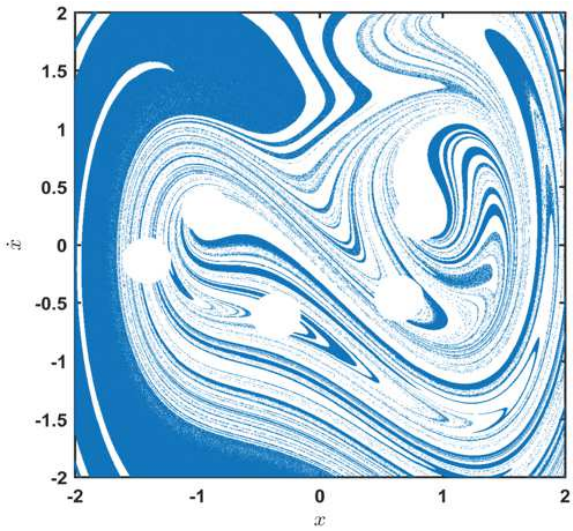

(b) Largest Safe Region

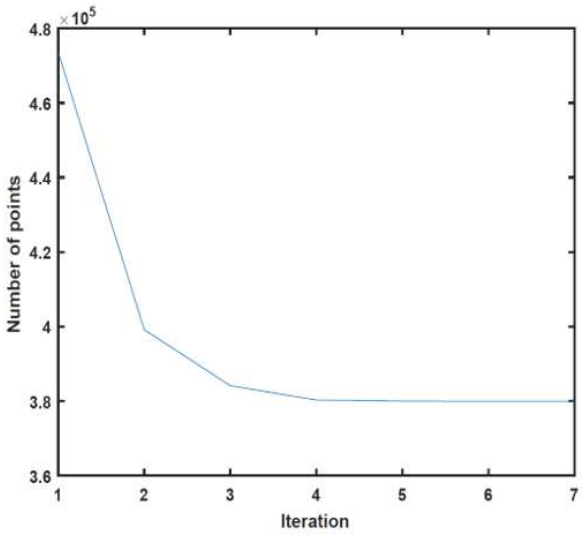

(c) Number of Grid Points after each Iteration

Figure 3.6: Safe set sculpting algorithm: (a) Initial set to start the Sculpting Algorithm. (b) Final Safe Set after 7 iterations. (c) Number of points per iteration. The Sculpting Algorithm has been applied for white noise of amplitude $\sigma = 0.002$. The control has been applied at discrete time interval of $3T$ with $T = 2\pi$ and upper bound of the control $u_0(3) = 0.035$. Numerical integration has been done using the Euler-Maruyama scheme. In each step, part of the region Q is removed. Blue colored regions represent the part of the set that remains after each iteration. After several iterations, there is convergence to a safe set, which is represented by Q_∞ as shown in (b).

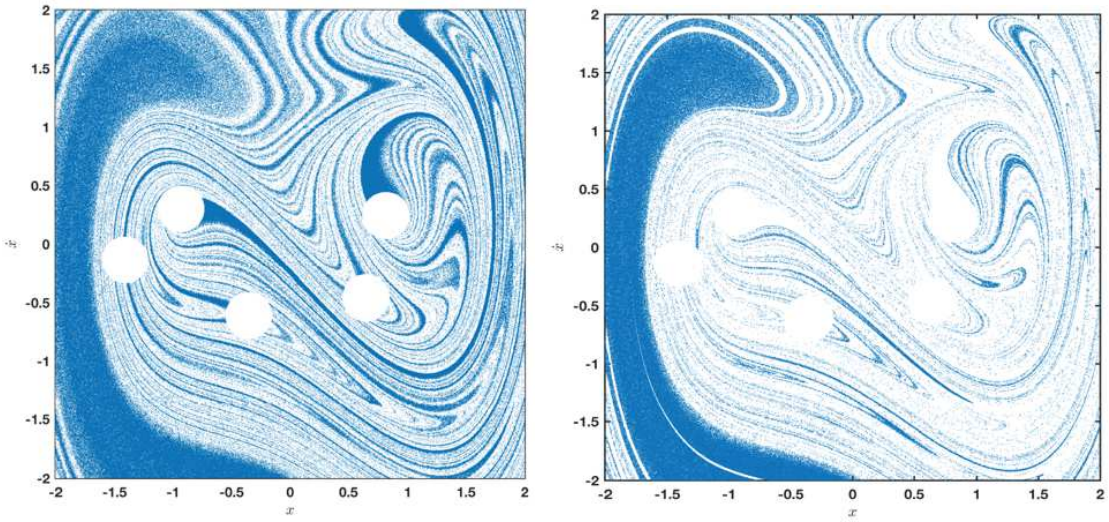

(a) Initial Set

(b) Largest Safe Region

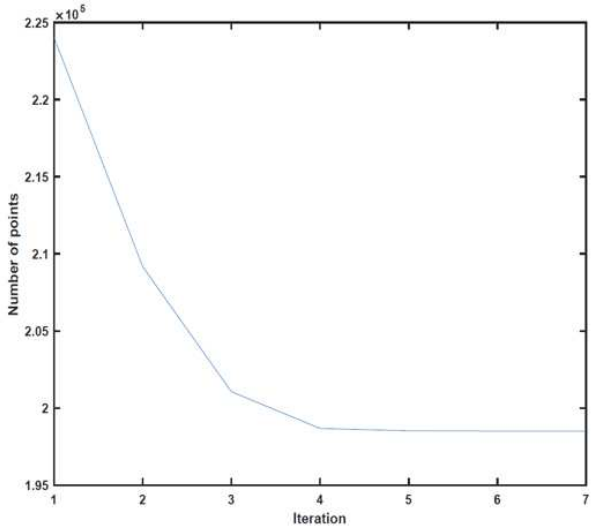

(c) Number of Grid Points after each Iteration

Figure 3.7: Safe set sculpting algorithm: (a) Initial set to start the Sculpting Algorithm. (b) Final Safe Set after 7 iterations. (c) Number of points per iteration. The Sculpting Algorithm has been applied for white noise of amplitude $\sigma = 0.002$. The control has been applied at discrete time interval of $5T$ with $T = 2\pi$ and upper bound of the control $u_0(5) = 0.04$. Numerical integration has been done using the Euler-Maruyama scheme. In each step, part of the region Q is removed. Blue colored regions represent the part of the set that remains after each iteration. After several iterations, there is convergence to a safe set, which is represented by Q_∞ as shown in (b).

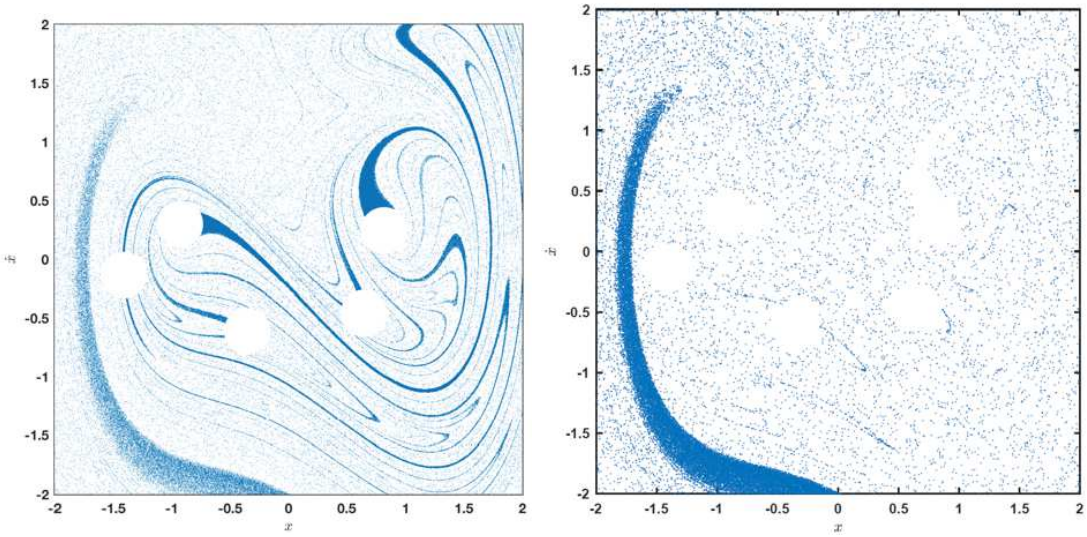

(a) Initial Set

(b) Largest Safe Region

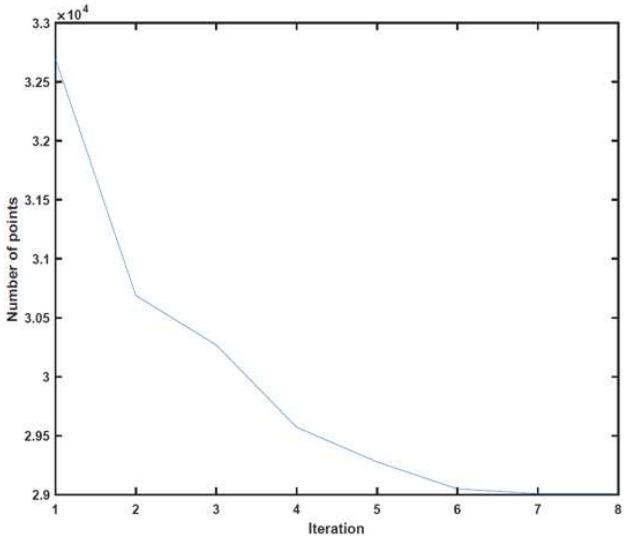

(c) Number of Grid Points after each Iteration

Figure 3.8: Safe set sculpting algorithm: (a) Initial set to start the Sculpting Algorithm. (b) Final Safe Set after 8 iterations. (c) Number of points per iteration. The Sculpting Algorithm has been applied for white noise of amplitude $\sigma = 0.002$. The control has been applied at discrete time interval of $10T$ with $T = 2\pi$ and upper bound of the control $u_0(10) = 0.07$. Numerical integration has been done using the Euler-Maruyama scheme. In each step, part of the region Q is removed. Blue colored regions represent the part of the set that remains after each iteration. After several iterations, there is convergence to a safe set, which is represented by Q_∞ as shown in (b).

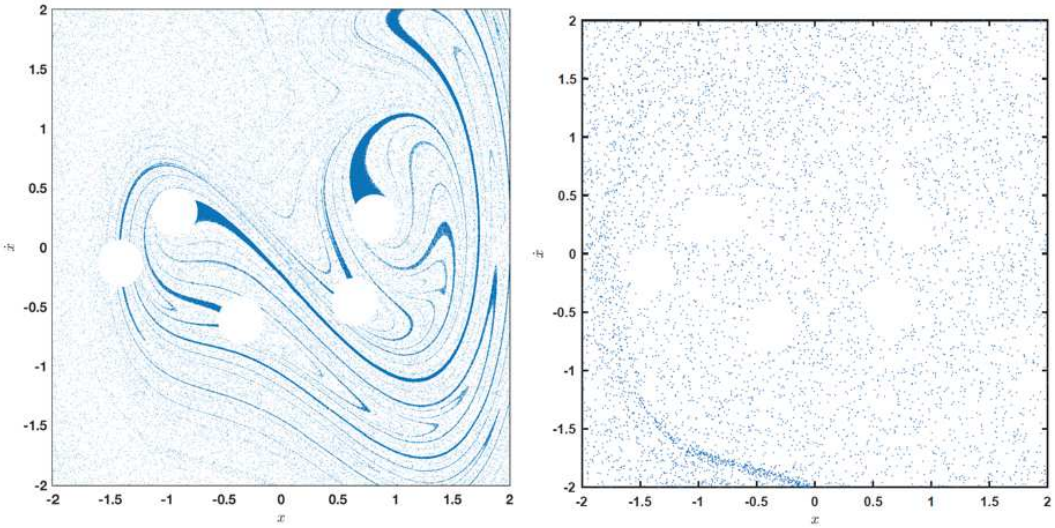

(a) Initial Set

(b) Largest Safe Region

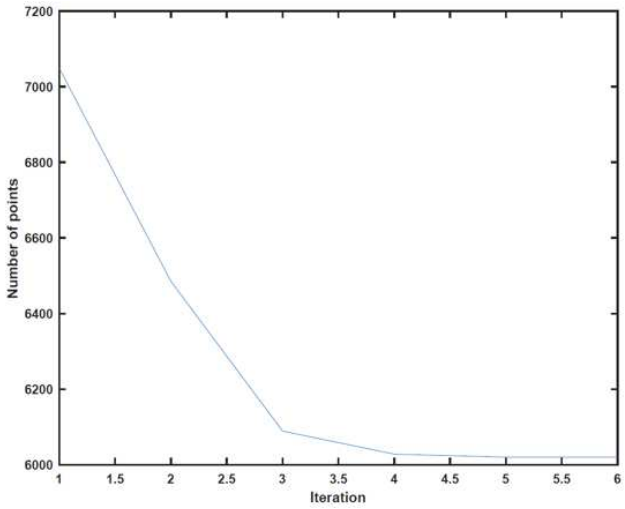

(c) Number of Grid Points after each Iteration

Figure 3.9: Safe set sculpting algorithm: (a) Initial set to start the Sculpting Algorithm. (b) Final Safe Set after 6 iterations. (c) Number of points per iteration. The Sculpting Algorithm has been applied for white noise of amplitude $\sigma = 0.002$. The control has been applied at discrete time interval of $15T$ with $T = 2\pi$ and upper bound of the control $u_0(15) = 0.08$. Numerical integration has been done using the Euler-Maruyama scheme. In each step, part of the region Q is removed. Blue colored regions represent the part of the set that remains after each iteration. After several iterations, there is convergence to a safe set, which is represented by Q_∞ as shown in (b).

The safe set Sculpting Algorithm has been applied to a map associated with the Duffing oscillator. The results with different discrete time control are shown in Figures 3.4 to 3.9. It is found that there is always a minimum value of control $u_0(r)$ which corresponds to the smallest $u_0(r)$ for which there exists a safe set. For a control bound less than $u_0(r)$, there were no safe sets for the Duffing oscillator given by equation (3.17). The safe set disappears for values of the control bound smaller than $u_0(r)$, because for all of the points in Q there is always an admissible noise (within the disturbance bound) for which there is no admissible control (within the control bound) able to put the trajectory again on any safe region. Therefore the algorithm converges to the empty set. The control bound values $u_0(r)$ with different clocking time are presented in Table 3.2.

3.3 Studies of Case with Bounded Noise

As a further study, for a particular value of bounded noise, the results obtained by using the Euler-Maruyama scheme and the Runge-Kutta method are discussed. In particular, the Duffing system given by equation (3.17) is studied. For the current section, the Sculpting Algorithm is applied to the time-2π map (i.e., control at each T).

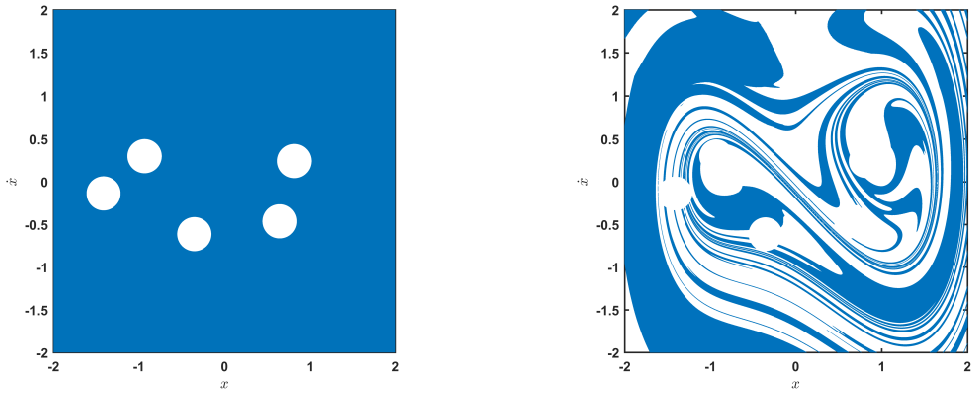

(a)

(b)

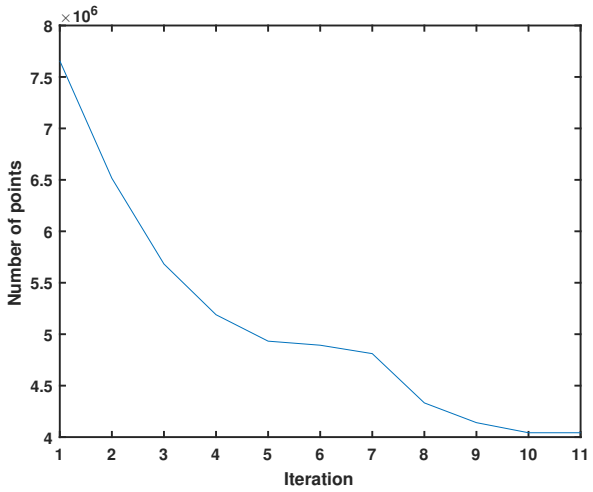

(c)

Figure 3.10: Safe set sculpting algorithm: (a) Initial set to start the Sculpting Algorithm. (b) Final Safe Set after 11 iterations. (c) Number of points per iteration. The Sculpting Algorithm has been applied for a case with noise that is bounded by $\xi_0 = 0.08$, and upper bound of the control $u_0 = 0.0475$. Numerical integration has been carried by using the Runge-Kutta method. In each step, part of the region Q is removed. Blue colored regions represent the part of the set that remains after each iteration. After several iterations, there is convergence to a safe set, which is represented by Q_∞ as shown in (b).

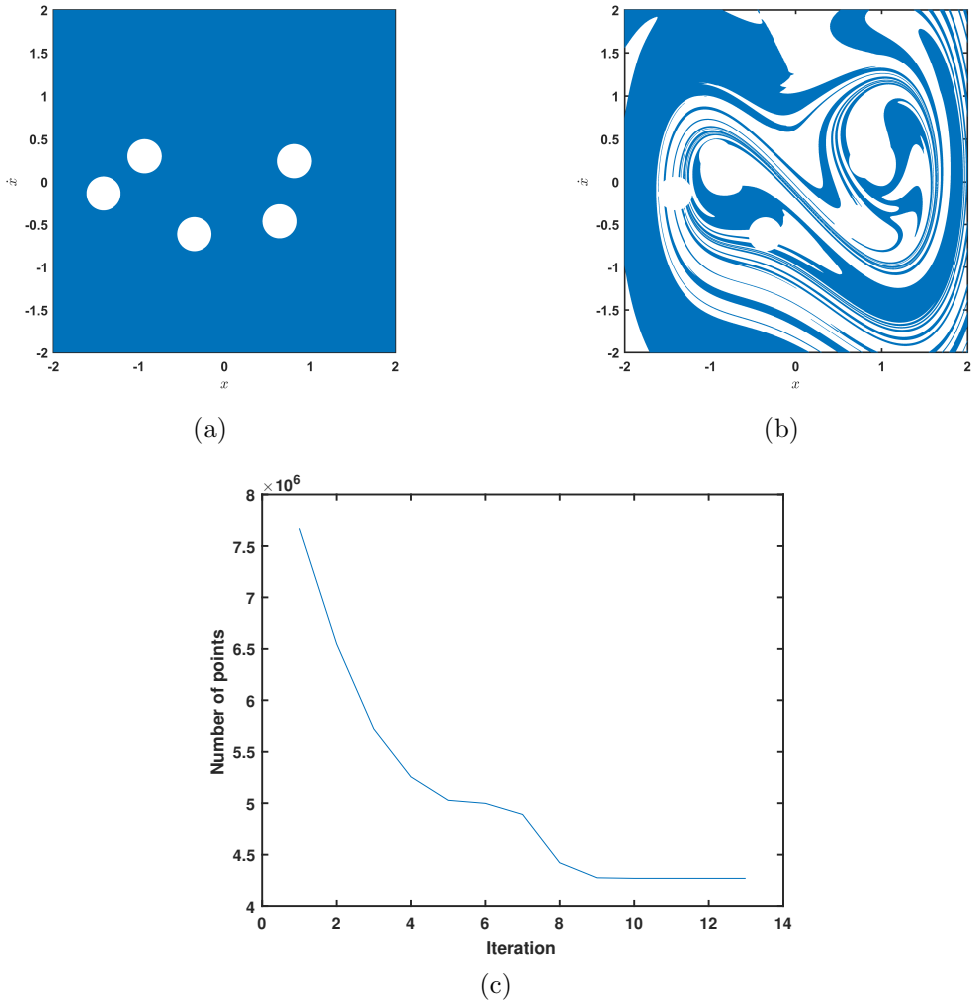

Figure 3.11: Safe set sculpting algorithm: (a) Initial set to start the Sculpting Algorithm. (b) Final Safe Set after 13 iterations. (c) Number of points per iteration. The Sculpting Algorithm has been applied for noise that is bounded by $\xi_0 = 0.08$, and upper bound of the control $u_0 = 0.0475$. Numerical integration has been done using the Euler-Maruyama scheme. In each step, part of the region Q is removed. Blue colored regions represent the part of the set that remains after each iteration. After several iterations, there is convergence to a safe set, which is represented by Q_∞ as shown in (b).

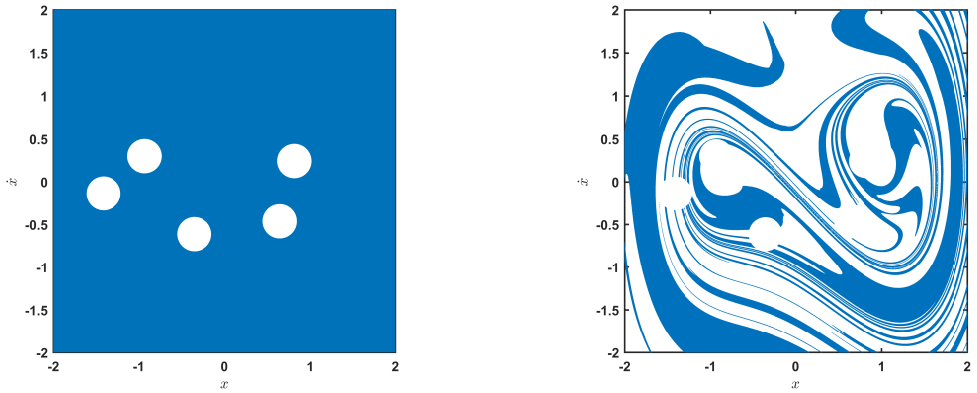

(a) (b)

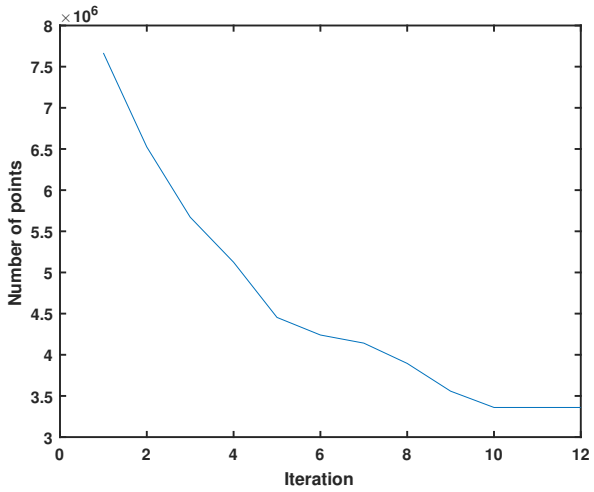

(c)

Figure 3.12: Safe set sculpting algorithm: (a) Initial set to start the Sculpting Algorithm (b) Final Safe Set after 12 iterations (c) Number of points per iteration. The Sculpting Algorithm has been applied for noise that is bounded by $\xi_0 = 0.08$, and upper bound of the control $u_0 = 0.0470$. Numerical integration has been done using the Euler-Maruyama scheme. In each step, part of the region Q is removed. Blue colored regions represent the part of the set that remains after each iteration. After several iterations, there is convergence to a safe set, which is represented by Q_∞ as shown in (b).

3.3.1 Implementation Based on Runge-Kutta Scheme

The author starts with an upper bound of noise $\xi_0 = 0.08$, and an upper bound of control $u_0 = 0.0475$. For this case, the Runge-Kutta method is used to find the image q_{n+1} of any point q_n. Furthermore, the Sculpting Algorithm is applied to get a safe set. The results are shown in Figure 3.10 (Sabuco *et al.*, 2012a).

It has been found that it is possible to maintain a chaotic behavior indefinitely with an upper bound of control $u_0 = 0.0475$, which is smaller than the upper bound of the disturbance $\xi_0 = 0.08$. For any upper bound of control less than 0.0475 for the same upper bound of noise $\xi_0 = 0.08$, no safe set was found; that is the obtained safe set is an empty set.

3.3.2 Implementation Based on Euler-Maruyama Scheme

Here, as in the previous section, the numerical simulation is started with an upper bound of noise $\xi_0 = 0.08$, and an upper bound of control $u_0 = 0.0475$. The Euler-Maruyama scheme has been used to find the image q_{n+1} of any point q_n. Next, the Sculpting Algorithm has been applied to get a safe set. The results are shown in Figure 3.11. It is also shown clearly here, how the safe set obtained with the Euler-Maruyama integration scheme (panel 13 in Figure 3.11), is substantially different from the safe set obtained with the Runge-Kutta integration scheme (panel 11 in Figure 3.10), for the same parameters bounds on control and noise.

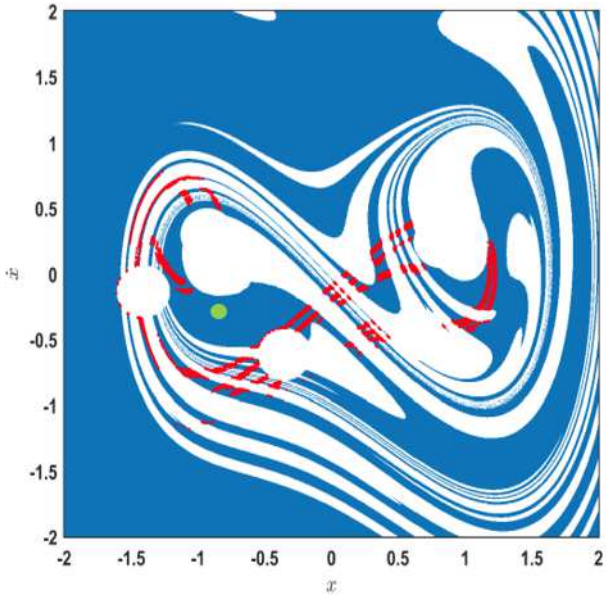

(a)

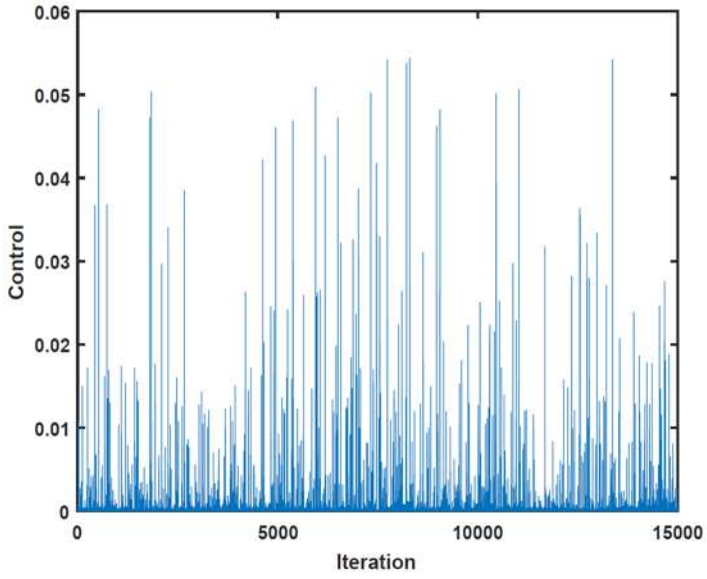

(b)

Figure 3.13: Controlled Trajectory: In plot (a), the trajectory obtained by considering as initial condition the point shown as green dot, which is inside the safe sate (blue region) in the presence of white noise ($\sigma = 0.002$). The control has been applied at discrete time intervals of T with $T = 2\pi$. (The associated safe set is shown in Figure 3.4.) The red dots represent the controlled trajectory for 15000 iterations. In plot (b), the applied control input for each iteration is shown. The control is bounded by the value $u_0(1) = 0.06$ that is the upper bound of the control for this particular safe set.

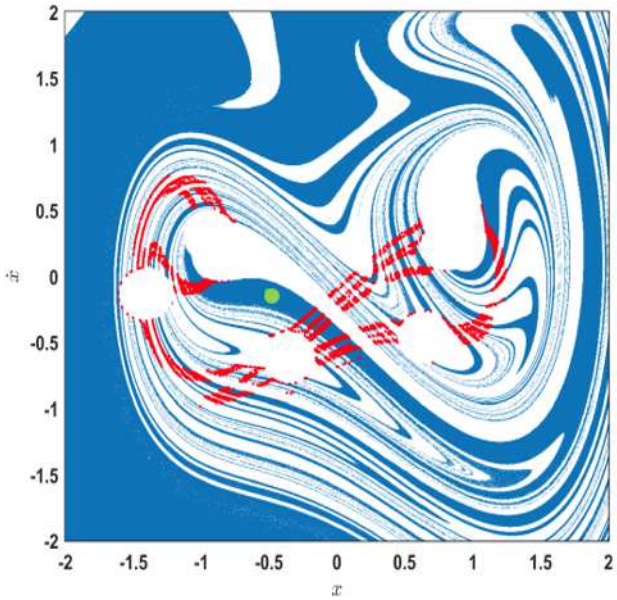

(a)

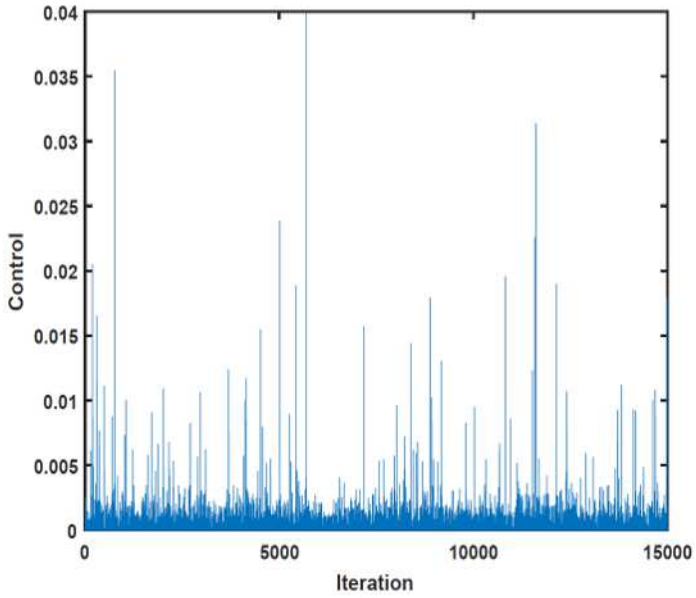

(b)

Figure 3.14: Controlled Trajectory: In plot (a), the trajectory obtained by considering as initial condition the point shown as green dot, which is inside the safe sate (blue region) in the presence of white noise ($\sigma = 0.002$). The control has been applied at discrete time intervals of $2T$ with $T = 2\pi$. (The associated safe set is shown in Figure 3.5.) The red dots represent the controlled trajectory for 15000 iterations. In plot (b), the applied control input for each iteration is shown. The control is bounded by the value $u_0(2) = 0.04$ that is the upper bound of the control for this particular safe set.

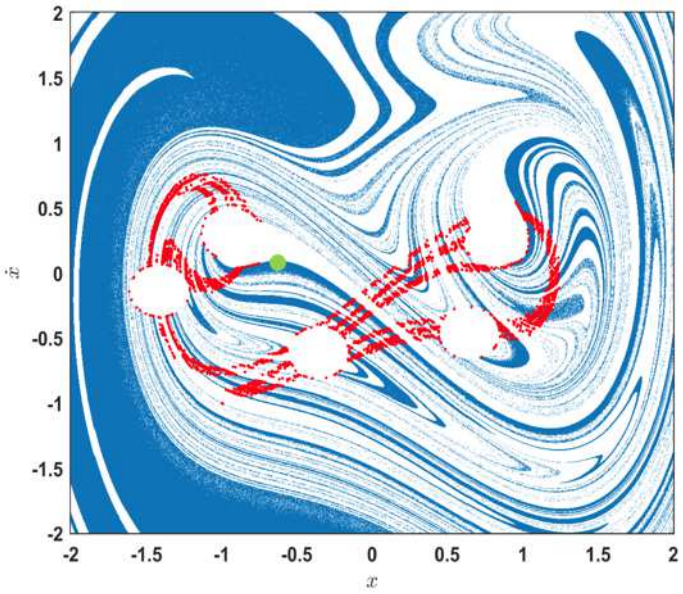

(a)

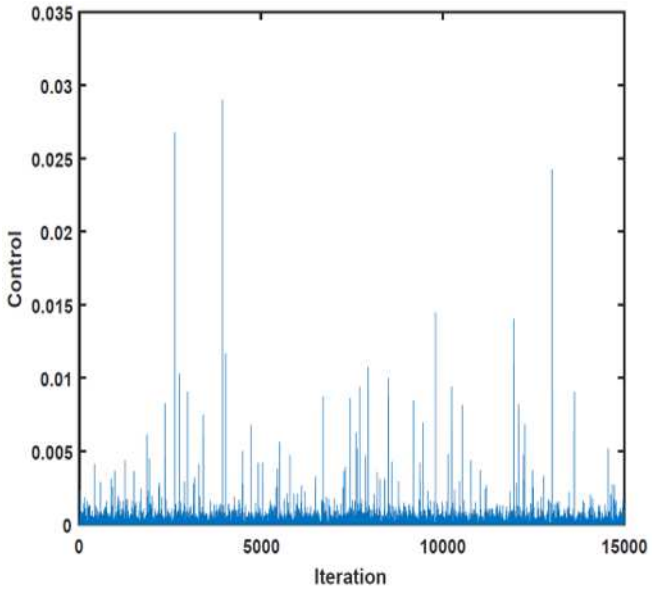

(b)

Figure 3.15: Controlled Trajectory: In plot (a), the trajectory obtained by considering as initial condition the point shown as green dot, which is inside the safe sate (blue region) in the presence of white noise ($\sigma = 0.002$). The control has been applied at discrete time intervals of $3T$ with $T = 2\pi$. (The associated safe set is shown in Figure 3.6.) The red dots represent the controlled trajectory for 15000 iterations. In plot (b), the applied control input for each iteration is shown. The control is bounded by the value $u_0(3) = 0.035$ that is the upper bound of the control for this particular safe set.

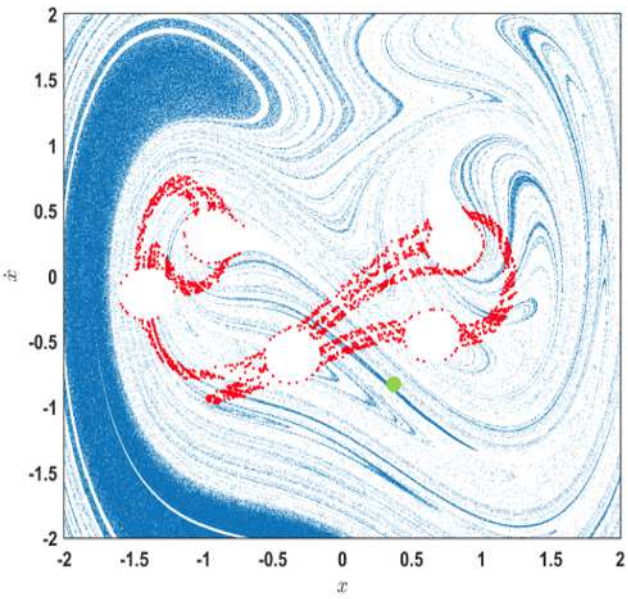

(a)

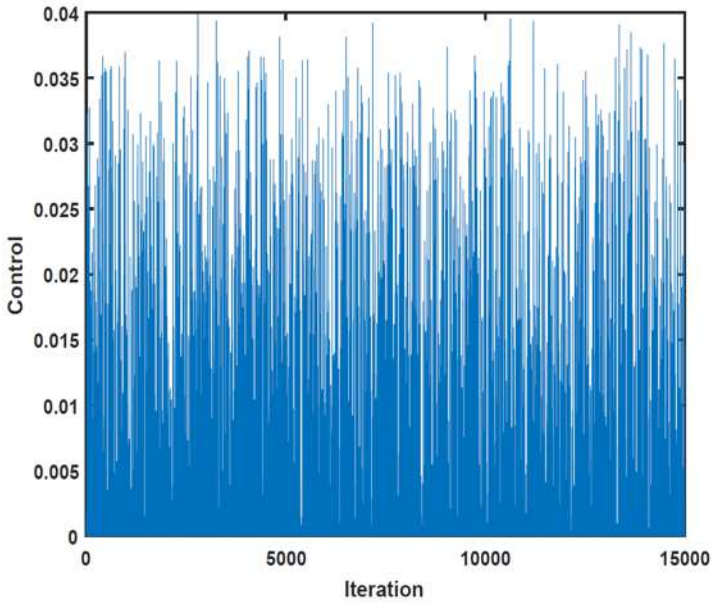

(b)

Figure 3.16: Controlled Trajectory: In plot (a), the trajectory obtained by considering as initial condition the point shown as green dot, which is inside the safe sate (blue region) in the presence of white noise ($\sigma = 0.002$). The control has been applied at discrete time intervals of $5T$ with $T = 2\pi$. (The associated safe set is shown in Figure 3.7.) The red dots represent the controlled trajectory for 15000 iterations. In plot (b), the applied control input for each iteration is shown. The control is bounded by the value $u_0(5) = 0.04$ that is the upper bound of the control for this particular safe set.

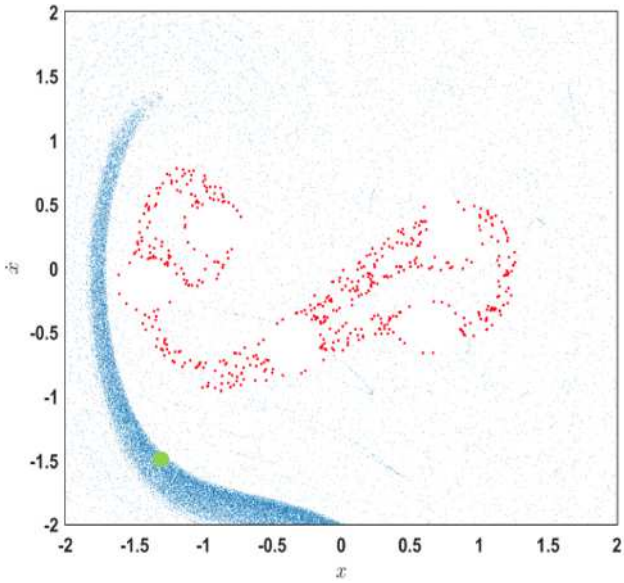

(a)

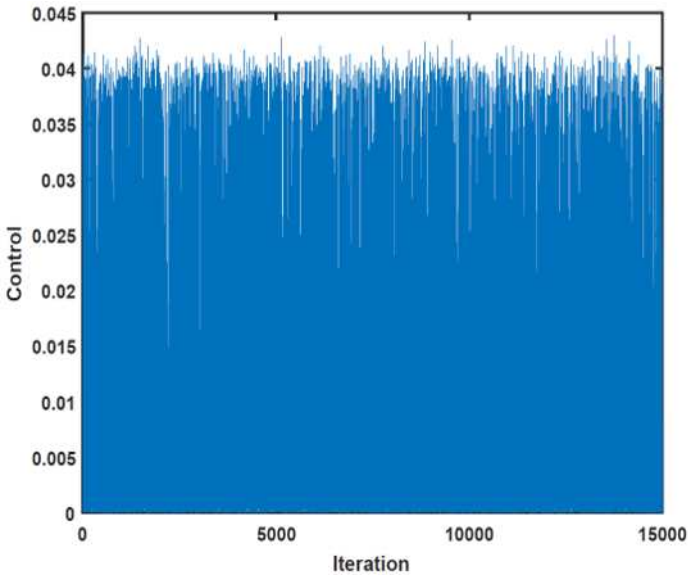

(b)

Figure 3.17: Controlled Trajectory: In plot (a), the trajectory obtained by considering as initial condition the point shown as green dot, which is inside the safe sate (blue region) in the presence of white noise ($\sigma = 0.002$). The control has been applied at discrete time intervals of $10T$ with $T = 2\pi$. (The associated safe set is shown in Figure 3.8.) The red dots represent the controlled trajectory for 15000 iterations. In plot (b), the applied control input for each iteration is shown. The control is bounded by the value $u_0(10) = 0.07$ that is the upper bound of the control for this particular safe set.

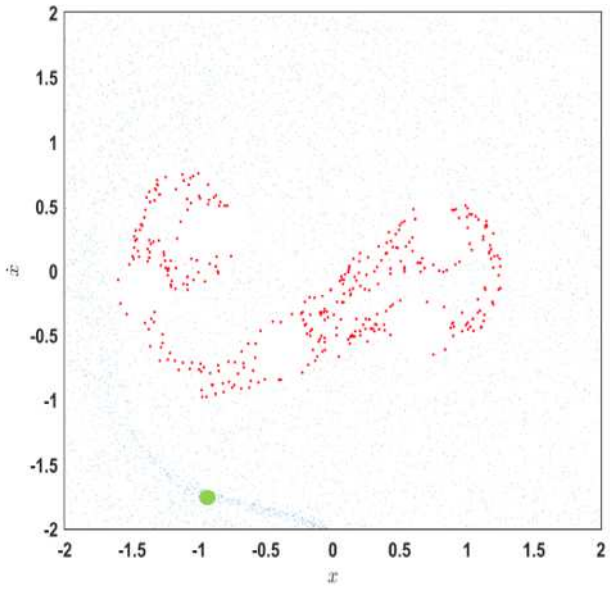

(a)

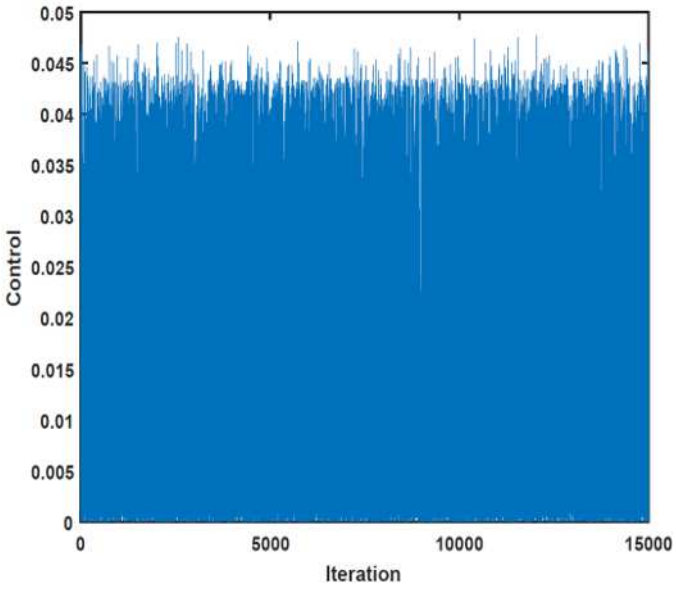

(b)

Figure 3.18: Controlled Trajectory: In plot (a), the trajectory obtained by considering as initial condition the point shown as green dot, which is inside the safe sate (blue region) in the presence of white noise ($\sigma = 0.002$) . The control has been applied at discrete time intervals of $15T$ with $T = 2\pi$. (The associated safe set is shown in Figure 3.9.) The red dots represent the controlled trajectory for 15000 iterations. In plot (b), the applied control input for each iteration is shown. The control is bounded by the value $u_0(15) = 0.08$ that is the upper bound of the control for this particular safe set.

Table 3.2: Control bound and safe regions for the applied partial control

Control Time Interval	**Control Bound u_0**	**Safe Region (% of Total Area)**
T	$u_0(1) = 0.06$	62
$2T$	$u_0(2) = 0.04$	50.1
$3T$	$u_0(3) = 0.035$	37.9
$5T$	$u_0(5) = 0.04$	19.8
$10T$	$u_0(10) = 0.07$	2.9
$15T$	$u_0(15) = 0.08$	0.6

It has been found that it is possible to maintain chaotic behavior indefinitely with an upper bound of control $u_0 = 0.0475$. With the use of the Runge-Kutta scheme for any upper bound of control less than 0.0475, no safe set exists. But, with the use of the Euler-Maruyama scheme, it has been found that a minimum upper bound for the existence of a safe set is $u_0 = 0.0470$. This suggests that with the use of the Euler-Maruyama scheme, one can have a safe set with a lower control value than with that for the Runge-Kutta scheme. For example, the safe set for a control $u_0 = 0.0470$ is shown in Figure 3.12. With this numerical integration scheme, for any upper bound of control smaller than 0.0470 for the same upper bound of noise $\xi_0 = 0.08$, no safe set was found. It other words, the obtained safe set is an empty set.

The controlled trajectories of 15000 iterations in the presence of white noise ($\sigma = 0.002$) have been shown in Figures 3.13 to 3.18 where the control is bounded in value by $u_0(r)$ as represented in Table 3.2.

3.4 Conclusions

In this chapter, the author has presented the partial control method based on the Euler-Maruyama scheme for finding safe sets for continuous time systems with white noise. A harmonically forced Duffing oscillator has been used as a representative prototype to illustrate the development as well as to make comparisons with prior work, wherein a bounded noise has been used. As shown in this work, by using the control method developed, one can keep trajectories confined inside a prescribed region and maintain a transient chaotic behavior. For the control method presented here, the value of the upper bound of control $u_0(r)$ has been chosen based on the value of noise amplitude σ, clocking time rT, and harmonic forcing amplitude F. This is the first demonstration of partial control applied at time interval other than T. It has been observed that the system can be controlled with a relatively smaller magnitude control bound (u_0) when the control is applied at different discrete time intervals (e.g., here, the minimum control bound $u_0(3) = 0.035$, when the control is applied at each time interval of $3T$) but, there is a limitation in further increasing the applied control time interval if the response of the system escapes in between.

Chapter 4: Noise-Influenced Rotor Dynamics

In this chapter, torsional vibrations and whirling motions of a Jeffcott rotor confined within a fixed stator are analytically and numerically explored for both forward and backward whirling motions. The work in this chapter is a part of the study conducted by Agarwal and Balachandran (2019b). The governing equations are constructed in a generalized polar coordinate system for describing non-constant whirling speeds and impact motions. Torsional vibrations and whirling motions are examined by using the derived reduced-order equations. It is found that both forward and backward whirling motions with contact have different, but constant steady state whirling speeds. Furthermore, the effects of introduction of noise in driving speed have been explored. The trigonometric representation of non-Gaussian excitation as a harmonic excitation with a random phase modulation is modified by introducing a new state variable. The Euler-Maruyama simulation scheme is used for numerical integration. It is observed that for a small value of friction coefficient, a sufficient level of noise amplitude affects the system dynamics for the cases of forward and backward whirling with contact.

The rest of this chapter is organized as follows. In Section 4.1, the modeling efforts undertaken to derive the governing equations with a generalized polar

Table 4.1: Nomenclature describing the quantities governing the Jeffcott rotor.

Nomenclature	
r	Radial distance between geometric centers of rotor and stator
ϕ	Whirl angle
θ	Torsional angle
$\dot{\phi}$	Whirling speed (frequency)
$\dot{\Omega}$	Rotor driving speed (frequency)
M	Rotor mass
m	Unbalanced mass
R	Rotor radius
e	Eccentricity
δ	static clearance between rotor and stator
k_b	Lateral stiffness
k	Torsion stiffness
c_b	Lateral damping
c_b	Torsion damping
J	Total rotary inertia of the rotor with mass imbalance
ω_{for}	Forward whirling speed
ω_{back}	Backward whirling speed
μ	Friction coefficient
$\dot{W}(t)$	White Gaussian noise
σ	Amplitude of noise for numerical simulations
x_i	State space variables

coordinate system are presented. Further, reduced-order equations are derived for continuous rotor-stator contact. Euler-Maruyama simulations are presented. In Section 4.2, the numerical results for both deterministic and stochastic dynamics are presented. Finally, conclusions are drawn and presented together in Section 4.3.

4.1 Mathematical Modeling

4.1.1 Governing Equations Without Noise: Full Model

A schematic diagram of an extended Jeffcott rotor is shown in Figure 4.1(a). This system is capable of exhibiting torsional vibrations as well as whirling motions

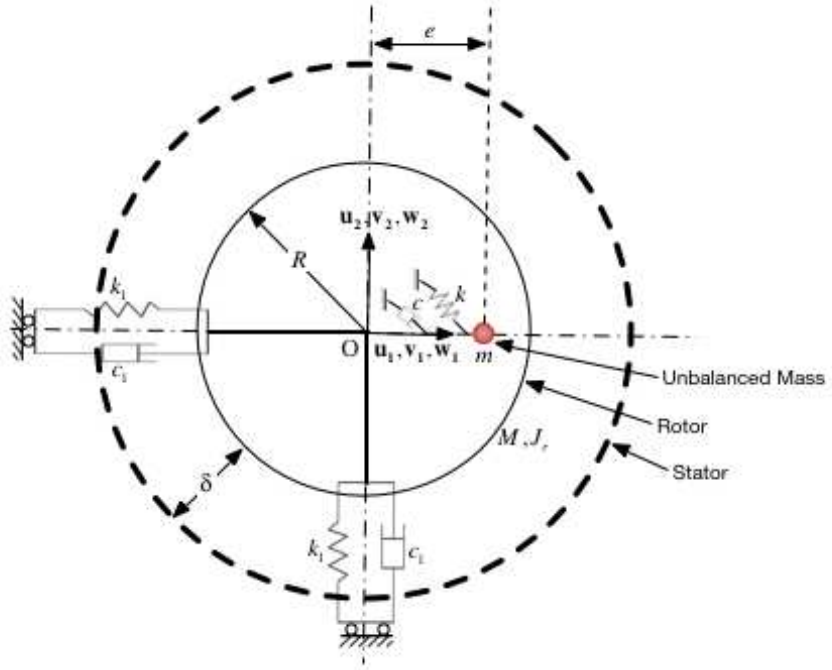

(a)

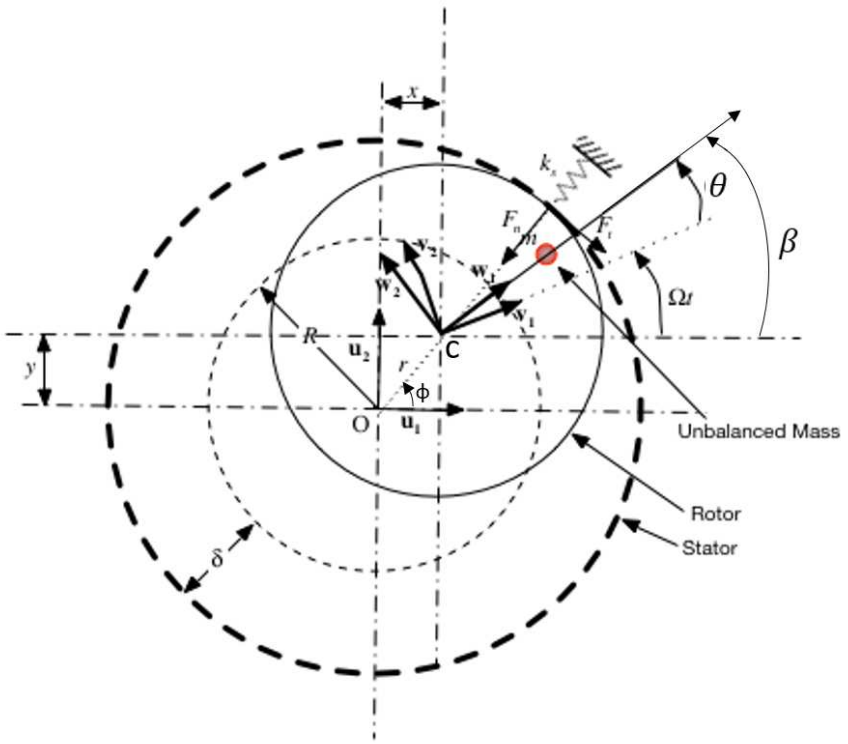

(b)

Figure 4.1: Extended Jeffcott Rotor-Stator Model: (a) Static configuration (rotor within the stator). (b) Dynamic configuration (continuous rotor-stator contact).

with or without stator contact. The author chose (r, ϕ, θ) as generalized coordinates to understand the dynamics of the Jeffcott rotor. Here, r represents the distance of the geometric center of the moving rotor (point 'C') from the fixed center of the stator (point 'O'). ϕ and θ represent whirling angle and torsional deformation respectively. It can also be said that r and ϕ account for lateral deformation and θ accounts for torsional deformation. The center of rotor with radius R, mass M, and an unbalanced mass m with eccentricity e coincides with the center of the stator. The static clearance between the rotor and the stator is δ. The geometric center of the rotor without the mass imbalance coincides with its center of mass. Due to a choice of symmetric rotor, the equivalent lateral stiffness values is $k_x = k_y = k_b$ and the lateral damping is assumed to be $c_x = c_y = c_b$. The torsion stiffness is k and the associated torsion damping is c. For a particular dynamic state, the rotor-stator system configuration is displayed in Figure 4.1(b). The gyroscopic effects are assumed to be negligible and it is assumed that the rotor experiences planar motion. The gravity loading is normal to the rotor plane. There are three sets of unit vectors, namely $\mathbf{u_1}$-$\mathbf{u_2}$, $\mathbf{v_1}$-$\mathbf{v_2}$, and $\mathbf{w_1}$-$\mathbf{w_2}$, which are placed at the geometric center of the rotor. $\mathbf{u_1}$ and $\mathbf{u_2}$ are orthogonal unit vectors in an inertial frame. The orthogonal unit vectors $\mathbf{v_1}$ and $\mathbf{v_2}$, which are fixed to the geometric center of the rotor, rotate with the driving angular speed Ω with respect to $\mathbf{u_1}$-$\mathbf{u_2}$. The orthogonal unit vectors $\mathbf{w_1}$ and $\mathbf{w_2}$, which also are fixed to the geometric center of the rotor, are displaced by a radial amount of torsional deformation $\theta(t)$ with respect to the set $\mathbf{v_1}$-$\mathbf{v_2}$. Furthermore, no gyroscopic effects due to rotations about the $\mathbf{u_1}$ and $\mathbf{u_2}$ axes have been taken into account and the rotor is only able to undergo planar

motions. A constraint as a result of planar motion is imposed as $\mathbf{u_3} = \mathbf{v_3} = \mathbf{w_3}$ for all time t, where $\mathbf{u_3} = \mathbf{u_1} \times \mathbf{u_2}$, $\mathbf{v_3} = \mathbf{v_1} \times \mathbf{v_2}$, and $\mathbf{w_3} = \mathbf{w_1} \times \mathbf{w_2}$. In static configuration, at time $t = 0$, $\mathbf{u_1} \equiv \mathbf{v_1} \equiv \mathbf{w_1}$, $\mathbf{u_2} \equiv \mathbf{v_2} \equiv \mathbf{w_2}$ and the mass imbalance m is located along the $\mathbf{u_1}$-axis.

The governing equations of motion have been derived by using Lagrange's equations. To do this, the kinetic energy of the rotor system with mass imbalance is constructed as

$$T = \frac{1}{2}M(\dot{r}^2 + r^2\dot{\phi}^2) + \frac{J_o\dot{\beta}^2}{2} + \frac{m}{2}\Big[\dot{r}^2 + r^2\dot{\phi}^2 + e^2\dot{\beta}^2 + 2e\dot{\beta}\Big\{\dot{r}\sin(\phi-\beta) + r\dot{\phi}\cos(\phi-\beta)\Big\}\Big] \tag{4.1}$$

where J_o is the mass moment of inertia of the rotor without mass imbalance about the axis normal to the rotor plane and passing through its center. $\beta(t) \equiv \beta = \theta(t) + \Omega t$ includes the torsional deformation and rigid body rotation. The overdots represent derivatives with respect to time. The above equation can be simplified as

$$T = \frac{1}{2}(M+m)(\dot{r}^2 + r^2\dot{\phi}^2) + \frac{J\dot{\beta}^2}{2} + me\dot{\beta}\Big\{\dot{r}\sin(\phi-\beta) + r\dot{\phi}\cos(\phi-\beta)\Big\} \tag{4.2}$$

where $J = J_0 + me^2$ is the total rotary inertia of the rotor with mass imbalance. The potential energy of the system can be expressed as

$$V = \frac{1}{2}\left[k_b r^2 + k\theta^2\right] \tag{4.3}$$

The Rayleigh's dissipation function is given by

$$D = \frac{1}{2}\left[c_b(\dot{r}^2 + r^2\dot{\phi}^2) + c\dot{\theta}^2\right] \tag{4.4}$$

Then, the governing equations of motion are derived using Lagrange's equations and can be simplified as

$$\begin{cases} (M+m)\ddot{r} + me\sin(\phi-\beta)\ddot{\theta} + c_b\dot{r} + k_b r \\ \quad = (M+m)r\dot{\phi}^2 + me\dot{\beta}^2\cos(\phi-\beta) - F_n \\ \\ (M+m)r\ddot{\phi} + me\cos(\phi-\beta)\ddot{\theta} + c_b r\dot{\phi} \\ \quad = -2(M+m)\dot{r}\dot{\phi} - me\dot{\beta}^2\sin(\phi-\beta) + F_t \\ \\ me\sin(\phi-\beta)\ddot{r} + mer\cos(\phi-\beta)\ddot{\phi} + J\ddot{\theta} + c\dot{\theta} + k\theta \\ \quad = me\left[r\dot{\phi}^2\sin(\phi-\beta) - 2\dot{r}\dot{\phi}\cos(\phi-\beta)\right] + M_t \end{cases} \tag{4.5}$$

The contact forces F_n, F_t, and the moment M_t will be zero until the displacement r of the center of the rotor, becomes equal to the clearance δ, or the rotor comes into contact with the stator.

The contact normal force acting on the rotor can explicitly be written as

$$F_n = \begin{cases} 0 & \text{for } r \le \delta \\ \\ k_s(r-\delta) & \text{for } r > \delta \end{cases} \tag{4.6}$$

Given the friction coefficient μ, the friction force is given by

$$F_t = -\mu F_n \tag{4.7}$$

The moment can be written as

$$M_t = F_t R \tag{4.8}$$

The friction model is adapted from Leine and Nijmeijer (2013), Thomsen (2013), and Vlajic *et al.* (2014b), and it can be expressed as

$$\begin{cases} \mu(v_{rel}) & = \mu_s \text{sgn}(v_{rel}) - \frac{3}{2}(\mu_s - \mu_m)\left(\frac{v_{rel}}{v_m} - \frac{1}{3}\left(\frac{v_{rel}}{v_m}\right)^3\right) \\ & = \mu_s \text{sgn}(v_{rel}) - \mu_1 v_{rel} + \mu_3 v_{rel}^3 \end{cases} \tag{4.9}$$

where μ_s is the static friction coefficient, and μ_m is the minimum friction coefficient at $v_{rel} = v_m$.

The signum function used in equation (4.9) does lead to difficulties when numerically integrating the system. Therefore, as in Vlajic *et al.* (2014b), during numerical integration, equation (4.9) is replaced with

$$\mu(v_{rel}) = \mu_s \frac{2}{\pi} \arctan(\delta_f v_{rel}) - \frac{3}{2}(\mu_s - \mu_m)\left(\frac{v_{rel}}{v_m} - \frac{1}{3}\left(\frac{v_{rel}}{v_m}\right)^3\right) \tag{4.10}$$

Table 4.2: Parameter values used in simulations

Parameter	Value	Units
c_b	0.02	$N \cdot s/m$
c	1.8 e^{-4}	$N \cdot m \cdot s/rad$
e	0.05	m
M	1	kg
m	0.05	kg
k_b	1	N/m
k_s	$1e^4$	N/m
k	0.05	$N \cdot m/rad$
R	0.05	m
v_m	0.15	m/s
δ	0.01	m
δ_f	$1e^6$	-
μ_s	1.05 μ_m	-
μ_m	{0.005,0.05}	-

where for $\delta_f \gg 1$, normalized arctangent in equation (4.10) closely resembles the signum function in equation (4.9).

The relative speed between the rotor and stator surface at the point of contact is given by

$$v_{rel} = \left(\Omega + \dot{\theta}\right) R + r\dot{\phi} \tag{4.11}$$

where $\dot{\phi}$ and Ω represent the whirling speed and the driving speed respectively. For the current study, the whirling speed is not assumed to be constant unless mentioned.

4.1.2 Governing Equations Without Noise: Continuous Rotor-Stator Contact and Reduced-Order Model

In this section, the rotor is assumed to maintain contact with the stator while the whirling speed is not assumed to be constant, with the corresponding radial displacement $r = \delta$. With the substitution of $r = \delta$, $\dot{r} = 0$, and $\ddot{r} = 0$, the system of equations given by equations (4.5) can be reduced to

$$\begin{cases} (M+m)\delta\ddot{\phi} + me\cos(\phi-\beta)\ddot{\theta} + c_b\delta\dot{\phi} &= -me\dot{\beta}^2\sin(\phi-\beta) + F_t \\ \\ me\delta\cos(\phi-\beta)\ddot{\phi} + J\ddot{\theta} + c\dot{\theta} + k\theta &= me\delta\dot{\phi}^2\sin(\phi-\beta) + M_t \end{cases} \tag{4.12}$$

Given that the eccentricity e is much smaller than the clearance δ and the unbalanced mass m is much smaller than the rotor mass M, which is usually the case in most rotor systems, as in the work of Vlajic *et al.* (2014b), the contact forces can be approximated as

$$\begin{cases} F_n &= (M+m)\delta\dot{\phi}^2 - k_b\delta \\ F_t &= -\mu F_n \\ M_t &= F_t R \end{cases} \tag{4.13}$$

4.1.3 Governing Equations With Noise

In the current section, the rotor drive input includes a deterministic input and white Gaussian noise. The addition of noise can be expressed as

$$\dot{\beta} = \Omega + \dot{\theta}(t) + \sigma \dot{W}(t) \tag{4.14}$$

where the deterministic drive speed component is represented by Ω, $\dot{\theta}$ represents the torsional vibration, and the noise input to the system is represented by $\sigma \dot{W}(t)$, where σ represents the noise amplitude used in the numerical simulation, $W(t)$ represents the standard Wiener process, and $\dot{W}(t)$ is a "mnemonic" derivative.

For the convenience of numerical simulations, the noise amplitude is chosen to be small in comparison to the deterministic drive speed Ω. It can be approximated as

$$\dot{\beta}^2 \approx \left(\Omega + \dot{\theta}(t)\right)^2 + \sigma \left(\Omega + \dot{\theta}(t)\right) \dot{W}(t) \tag{4.15}$$

It is mentioned that in this differential form, one no longer has the derivative of the Brownian motion (which does not exist) but a differential white noise which does exist. Therefore, equations (4.5) and (4.12) in presence of noise are extended in state-space form. As given in equations (4.5), (4.12), and (4.14), the noise is in the phase of a trigonometric function. This is called as trigonometric function representation of non-Gaussian processes where the trigonometric functions represent harmonic

excitation with random phase modulation (Dimentberg, 1988).

Full Model with Noise: The state variables are defined as

$$\begin{cases} x_1 = r; \quad x_4 = \dot{r}; \quad x_7 = \sin(\phi - \beta) \\ x_2 = \phi; \quad x_5 = \dot{\phi}; \quad x_8 = \cos(\phi - \beta) \\ x_3 = \theta; \quad x_6 = \dot{\theta} \end{cases} \tag{4.16}$$

Equation (4.5) can be rewritten in state-space form as

$$
\begin{cases}
\dot{x}_1 = x_4 \\
\dot{x}_2 = x_5 \\
\dot{x}_3 = x_6 \\
(M+m)\dot{x}_4 + mex_7\dot{x}_6 = \Big[- c_b x_4 - k_b x_1 + (M+m)x_1 x_5^2 \\
\quad + mex_8(x_6+\Omega)^2 - F_n + mex_8\sigma(x_6+\Omega)\dot{W}(t)\Big] \\
(M+m)x_1\dot{x}_5 + mex_8\dot{x}_6 = \Big[- c_b x_1 x_5 - 2(M+m)x_4 x_5 \\
\quad - mex_7(x_6+\Omega)^2 + F_t - mex_7\sigma(x_6+\Omega)\dot{W}(t)\Big] \\
mex_7\dot{x}_4 + mex_1x_8\dot{x}_5 + J\dot{x}_6 = \Big[- cx_6 - kx_3 \\
\quad + mex_1x_5^2x_7 - 2mex_4x_5x_8 + M_t\Big] \\
\dot{x}_7 = x_8\Big[x_5 - x_6 - \Omega - \sigma\dot{W}(t)\Big] \\
\dot{x}_8 = -x_7\Big[x_5 - x_6 - \Omega - \sigma\dot{W}(t)\Big]
\end{cases}
\tag{4.17}
$$

In order to carry out numerical studies, the above equations are expressed in the Langevin form as

$$
\begin{cases}
dx_1 = x_4 dt \\
dx_2 = x_5 dt \\
dx_3 = x_6 dt \\
\\
(M+m)dx_4 + mex_7 dx_6 = \Big[-c_b x_4 - k_b x_1 + (M+m)x_1 x_5^2 \\
\quad + mex_8(x_6+\Omega)^2 - F_n \Big] dt + mex_8 \sigma (x_6+\Omega) dW \\
\\
(M+m)x_1 dx_5 + mex_8 dx_6 = \Big[-c_b x_1 x_5 - 2(M+m)x_4 x_5 \\
\quad - mex_7(x_6+\Omega)^2 + F_t \Big] dt - mex_7 \sigma (x_6+\Omega) dW \\
\\
mex_7 dx_4 + mex_1 x_8 dx_5 + J dx_6 = \Big[-cx_6 - kx_3 \\
\quad + mex_1 x_5^2 x_7 - 2mex_4 x_5 x_8 + M_t \Big] dt \\
\\
dx_7 = x_8(x_5 - x_6 - \Omega)dt - \sigma x_8 dW \\
dx_8 = -x_7(x_5 - x_6 - \Omega)dt + \sigma x_7 dW
\end{cases}
\tag{4.18}
$$

The quantity dW, is the incremental noise, which has a mean value of zero and standard deviation equal to $\sqrt{dt}$. Noting the constraint equation $x_7^2 + x_8^2 = 1$, the Euler-Maruyama method is used to obtain numerical solutions of equations (4.18).

Reduced Model with Noise: For the reduced model, $r = \delta$, $\dot{r} = 0$, and

$\ddot{r} = 0$. The rotor is in continuous contact with the stator and the state variables are defined as

$$\begin{cases} x_1 = \phi; \quad x_3 = \dot{\phi}; \quad x_5 = \sin(\phi - \beta) \\ x_2 = \theta; \quad x_4 = \dot{\theta}; \quad x_6 = \cos(\phi - \beta) \end{cases} \tag{4.19}$$

Equation (4.17) can be written in the state-space form as

$$\begin{cases} \dot{x}_1 = x_3 \\ \dot{x}_2 = x_4 \\ (M+m)\delta\dot{x}_3 + mex_6\dot{x}_4 = \Big[- c_b\delta x_3 \\ -mex_5(x_4+\Omega)^2 + F_t - mex_5\sigma(x_4+\Omega)\dot{W}(t)\Big] \\ me\delta x_6\dot{x}_3 + J\dot{x}_4 = \Big[- cx_4 - kx_2 \\ +me\delta x_3^2 x_5 + M_t\Big] \\ \dot{x}_5 = x_6\Big[x_3 - x_4 - \Omega - \sigma\dot{W}(t)\Big] \\ \dot{x}_6 = -x_5\Big[x_3 - x_4 - \Omega - \sigma\dot{W}(t)\Big] \end{cases} \tag{4.20}$$

In order to carry out numerical studies, similar to the full model, the above

equations are expressed in the Langevin form as

$$\begin{cases} dx_1 = x_3 dt \\ dx_2 = x_4 dt \\ (M+m)\delta dx_3 + mex_6 dx_4 = \Big[- c_b \delta x_3 \\ -mex_5(x_4+\Omega)^2 + F_t \Big] dt - mex_5 \sigma (x_4+\Omega) dW \\ me\delta x_6 dx_3 + J dx_4 = \Big[- cx_4 - kx_2 \\ +me\delta x_3^2 x_5 + M_t \Big] dt \\ dx_5 = x_6(x_3 - x_4 - \Omega)dt - \sigma x_6 dW \\ dx_6 = -x_5(x_3 - x_4 - \Omega)dt + \sigma x_5 dW \end{cases} \tag{4.21}$$

Here, similar to the full model, the quantity dW, is the incremental noise, which has a mean value of zero and standard deviation value of $\sqrt{dt}$. Noting the constraint equation $x_5^2 + x_6^2 = 1$, the Euler-Maruyama method can be used to obtain numerical solutions of equations (4.21). For the current study, the author has considered the full model to capture the impact between rotor and stator with the application of noise.

4.2 Results

Friction model. The analytical friction model along with friction model used for numerical simulations are given in equations (4.9) and (4.10). The graphical depictions of the same with two different values of minimum friction coefficient μ_m are shown in Figure 4.2. In rest of the chapter, the friction coefficient $\mu_m = 0.005$ is referred to as a small friction coefficient and $\mu_m = 0.05$ is referred to as a large friction coefficient. The author has studied the dynamics of the Jeffcott rotor with these two different friction coefficients and keeping other system parameters constant as shown in Table 4.2.

Deterministic system dynamics. For the parameters given in Table 4.2, the deterministic system dynamics, given by equations (4.5) and (4.12), are numerically solved by using the ODE solver in MATLAB. The system can have multiple stable solutions; that is, forward whirling with or without rotor-stator contact, and backward whirling with rotor-stator contact (Vlajic *et al.*, 2014b). The initial conditions determine which branch of the stable solution will eventually be reached by the system. For the current study, the author has chosen initial conditions such that the deterministic system dynamics is either in forward whirling with contact or in backward whirling with continuous rotor-stator contact. The same initial conditions are used when studying the influence of noise on system dynamics. The full model is a three degree-of-freedom system with r, ϕ, and θ as generalized coordinates. As noted earlier, 'r' represents the distance between the geometric center of the rotor and geometric center of the stator. ϕ represents the whirl angle, and θ represents

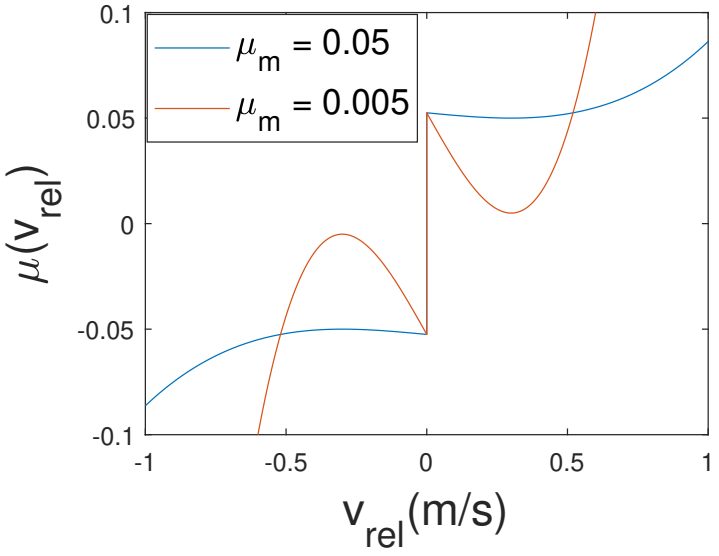

(a)

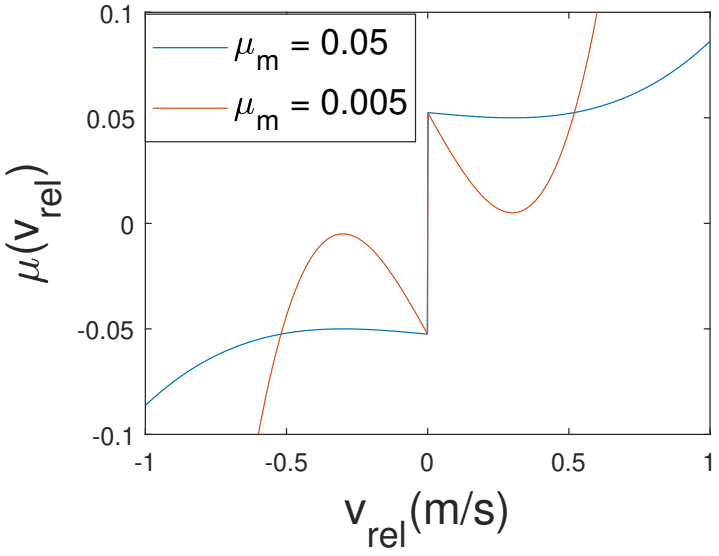

(b)

Figure 4.2: Friction coefficient model with two different values of minimum friction coefficient μ_m. In plot (a), analytical friction coefficient model is shown considering equation (4.9). In plot (b), friction coefficient model used for numerical simulations is shown considering equation (4.10).

the torsional angle. For continuous rotor-stator contact, $r = \delta$, where δ is the clearance between rotor and the stator in the static position. This results in reduction of one dimension and the governing equations for the reduced-order model can be

expressed as given in equation (4.12). For the current study, the counter-clockwise direction is assumed to be positive as shown in Figure 4.1.

For small value of the friction coefficient $\mu_m = 0.005$, a similar pattern is obtained with both the full and reduced-order models for forward whirling with continuous rotor-stator contact, as shown in Figure 4.3. The full model dynamics model is solved and results in $r = \delta = 0.01$, which is the condition for continuous rotor-stator contact. It is observed that the whirling frequency, denoted as $\omega_{for} = \dot{\phi}$, is found to be approximately equal to the prescribed angular speed Ω of the rotor and the whirl motion is in the direction of the input rotation. Additionally, the relative speed between the two surfaces at the point of contact is determined to be $v_{rel} \approx \delta\dot{\phi} + \Omega R = 0.24$ m/s. For the chosen parameter values, the torsional angle decays as shown in Figures 4.3(c)-(d). In this case, the forward whirling motion with continuous rotor-stator contact corresponds to a stable solution branch.

With an increase in the value of friction coefficient to $\mu_m = 0.05$, it is seen that the system dynamics moves from the forward whirling with contact to backward whirling with continuous rotor-stator contact via impact between rotor and stator. During the impact motion, $r < \delta$ and the reduced-order model is not able to capture the transient dynamics. The change in dynamics for full model is shown in Figure 4.4. The radial distance is shown in Figure 4.4(a), and $r < 0.01$ represents the impact motion. In Figure 4.4(b), it is seen that the whirl angle ϕ undergoes a clear transition from forward whirling to backward whirling. The torsion angle decay is shown in Figure 4.4(c). The steady-state whirling motion is in the opposite direction of the input rotation. This motion is called backward whirling and is associated with

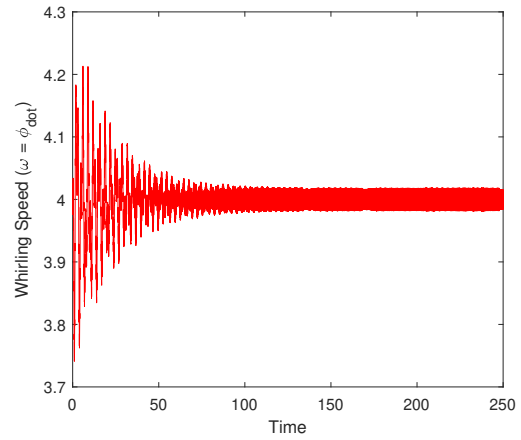

(a) Full Model: Whirling Speed

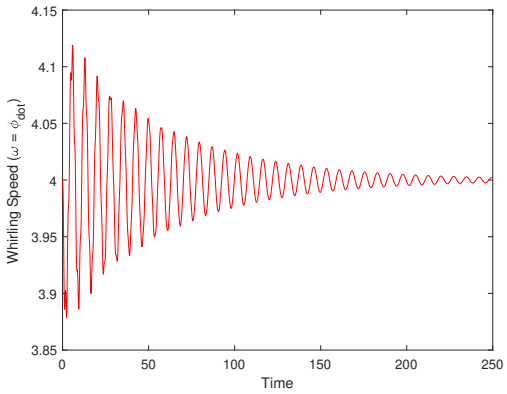

(b) Reduced Model: Whirling Speed

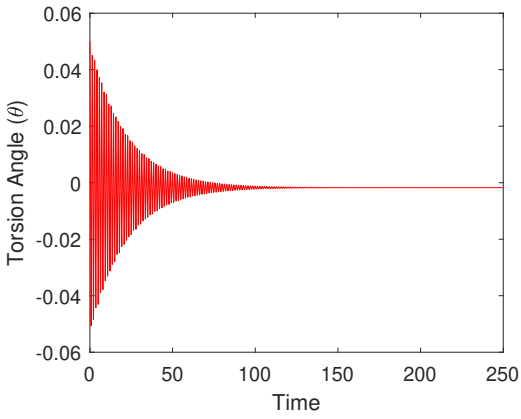

(c) Full Model: Torsional Angle

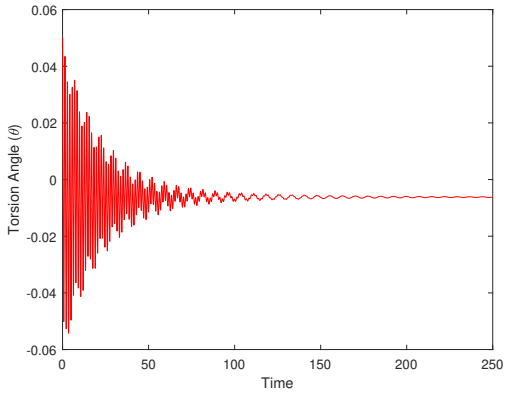

(d) Reduced Model: Torsional Angle

Figure 4.3: Comparisons of the results from the full model (equation (4.5)) and the reduced-order model (equation (4.12)) at $\Omega = 4.0$ rad/s and $\mu_m = 0.005$. Both the full model and reduced-order model results converge to forward whirling with continuous rotor-stator contact with a constant whirl speed of $\omega_{for} \approx \Omega = 4$ rad/s, and torsional perturbations that decay in both the full model and the reduced-order model simulations.

the negative sign. The steady state backward whirling frequency $\omega_{back} = \dot{\phi}$ is at a faster rate than the input rotation speed and is found to be approximately equal to $\omega_{back} \approx -\Omega\frac{R}{\delta} = -20$ rad/s. Additionally, the relative speed between the two surfaces at the point of contact satisfies $v_{rel} \approx \delta\dot{\phi} + \Omega R$ and is measured to be zero valued.

Further, the rotor dynamics with backward whirling with continuous rotor-stator contact is shown in Figure 4.5. The full model dynamics is in agreement with that of the reduced-order model. The steady state whirling speed is measured to be $\omega_{back} \approx -\Omega\frac{R}{\delta} = -20$ rad/s and the relative speed is found to be $v_{rel} \approx \delta\dot{\phi} + \Omega R = 0$ m/s.

It is noted that for a large friction coefficient $\mu_m = 0.05$, and given parameter values (see Table 4.2), the system dynamics with all the initial conditions reaches to a backward whirling state with continuous rotor-stator contact. On the other hand, for a small friction coefficient $\mu_m = 0.005$, and given parameter values (see Table 4.2), two different system dynamics are presented as shown in Figures 4.3 and 4.5. The steady state whirling speed can be expressed as

$$\omega_{for} \approx \Omega, \quad \omega_{back} \approx -\Omega\frac{R}{\delta} \tag{4.22}$$

Stochastic system dynamics. Numerical simulations have been conducted to study the changes in the system dynamics with a white Gaussian noise modulation in the driving speed. For numerical simulations with noise, the author chose the initial conditions corresponding to different branch curves obtained for the determin-

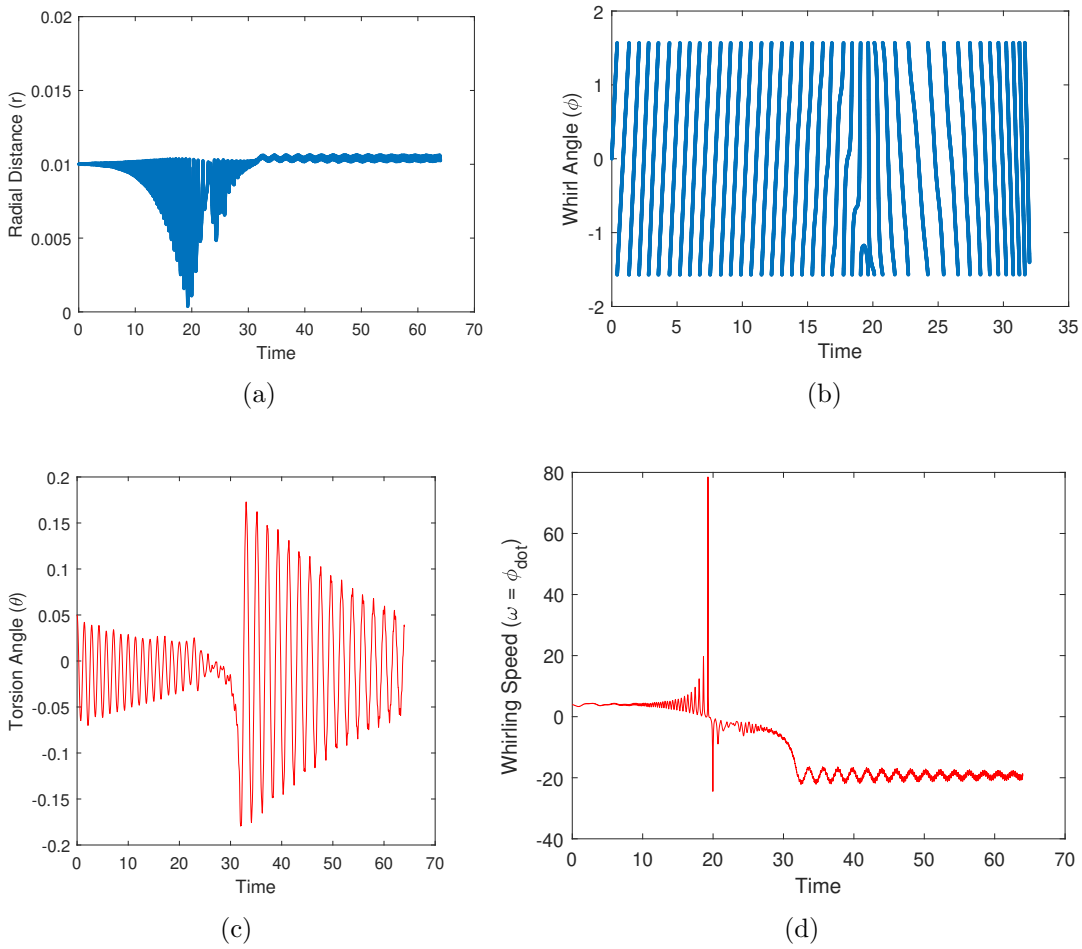

Figure 4.4: The system dynamics for the full model (equation (4.5)) at $\Omega = 4.0$ rad/s and $\mu_m = 0.05$. At this high value of the friction coefficient, with the same initial conditions as for Figure 4.3, the forward whirling motion is not stable and the system response moves from forward whirling with continuous rotor-stator contact to backward whirling with continuous rotor-stator contact via impact between rotor and stator. In plot (a), the radial distance between geometric center of rotor and geometric center of the stator is plotted and $r < 0.01$ represents the impact motion. In plot (b), the whirl angle ϕ is plotted and a clear transition from forward whirling to backward whirling is shown. The torsional angle, which is shown in plot (c), is seen to decay in time. In plot (d), the whirling speed is plotted and the steady state backward whirling frequency is found to be approximately equal to $\omega_{back} \approx -\Omega\frac{R}{\delta} = -20$ rad/s.

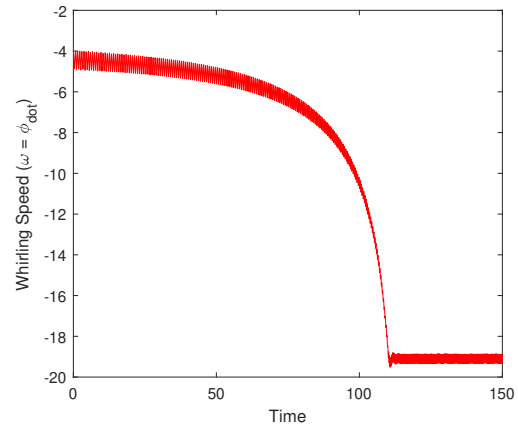

(a) Full Model: Whirling Speed

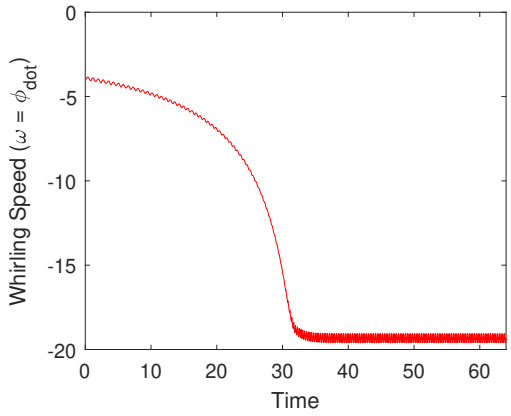

(b) Reduced Model: Whirling Speed

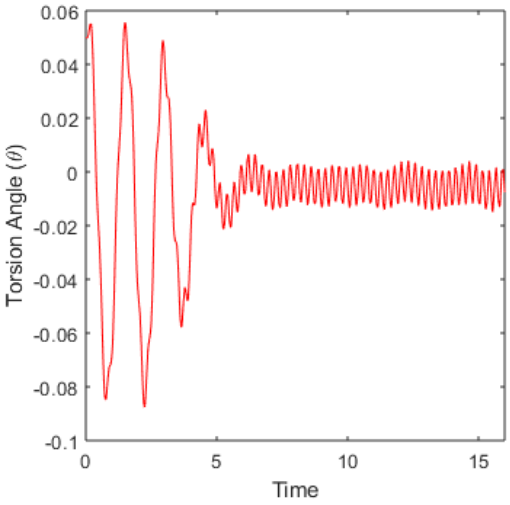

(c) Full Model: Torsional Angle

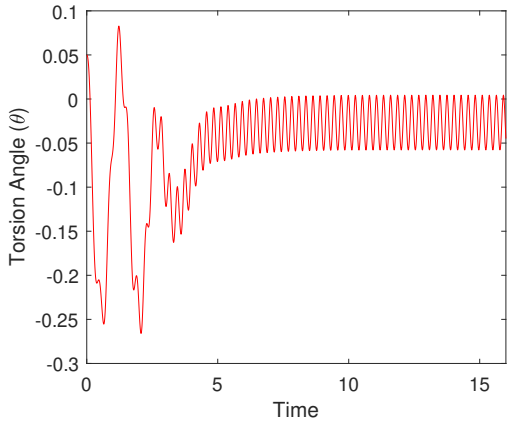

(d) Reduced Model: Torsional Angle

Figure 4.5: Comparisons of the results from the full model (equation (4.5)) and the reduced-order model (equation (4.12)) at $\Omega = 4.0$ rad/s and $\mu_m = 0.005$. Both the full model and reduced-order model results converge to backward whirling with continuous rotor-stator contact with a constant whirl speed of $\omega_{back} \approx -\Omega\frac{R}{\delta} = -20$ rad/s, and torsional perturbations that decay in both full model and reduced-order model simulations.

istic case. Here, the stochastic differential equation contains trigonometric functions with white Gaussian noise in phase modulation as shown in equation (4.5). This is called as trigonometric function representation of non-Gaussian processes where the trigonometric functions represent harmonic excitation with random phase modulation (Dimentberg, 1988). The author has introduced an extra dimension for the trigonometric function as defined in equation (4.16). The numerical results are obtained by solving the state-space form given by equation (4.18). The numerical simulation results are produced with the same initial conditions, the same rotor driving speed Ω and by averaging 100 Euler-Maruyama simulations in the time domain, and the steady-state response is captured. For a given driving speed Ω, each of these Euler-Maruyama simulations has the same noise amplitude σ, but different noise vectors. Any qualitative change in the system dynamics depends on the noise amplitude.

In Figure 4.6, the numerical results obtained for the small value of friction coefficient $\mu_m = 0.005$ and driving speed $\Omega = 4$ rad/s are shown. The deterministic dynamics shows a forward whirling motion with continuous rotor-stator contact as shown in Figure 4.3. For a noise amplitude $\sigma = 0.06$, the numerical results presented in Figures 4.6(b), 4.6(e), and 4.6(h) reveal that the system response moves from forward whirling with continuous rotor-stator contact to forward whirling with impact between rotor and stator. The whirling speed is still in the same direction as the driving speed. The noise inclusion is stopped after a while, but the system dynamics response stays on the branch of forward whirling with impact. The corresponding results are shown in Figures 4.6(c), 4.6(f), and 4.6(i). With a sufficient

level of noise modulation in the driving speed, it is noted that the system dynamics is moved from forward whirling with rotor-stator contact to no contact without any observable changes in the torsional angle.

Further, the effects of noise on the system dynamics of the backward whirling with continuous rotor-stator contact has been reached. The deterministic system response for $\mu_m = 0.005$ and driving speed $\Omega = 4$ rad/s is shown in Figure 4.5. The steady state backward whirling frequency ω_{back} is at a much faster rate than the input rotation speed for $\delta < R$, and is determined to be $\omega_{back} \approx -\Omega\frac{R}{\delta} = -20$ rad/s. Such backward whirling dynamics are very robust to noise modulation in the driving speed. The author has found a new way way to break the contact by decreasing the driving speed and introducing the noise afterwards. The reduction in driving speed results in reduction of whirling frequency. A proper combination of such driving frequency and noise amplitude can play an important role in influencing the system dynamics. In the current study, the author reduced the driving speed from 4 rad/s to 1 rad/s. The deterministic system dynamics is still in a backward whirling state with contact but, with the reduced whirling speed $\omega_{back} \approx -\Omega\frac{R}{\delta} = -5$ rad/s. The associated deterministic system dynamics results are shown in Figures 4.7(a), 4.7(d), 4.7(g), and 4.7(h). With the introduction of noise having a noise amplitude of $\sigma = 0.08$ units, the system response moves from back whirling with continuous rotor-stator contact to backward whirling with impact between rotor and stator. At that stage, the noise addition is stopped and this moves the response from backward whirling with impact to forward whirling with impact. The transition from backward whirling to forward whirling is shown in Figure 4.7(h). In transition from backward

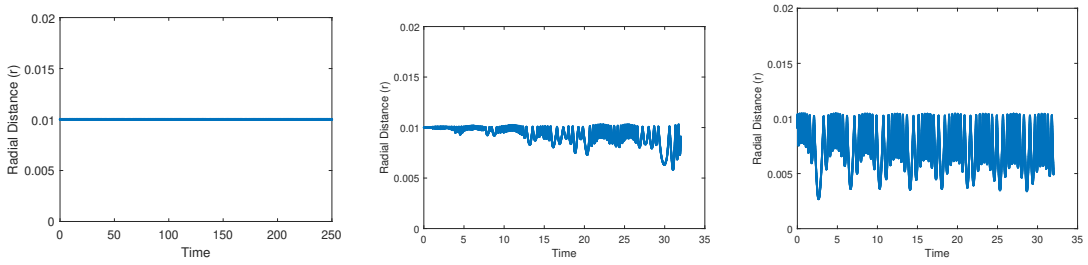

(a) $\sigma = 0$ (b) $\sigma = 0.06$ (c) $\sigma = 0$

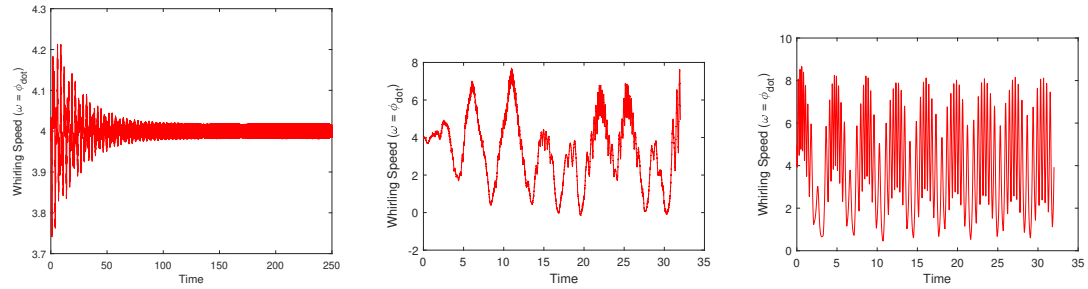

(d) $\sigma = 0$ (e) $\sigma = 0.06$ (f) $\sigma = 0$

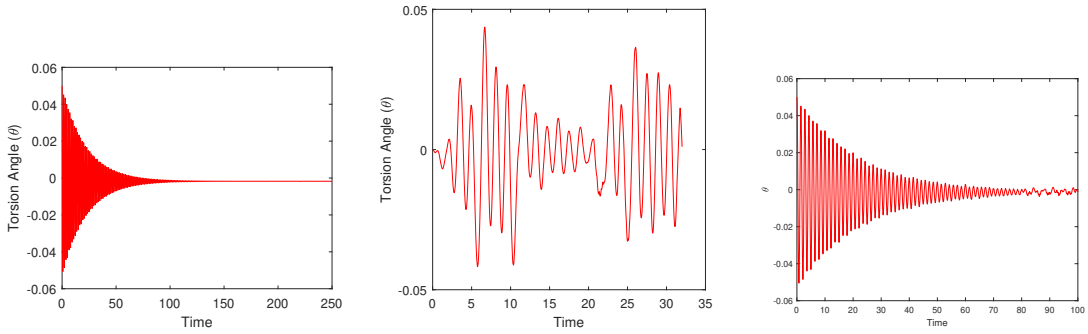

(g) $\sigma = 0$ (h) $\sigma = 0.06$ (i) $\sigma = 0$

Figure 4.6: The numerical results obtained for the small value friction coefficient $\mu_m = 0.005$ and driving speed $\Omega = 4$ rad/s. See Table 4.2 for system parameter values. The plots (a), (d), and (g) show the deterministic dynamics before the introduction of noise. The plots (b), (e), and (h) show the stochastic dynamics with a noise amplitude of $\sigma = 0.06$. The plots (c), (f), and (i) shows the deterministic dynamics after the noise addition has been stopped. For a noise amplitude $\sigma = 0.06$ units, the system response moves from forward whirling with continuous rotor-stator contact to forward whirling with impact between rotor and stator. The whirling speed is still in the same direction as the driving speed. After a while the noise addition has been stopped but the system dynamics response stays on the branch of forward whirling with impact.

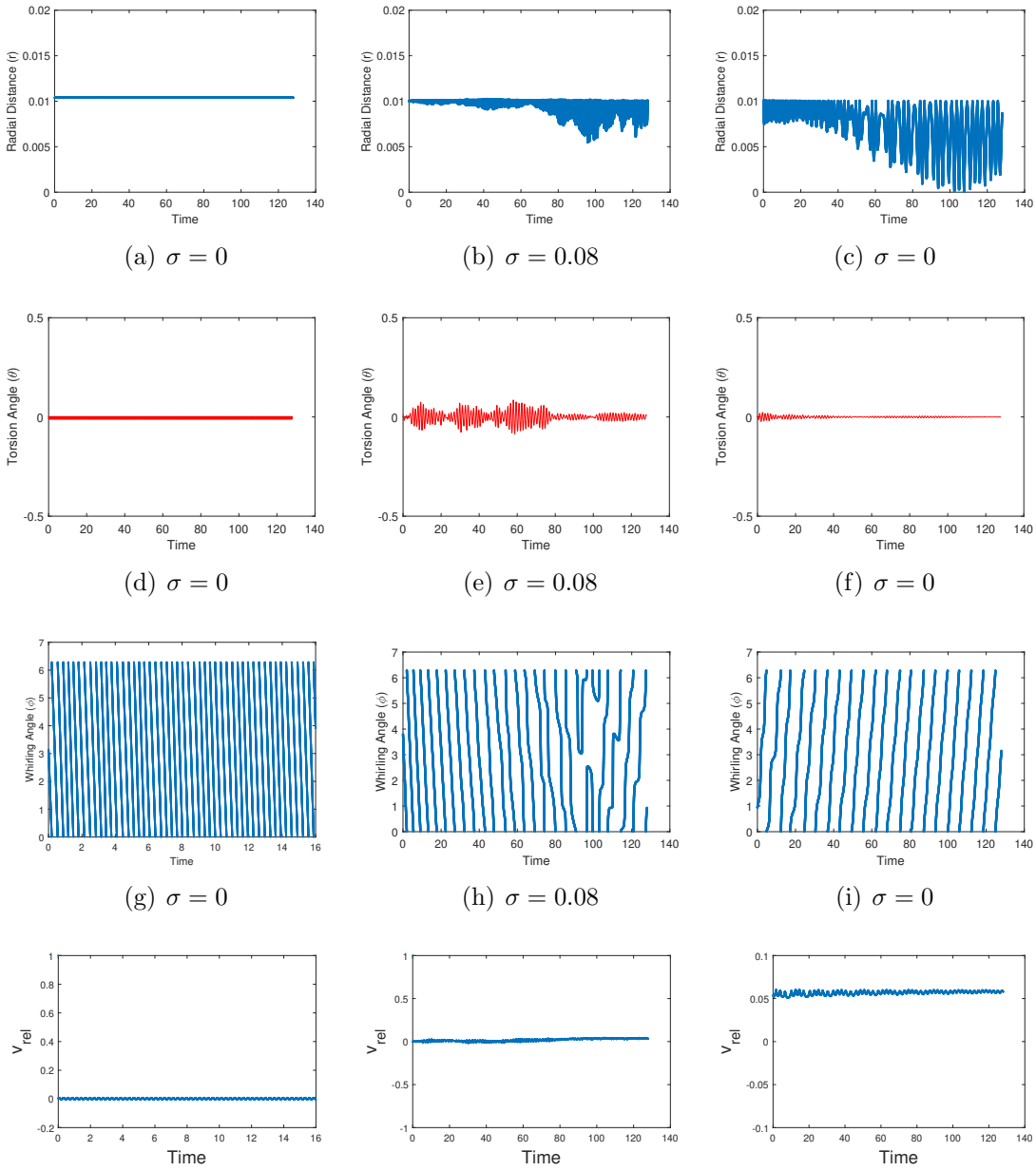

(a) $\sigma = 0$ (b) $\sigma = 0.08$ (c) $\sigma = 0$

(d) $\sigma = 0$ (e) $\sigma = 0.08$ (f) $\sigma = 0$

(g) $\sigma = 0$ (h) $\sigma = 0.08$ (i) $\sigma = 0$

(j) $\sigma = 0$ (k) $\sigma = 0.08$ (l) $\sigma = 0$

Figure 4.7: The numerical results obtained for the small value friction coefficient $\mu_m = 0.005$ and driving speed $\Omega = 1$ rad/s. See Table 4.2 for system parameter values. The plots in the first column show the deterministic dynamics before the introduction of noise. The column plots represent the stochastic dynamics with a noise amplitude of $\sigma = 0.08$ units. The last column plots show the deterministic dynamics after the noise has been stopped. The system response moves from backward whirling with continuous rotor-stator contact to forward whirling with impact between rotor and stator. The relative velocity between the two surfaces goes from a zero value to a non-zero value as shown in plots (j)-(l). In plot (h), the author shows the transition from backward whirling to forward whirling. There are no observable changes in the torsional angle.

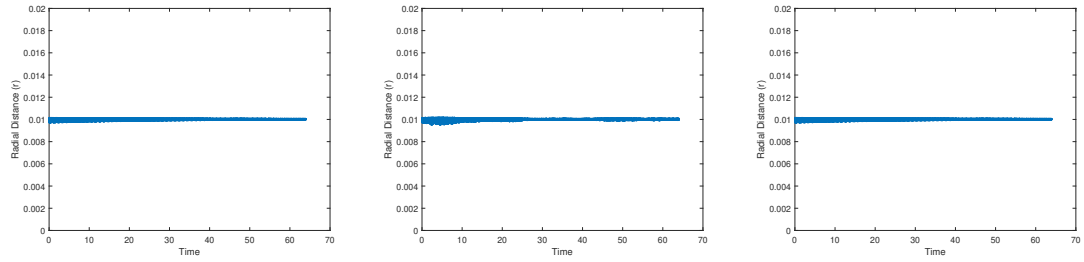

(a) $\sigma = 0$ (b) $\sigma = 0.08$ (c) $\sigma = 0$

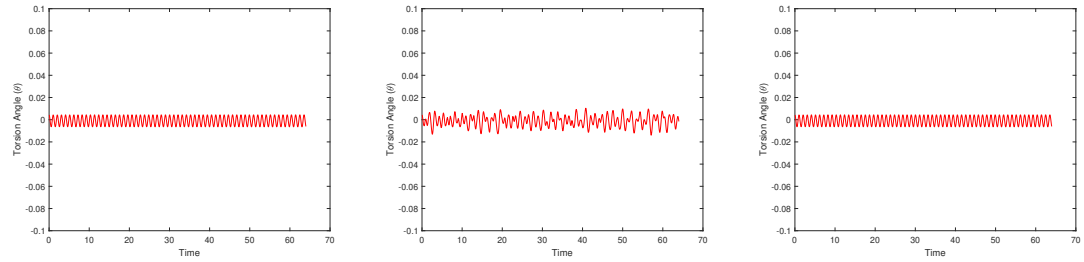

(d) $\sigma = 0$ (e) $\sigma = 0.08$ (f) $\sigma = 0$

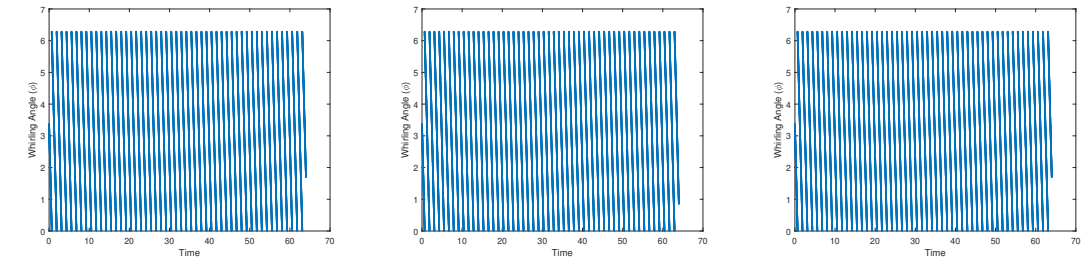

(g) $\sigma = 0$ (h) $\sigma = 0.08$ (i) $\sigma = 0$

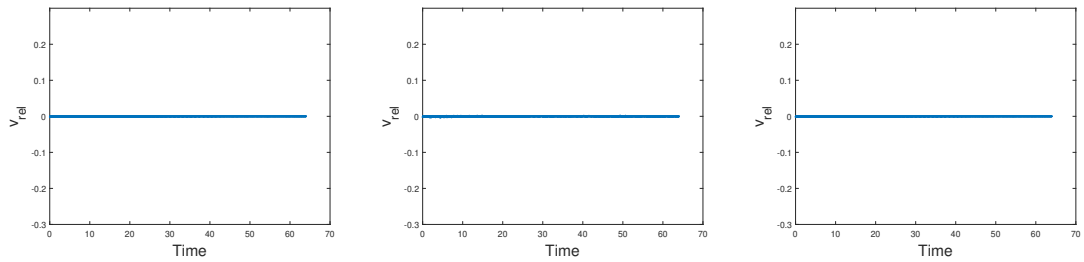

(j) $\sigma = 0$ (k) $\sigma = 0.08$ (l) $\sigma = 0$

Figure 4.8: The numerical results obtained for the large value friction coefficient $\mu_m = 0.05$ and driving speed $\Omega = 1$ rad/s. See Table 4.2 for system parameter values. The plots in the first column show the deterministic dynamics before the introduction of noise. The column plots represent the stochastic dynamics with a noise amplitude of $\sigma = 0.08$ units. The last column plots show the deterministic dynamics after the noise has been stopped. There are no qualitative changes observed in the system dynamics.

whirling to forward whirling, the relative velocity between the two surfaces goes from a zero value to a non-zero value as shown in Figures 4.7(j)-(l). For a small value of friction coefficient $\mu_m = 0.005$, with a combination of driving rotor speed Ω, and noise amplitude σ, the system dynamics can be moved from backward whirling to forward whirling.

On the other hand, for a large value of friction coefficient $\mu_m = 0.05$, there are no qualitative changes observed in the system dynamics and the system dynamics is still in backward whirling with continues rotor-stator contact. The corresponding results are shown in Figure 4.8.

4.3 Conclusions

The deterministic and stochastic dynamics of torsional vibrations and whirling motions for a Jeffcott rotor contained within a fixed stator during forward and backward whirling motions along with continuous rotor-stator contact have been been studied in this chapter. To capture motions with non-constant whirling speeds, the governing equations are constructed by using generalized polar coordinate system. In order to simplify the dynamics, reduced-order equations are constructed for a continuous rotor-stator contact with the aim of capturing whirling and torsional motions. The reduced-order model results are found to be in agreement with those obtained with the full model. Further, the effects of introduction of noise in driving speed have been explored. For a small value of the friction coefficient, it is noted that with noise addition, the system dynamics can be moved from forward or back-

ward whirling with contact to forward whirling with impact without any change in system parameter values.

Chapter 5: Summary of Contributions and Recommendations for Future Work

5.1 Summary of Contributions

In this section, the different research findings reported in Chapters 2 through 4 are collected and discussed.

A combination of experimental and numerical studies have been undertaken to comprehend the influence of white Gaussian noise on the responses of Duffing oscillators with hardening and softening spring characteristics as reported in Chapter 2. In the presence of harmonic excitation, the complex motions of this system are examined through experimental and numerical tools.

The key findings are as follows:

1. With an appropriate level of noise, the chaotic behavior of a harmonically forced oscillator can be significantly influenced. An addition of white Gaussian noise is found to push the aperiodic response of a softening Duffing oscillator to a stable fixed point of the corresponding unforced system (Agarwal and Balachandran, 2015).

2. Noise can be utilized to shift jump-up and jump-down frequencies and to get

rid of hysteresis observed in the response of a nonlinear oscillator. This finding suggests that the effect of nonlinearity on the frequency response of a softening Duffing oscillator can be countered through addition of white Gaussian noise (Agarwal *et al.*, 2018).

3. For nonlinear systems with a pair of attractors, one being periodic and another being chaotic, the chaotic attractor response can be controlled and terminated with introduction of an appropriate noise level. For trajectories in the basin of the chaotic attractor, white Gaussian noise can be added at a barely sufficient level to allow trajectories to eventually leave via a special escape route; that is, the unstable manifold of a fixed point saddle on the basin boundary between the two basins of attraction (Agarwal *et al.*, 2019). This work provides a glimpse into the possibilities for noise-influenced response control.

A partial control scheme constructed for a chaotic system is applied for confining the trajectories inside a particular region despite the presence of white noise as reported in Chapter 3 (Agarwal *et al.*, 2017; Agarwal and Balachandran, 2019a). As an illustration, the partial control method has been applied to restrict the response of a Duffing oscillator to a certain region of state-space. Numerical results with various noise forms are used to demonstrate the effectiveness of this control scheme. The proposed algorithm is shown to be effective for systems with different dimensions.

In Chapter 4, the dynamics of a modified Jeffcott rotor confined within a fixed stator is explored. The governing equations with a generalized polar coordinate

system are derived for a non-constant whirling speed (Agarwal and Balachandran, 2019b). Reduced-order equations are derived for a continuous rotor-stator contact with the aim of capturing whirling and torsional motions. The system dynamics is examined by using the reduced-order equations . The results of the analysis reveal a different but constant steady state whirling speed for both forward and backward whirling under the condition of contact. The reduced-order model results are found to be in agreement with those obtained with the full model. Further, the effects of introduction of noise in driving speed have been explored. The trigonometric representation of non-Gaussian excitation as a harmonic excitation with random phase modulation is considered and Euler-Maruyama simulation scheme is used for numerical integration.

5.2 Recommendations for Future Work

In Chapter 3 of this dissertation, the partial control scheme based on numerical simulations for finding safe sets for continuous time systems with white noise has been constructed. The viability of this approach with an experimental prototype of the Duffing oscillator with an extension to other systems are still remains to be completely addressed, for larger dimensions .

As the extension of the work presented in Chapter 2 and Chapter 4, studies of the effects of noise on a drill-string system could be one potential avenue for future research. Drill strings are long, tubular structures which are used for boring holes in the ground. These systems undergo large torsion deformations as well as

large lateral displacements. The effectiveness of noise in influencing backward and forward whirling motions can further be examined through experimental studies. Given the possibilities for noise-influenced dynamics reported here, understanding and exploiting noise for nonlinear systems can be further explored.

Appendix A: Use of the Method of Multiple Scales to Derive Frequency-Response Equation for a Forced Duffing Oscillator System

In this section, the derivation for an analytical implicit equation for the amplitude of response as a function of forcing frequency and the amplitude of harmonic excitation is presented which is used in Chapter 2. The analytical expression is obtained by using the method of multiple scales, see Nayfeh and Balachandran (1995).

Consider a forced Duffing oscillator system with weak forcing, weak damping, and weak nonlinearity and the equation of motion can be written as

$$\ddot{u} + \epsilon\eta\dot{u} + \Omega_n^2 u + \epsilon k_3 u^3 = \epsilon F_0 \cos(\Omega t). \tag{A.1}$$

Introducing a detuning parameter σ describes the nearness of Ω to Ω_n as $\Omega = \Omega_n + \epsilon\sigma$, where $\sigma = O(1)$. The expression of the solution in different time scales is of the form $u(t,\epsilon) = u_0(T_0, T_1, T_2, ...) + \epsilon u_1(T_0, T_1, T_2, ...) + \epsilon^2 u_2(T_0, T_1, T_2, ...) + ...$, where the different time scales are $T_0 = t, T_1 = \epsilon t$, and $T_2 = \epsilon^2 t$. The derivatives can be expressed as $\frac{d}{dt} = D_0 + \epsilon D_1 + \epsilon^2 D_2 ...$, and $\frac{d^2}{dt^2} = D_0^2 + 2\epsilon D_0 D_1 + \epsilon^2(D_1^2 + 2D_0 D_2) + ...$

Substituting these expansions back in Equation (A.1) and re-writing it again

as

$$\begin{aligned}(D_0^2 + 2\epsilon D_0 D_1 + \epsilon^2 D_1^2 + 2\epsilon^2 D_0 D_2 + ...)(u_0 + \epsilon u_1 + ...) \\ +\epsilon\eta(D_0 + \epsilon D_1 + ...)(u_0 + \epsilon u_1 + ...) + \Omega_n^2(u_0 + \epsilon u_1 + ...) \\ +\epsilon k_3(u_0 + \epsilon u_1 + ...)^3 = \epsilon F_0 \cos(\Omega_n T_0 + \sigma T_1)\end{aligned} \tag{A.2}$$

Equating the coefficients of ϵ^0, and ϵ^1 both side of the above equation, leads to the following set of equations:

$$O(\epsilon^0) : D_0^2 u_0 + \Omega_n^2 u_0 = 0 \tag{A.3}$$

$$O(\epsilon^1) : D_0^2 u_1 + \Omega_n^2 u_1 + 2D_0 D_1 u_0 + \eta D_0 u_0 + k_3 u_0^3 = F_0 \cos(\Omega_n T_0 + \sigma T_1) \tag{A.4}$$

The general solution of Equation (A.3) can be written as

$$u_0 = A(T_1)\exp(i\Omega_n T_0) + \bar{A}(T_1)\exp(-i\Omega_n T_0) \tag{A.5}$$

where $A(T_1)$ is determined by eliminating the secular terms from u_1. Substituting u_0 into Equation (A.4), expressing $\cos(\Omega_n T_0 + \sigma T_1)$ in a complex form, collecting the secular term and equating it to zero. The expression can be written as

$$2i\Omega_n(A' + \frac{\eta}{2}A) + 3k_3 A^2 \bar{A} - \frac{1}{2}F_0 \exp(i\sigma T_1) = 0 \tag{A.6}$$

where prime denotes the derivative with respect to T_1. To solve the above equation,

A can be written in the polar form as

$$A = \frac{1}{2} a \exp(ib) \tag{A.7}$$

where a and b are real. Separating the expression into its real and imaginary parts results in the following:

$$\begin{cases} a' &= -\frac{\eta}{2} a + \frac{1}{2} \frac{F_0}{\Omega_n} \sin(\sigma T_1 - b) \\ ab' &= \frac{3}{8} \frac{k_3}{\Omega_n} a^3 - \frac{1}{2} \frac{F_0}{\Omega_n} \cos(\sigma T_1 - b) \end{cases} \tag{A.8}$$

Considering $\sigma T_1 - b = \psi$, the above expression can be simplified as

$$\begin{cases} a' &= -\frac{\eta}{2} a + \frac{1}{2} \frac{F_0}{\Omega_n} \sin(\psi) \\ a\psi' &= \sigma a - \frac{3}{8} \frac{k_3}{\Omega_n} a^3 + \frac{1}{2} \frac{F_0}{\Omega_n} \cos(\psi) \end{cases} \tag{A.9}$$

For steady-state motions, $a' = \psi' = 0$, which simplifies the above equation as

$$\begin{cases} \frac{\eta}{2} a &= \frac{1}{2} \frac{F_0}{\Omega_n} \sin(\psi) \\ \sigma a - \frac{3}{8} \frac{k_3}{\Omega_n} a^3 &= -\frac{1}{2} \frac{F_0}{\Omega_n} \cos(\psi) \end{cases} \tag{A.10}$$

Squaring and adding the above equation results in

$$\left[\left(\frac{\eta}{2} \right)^2 + \left(\sigma - \frac{3}{8} \frac{k_3}{\Omega_n} a^2 \right)^2 \right] a^2 = \frac{F_0^2}{4\Omega_n^2} \tag{A.11}$$

Equation (A.11) is called as the frequency-response equation.

Bibliography

M. Frey, E. Simiu, Noise-induced chaos and phase space flux, Physica D: Nonlinear Phenomena 63 (1993) 321–340.

W. Liu, W. Zhu, Z. Huang, Effect of bounded noise on chaotic motion of duffing oscillator under parametric excitation, Chaos, Solitons & Fractals 12 (2001) 527–537.

C. Gan, Noise-induced chaos in duffing oscillator with double wells, Nonlinear Dynamics 45 (2006) 305–317.

X. Yang, W. Xu, Z. Sun, T. Fang, Effect of bounded noise on chaotic motion of a triple-well potential system, Chaos, Solitons & Fractals 25 (2005) 415–424.

D. Liu, W. Xu, Y. Xu, Noise-induced chaos in the elastic forced oscillators with real-power damping force, Nonlinear Dynamics 71 (2013) 457–467.

E. Perkins, B. Balachandran, Noise-enhanced response of nonlinear oscillators, Procedia IUTAM 5 (2012) 59–68.

E. Perkins, M. Kimura, T. Hikihara, B. Balachandran, Effects of noise on symmetric intrinsic localized modes, Nonlinear Dynamics 85 (2016) 333–341.

S. Ramakrishnan, B. Balachandran, Intrinsic localized modes in micro-scale oscillator arrays subjected to deterministic excitation and white noise, in: IUTAM Symposium on Multi-Functional Material Structures and Systems, Springer, pp. 325–334.

S. Ramakrishnan, B. Balachandran, Energy localization and white noise-induced enhancement of response in a micro-scale oscillator array, Nonlinear Dynamics 62 (2010b) 1–16.

S. Ramakrishnan, B. Balachandran, Influence of noise on discrete breathers in nonlinearly coupled micro-oscillator arrays, in: IUTAM Symposium on Dynamics Modeling and Interaction Control in Virtual and Real Environments, Springer, pp. 247–254.

G. Duffing, Erzwungene Schwingungen bei Veränderlicher Eigenfrequenz und ihre Technische Bedeutung (Vieweg, Braunschweig) in German, 1918.

A. H. Nayfeh, D. T. Mook, Nonlinear oscillations, John Wiley & Sons, 2008.

C. Hayashi, Nonlinear oscillations in physical systems, Princeton University Press, 2014.

I. Kovacic, M. J. Brennan, The Duffing equation: nonlinear oscillators and their behaviour, John Wiley & Sons, 2011.

A. Mallik, Response Of A Harmonically Excited Hard Duffing Oscillator–Numerical And Experimental Investigation, Springer, 2008.

E. Perkins, Effects of noise on the frequency response of the monostable duffing oscillator, Physics Letters A 381 (2017) 1009–1013.

J. Gottwald, L. Virgin, E. Dowell, Experimental mimicry of Duffing's equation, Journal of Sound and Vibration 158 (1992) 447–467.

A. H. Nayfeh, B. Balachandran, Applied nonlinear dynamics: analytical, computational and experimental methods, John Wiley & Sons, 1995.

H. Westra, M. Poot, H. Van Der Zant, W. Venstra, Nonlinear modal interactions in clamped-clamped mechanical resonators, Physical review letters 105 (2010) 117205.

T. Kalmár-Nagy, B. Balachandran, M. Brennan, Forced harmonic vibration of a duffing oscillator with linear viscous damping, The Duffing Equation: Nonlinear Oscillators and Their Behaviour, Wiley, New York (2011) 139–173.

A. Yao, T. Hikihara, Counter operation in nonlinear micro-electro-mechanical resonators, Physics Letters A 377 (2013) 2551–2555.

A. Yao, T. Hikihara, Reading and writing operations of memory device in micro-electromechanical resonator, IEICE Electronics Express 9 (2012) 1230–1236.

I. Mayergoyz, The classical preisach model of hysteresis, in: Mathematical models of hysteresis, Springer, 1991, pp. 1–63.

Y.-K. Wen, Method for random vibration of hysteretic systems, Journal of the engineering mechanics division 102 (1976) 249–263.

M. Dimian, P. Andrei, Mathematical models of hysteresis, in: Noise-Driven Phenomena in Hysteretic Systems, Springer, 2014a, pp. 1–63.

M. Dimian, P. Andrei, Noise driven relaxation phenomena in hysteretic systems, in: Noise-Driven Phenomena in Hysteretic Systems, Springer, 2014b, pp. 141–165.

T. Brown, I. Karaman, P. Shamberger, Impact of cycle-hysteresis interactions on the performance of giant magnetocaloric effect refrigerants, Materials Research Express 3 (2016) 074001.

C. Serpico, S. Perna, G. Bertotti, M. d'Aquino, A. Quercia, I. Mayergoyz, Noise-induced bifurcations in magnetization dynamics of uniaxial nanomagnets, Journal of Applied Physics 117 (2015) 17A709.

M. Dimian, P. Andrei, Noise spectral density of hysteretic systems, in: Noise-Driven Phenomena in Hysteretic Systems, Springer, 2014, pp. 167–200.

F. Moon, Experiments on chaotic motions of a forced nonlinear oscillator: strange attractors, Journal of Applied Mechanics 47 (1980) 638–644.

M. Todd, L. Virgin, An experimental verification of basin metamorphoses in a nonlinear mechanical system, International Journal of Bifurcation and Chaos 7 (1997) 1337–1357.

C. Grebogi, E. Ott, J. A. Yorke, Chaotic attractors in crisis, Physical Review Letters 48 (1982) 1507.

K. T. Alligood, T. D. Sauer, J. A. Yorke, Chaos, Springer, 1996.

C. Grebogi, E. Ott, J. A. Yorke, Critical exponent of chaotic transients in nonlinear dynamical systems, Physical review letters 57 (1986) 1284.

J. C. Sommerer, W. L. Ditto, C. Grebogi, E. Ott, M. L. Spano, Experimental confirmation of the scaling theory for noise-induced crises, Physical review letters 66 (1991) 1947.

L. Hong, J. Xu, Crises and chaotic transients studied by the generalized cell mapping digraph method, Physics Letters A 262 (1999) 361–375.

W. Xu, Q. He, T. Fang, H. Rong, Global analysis of crisis in twin-well duffing system under harmonic excitation in presence of noise, Chaos, Solitons & Fractals 23 (2005) 141–150.

G. Rega, F. Vestroni, IUTAM Symposium on Chaotic Dynamics and Control of Systems and Processes in Mechanics: Proceedings of the IUTAM Symposium Held in Rome, Italy, 8-13 June 2003, volume 122, Springer Science & Business Media, 2006.

I. T. Georgiou, I. B. Schwartz, The slow invariant manifold of a conservative pendulum-oscillator system, International Journal of Bifurcation and Chaos 6 (1996) 673–692.

V. In, M. L. Spano, J. D. Neff, W. L. Ditto, C. S. Daw, K. D. Edwards, K. Nguyen, Maintenance of chaos in a computational model of a thermal pulse combustor, Chaos: An Interdisciplinary Journal of Nonlinear Science 7 (1997) 605–613.

M. Perc, M. Marhl, Chaos in temporarily destabilized regular systems with the slow passage effect, Chaos, Solitons & Fractals 27 (2006) 395–403.

W. Yang, M. Ding, A. J. Mandell, E. Ott, Preserving chaos: Control strategies to preserve complex dynamics with potential relevance to biological disorders, Physical Review E 51 (1995) 102.

Á. G. López, J. Sabuco, J. M. Seoane, J. Duarte, C. Januário, M. A. Sanjuán, Avoiding healthy cells extinction in a cancer model, Journal of theoretical biology 349 (2014) 74–81.

S. Zambrano, M. A. Sanjuán, J. A. Yorke, Partial control of chaotic systems, Physical Review E 77 (2008) 055201(R).

J. Sabuco, S. Zambrano, M. A. Sanjuán, J. A. Yorke, Finding safety in partially controllable chaotic systems, Communications in Nonlinear Science and Numerical Simulation 17 (2012a) 4274–4280.

J. Sabuco, M. A. Sanjuán, J. A. Yorke, Dynamics of partial control, Chaos: An Interdisciplinary Journal of Nonlinear Science 22 (2012b) 047507.

S. Zambrano, M. A. Sanjuán, Exploring partial control of chaotic systems, Physical Review E 79 (2009) 026217.

R. Capeáns, J. Sabuco, M. A. Sanjuán, When less is more: Partial control to avoid extinction of predators in an ecological model, Ecological Complexity 19 (2014) 1–8.

H. Jecffott, The lateral vibration of loaded shafts in the neighborhood of a whirling speed-the eeffet of want of balanee [j], Phil. Mag 37 (1919) 304.

H. Black, Paper 4: synchronous whirling of a shaft within a radially flexible annulus having small radial clearance, in: Proceedings of the Institution of Mechanical Engineers, Conference Proceedings, volume 181, SAGE Publications Sage UK: London, England, pp. 65–73.

H. Black, Interaction of a whirling rotor with a vibrating stator across a clearance annulus, Journal of Mechanical Engineering Science 10 (1968) 1–12.

J. Jansen, Non-linear rotor dynamics as applied to oilwell drillstring vibrations, Journal of sound and vibration 147 (1991) 115–135.

C.-M. Liao, B. Balachandran, M. Karkoub, Y. L. Abdel-Magid, Drill-string dynamics: Reduced-order models and experimental studies, Journal of Vibration and Acoustics 133 (2011) 041008.

C.-M. Liao, N. Vlajic, H. Karki, B. Balachandran, Parametric studies on drill-string motions, International Journal of Mechanical Sciences 54 (2012) 260–268.

N. Vlajic, C.-M. Liao, H. Karki, B. Balachandran, Draft: stick-slip motions of a rotor-stator system, Journal of Vibration and Acoustics 136 (2014a) 021005.

N. Vlajic, X. Liu, H. Karki, B. Balachandran, Torsional oscillations of a rotor with continuous stator contact, International Journal of Mechanical Sciences 83 (2014b) 65–75.

H. Diangui, Experiment on the characteristics of torsional vibration of rotor-to-stator rub in turbomachinery, Tribology International 33 (2000) 75–79.

J. D. Jansen, L. Van Den Steen, Active damping of self-excited torsional vibrations in oil well drillstrings, Journal of sound and vibration 179 (1995) 647–668.

M. Karkoub, M. Zribi, L. Elchaar, L. Lamont, Robust μ-synthesis controllers for suppressing stick-slip induced vibrations in oil well drill strings, Multibody System Dynamics 23 (2010) 191–207.

A. Serrarens, M. Van de Molengraft, J. Kok, L. Van den Steen, H∞ control for suppressing stick-slip in oil well drillstrings, Control Systems, IEEE 18 (1998) 19–30.

A. Christoforou, A. Yigit, Fully coupled vibrations of actively controlled drillstrings, Journal of sound and vibration 267 (2003) 1029–1045.

S. Al-Hiddabi, B. Samanta, A. Seibi, Non-linear control of torsional and bending vibrations of oilwell drillstrings, Journal of sound and vibration 265 (2003) 401–415.

E. Kreuzer, M. Steidl, Controlling torsional vibrations of drill strings via decomposition of traveling waves, Archive of Applied Mechanics 82 (2012) 515–531.

A. Alzibdeh, M. Y. Al-Qaradawi, B. Balachandran, Influence of sinusoidal drive speed modulation on rotor with continuous stator contact, in: Qatar Foundation Annual Research Conference Proceedings, volume 2016, HBKU Press Qatar, p. EESP2073.

V. Agarwal, B. Balachandran, Noise-influenced response of Duffing oscillator, in: ASME 2015 International Mechanical Engineering Congress and Exposition, American Society of Mechanical Engineers, pp. V04BT04A019–V04BT04A019.

V. Agarwal, X. Zheng, B. Balachandran, Influence of noise on frequency responses of softening Duffing oscillators, Physics Letters A 382 (2018) 3355–3364.

V. Agarwal, J. A. Yorke, B. Balachandran, Noise-induced chaotic-attractor escape route, Chaos (2019) (Under Review).

V. Agarwal, J. Sabuco, B. Balachandran, Safe regions with partial control of a chaotic system in the presence of white gaussian noise, International Journal of Non-Linear Mechanics 94 (2017) 3–11.

V. Agarwal, B. Balachandran, Safe regions with dicrete time partial control of a chaotic system in the presence of noise, Chaos (2019a) (In Preparation).

V. Agarwal, B. Balachandran, Noise influenced rotor dynamics, International Journal of Mechanical Sciences (2019b) (In Preparation).

J. Yu, Y. Lin, Numerical path integration of a non-homogeneous markov process, International Journal of Non-Linear Mechanics 39 (2004) 1493–1500.

P. Hanggi, P. Riseborough, Dynamics of nonlinear dissipative oscillators, American Journal of Physics 51 (1983) 347–352.

T. Tél, M. Gruiz, Chaotic dynamics: an introduction based on classical mechanics, Cambridge University Press, 2006.

K. T. Alligood, T. D. Sauer, J. A. Yorke, Chaos, in: Chaos, Springer, 1997, pp. 105–147.

R. Capeáns, J. Sabuco, M. A. Sanjuán, Parametric partial control of chaotic systems, Nonlinear Dynamics 86 (2016) 869–876.

J. Aguirre, M. A. Sanjuán, Unpredictable behavior in the duffing oscillator: Wada basins, Physica D: Nonlinear Phenomena 171 (2002) 41–51.

R. I. Leine, H. Nijmeijer, Dynamics and bifurcations of non-smooth mechanical systems, volume 18, Springer Science & Business Media, 2013.

J. J. Thomsen, Vibrations and stability: advanced theory, analysis, and tools, Springer Science & Business Media, 2013.

M. F. Dimentberg, Statistical dynamics of nonlinear and time-varying systems, volume 5, Research Studies Press, 1988.